

ABSTRACT

GUO, WEI. Tailoring Light Emission of AlGaN Deep UV Emitters. (Under the direction of Professor Zlatko Sitar).

Tailoring and optimization of light emission and propagation of AlGaN based DUV emitters including light emitting diodes (LEDs) and laser diodes (LDs) was investigated. High absorption coefficients in the DUV range of AlN bulk crystals and a small light extraction cone lead to the low external quantum efficiency of high Al content AlGaN-based LEDs grown on AlN substrates prepared by physical vapor transport. A mild, controllable and smooth KOH based wet etching technique was developed. High selectivity between AlN and $\text{Al}_x\text{Ga}_{1-x}\text{N}$ as well as N-polar and III-polar was found to be critical in achieving effective substrate thinning or removal for AlGaN-based DUV LEDs. A smooth etching mechanism with reduced etching hillock size down to the wavelength scale was achieved by adding H_2O_2 into KOH etchant. The effect of adding H_2O_2 was explained by the formation and dissolution of oxide/ hydroxide on the III-nitride crystallographic planes, resulting in an isotropic etching perpendicular to the sample surface.

The fabrication of nano-porous and nano-pillar structures on III-nitride substrates and $\text{Al}_{0.5}\text{Ga}_{0.5}\text{N}/\text{AlN}$ MQW structures with feature size as small as 100 nm via natural lithography was also demonstrated. Nano-patterned structures revealed much lower integral reflectivity and enhanced photoluminescence intensity compared to as-grown structures, demonstrating a large-scale and mass-producible pathway to higher light extraction efficiency in surface-patterned DUV LEDs. In addition, periodic III-nitride arrays with pitch size of 200 nm were fabricated. This is the smallest periodicity achieved on GaN and AlN thin films so far using interference lithography. Angle-resolved transmission measurement

demonstrated diagonal intensity streaks on the pseudo-3D transmission graph as a function of both wavelength and collection angle. This was interpreted as a direct evidence of the existence of a photonic crystal.

Optical gain and polarization properties of AlGaN based laser diode structures grown on AlN bulk substrate were also investigated. An exponential increase of the edge emission with dominant TE polarization demonstrated the onset of stimulated emission. In addition, the gain spectra and gain thresholds of a single AlGaN layer, an AlGaN double-heterostructure, and an AlGaN/AlGaN Multiple-Quantum-Well structure were investigated and compared. In the case of the single AlGaN epitaxial layer no optical confinement was assumed. Therefore, the found positive gain value demonstrated the good optical quality of our AlGaN epitaxial layer. Net modal gain values of 16 cm^{-1} , 58 cm^{-1} , and 48 cm^{-1} were observed for a single AlGaN epitaxial layer, DH, and MQW structure, respectively, at a pumping power density of 1MW/cm^2 . Furthermore, *Silvaco* simulation was applied in theoretical calculation of gain spectra and mode distribution, 5000 cm^{-1} material gain coefficient can be achieved for MQW structure accompanied with a low (0.9%) optical confinement factor due to strong asymmetric design of cladding layer. The results provide guidance in further optimization of LD structures.

© Copyright 2014 Wei Guo

All Rights Reserved

Tailoring Light Emission of AlGaN Deep UV Emitters

by
Wei Guo

A dissertation submitted to the Graduate Faculty of
North Carolina State University
in partial fulfillment of the
requirements for the degree of
Doctor of Philosophy

Materials Science and Engineering

Raleigh, North Carolina

2014

APPROVED BY:

Zlatko Sitar
Committee Chair

Ramón Collazo

Jon-Paul Maria

John Muth

DEDICATION

To my parents, this dissertation is for you.

BIOGRAPHY

The author, Wei Guo was born on December 22nd, 1987 in Ma'anshan City in eastern part of China. He joined Shanghai Jiao Tong University in Shanghai, China studying Materials Science and Engineering. After he received his Bachelor of Engineering degree in 2010, he enrolled in the doctoral program of the Materials Science and Engineering Department at North Carolina State University.

ACKNOWLEDGMENTS

I would like to thank my advisor Dr. Zlatko Sitar for his patient guidance in my research as well as his rich knowledge and expertise in almost every aspects of work. I would like to give thanks to Dr. Ramón Collazo for his guidance and assistant in the detailed research work. I also like to thank Dr. Jon-Paul Maria and Dr. John Muth for being my committee members and providing useful suggestions and comments. In addition, I am grateful to all the colleagues and good friends in the Wide-Band-Gap Lab for their help in my research and fruitful discussions during my PhD. They are: Jinqiao Xie, Seiji Mita, Ronny Kirste, James Tweedie, Anthony Rice, Marc Hoffmann, Alexander Franke, Lindsay Hussey, Isaac Bryan, Zachary Bryan, Milena Bobea, Pramod Reddy, Shun Washiyama, Felix Kaess and Dorian Alden. I would like to thank Yiling Yu from Dr. Linyou Cao's group at MSE department for the resources of FDTD simulation software; Abhijeet Bagal from Dr. Chi-Hao Chang's group at MAE department for his generous help in interference lithography fabrication. Finally, I would like to thank our Materials Science and Engineering department, especially Dr. Yuntian Zhu for his initial help in giving me TA at the beginning of study at NCSU and Jan Jackson for her help on a lot of things related to working at RB1.

TABLE OF CONTENTS

| | |
|--|------|
| LIST OF TABLES | viii |
| LIST OF FIGURES | ix |
| CHAPTER 1 Introduction..... | 1 |
| 1.1 Dissertation overview | 1 |
| 1.2 Properties of III-nitrides..... | 2 |
| 1.3 Growth of III-nitride bulk crystals and epitaxial films | 5 |
| 1.4 Deep UV Light-Emitting-Diodes (LEDs)..... | 7 |
| 1.4.1 Working conditions and applications..... | 7 |
| 1.4.2 Development of UV-LEDs | 8 |
| 1.4.3. Definition of the quantum efficiency | 10 |
| 1.4.4 Light extraction in AlGaN-based UV-LEDs | 11 |
| 1.5 UV-Laser Diodes and its characterization | 14 |
| 1.5.1 General property of stimulated emission | 14 |
| 1.5.2 Optical gain and laser diode structure..... | 17 |
| 1.5.3 Deep UV laser diodes applications | 21 |
| CHAPTER 2 Selective wet etching of AlN, GaN, and Al _x Ga _{1-x} N | 23 |
| 2.1 Substrate removal for light extraction enhancement in DUV-LEDs | 23 |
| 2.2 Experimental design..... | 26 |
| 2.3 The influence of the Al composition on the etch rate and selectivity..... | 31 |
| 2.4 The influence of KOH etching on the surface morphology..... | 36 |

| | |
|--|----|
| 2.5 Surface stoichiometry investigation on etched surfaces and investigation of the H ₂ O ₂ smoothening mechanism..... | 43 |
| 2.6 Etching hillock development and etching mechanism..... | 46 |
| 2.7 Conclusion | 50 |
| CHAPTER 3 Surface patterning of III-nitrides | 52 |
| 3.1 Surface patterning for light extraction efficiency enhancement in DUV-LEDs..... | 52 |
| 3.1.1 Natural lithography technique..... | 53 |
| 3.1.2 Interference lithography technique | 54 |
| 3.1.3 Photonic crystals | 55 |
| 3.2 Natural lithography and interference lithography for III-nitrides..... | 57 |
| 3.3 Surface morphology of patterned III-nitride surfaces..... | 64 |
| 3.3.1 Nano-porous and nano-pillar GaN fabricated by natural lithography | 64 |
| 3.3.2 1D and 2D III-nitride periodic arrays fabricated by interference lithography..... | 73 |
| 3.4 Optical properties of patterned III-nitrides | 76 |
| 3.4.1 Integral reflectivity of nano-patterned structures..... | 76 |
| 3.4.2 Angle-resolved transmission of nano-patterned structures..... | 80 |
| 3.4.3 Angle-resolved photoluminescence spectra of nano-patterned MQW structures.. | 82 |
| 3.5 FDTD simulation of the light extraction efficiency and the far-field emission profile of DUV-LEDs | 84 |
| 3.6 Conclusions..... | 87 |
| CHAPTER 4 Stimulated emission and optical gain measurements in AlGaN based Laser Diode structures | 89 |

| | |
|--|-----|
| 4.1 The influence of modal gain and gain threshold on the performance of laser diodes .. | 89 |
| 4.2 Experiment procedure | 92 |
| 4.3 Stimulated emission and polarization characteristics of AlGaN heterostructures | 97 |
| 4.4 Gain spectra and threshold values of AlGaN heterostructures | 104 |
| 4.5 Simulation of the gain characteristic and the LD structural design | 113 |
| 4.6 Conclusion | 120 |
| CHAPTER 5 Conclusions and future work..... | 122 |
| 5.1 Conclusions..... | 122 |
| 5.2 Future work..... | 124 |
| REFERENCES | 126 |
| APPENDIX..... | 142 |
| Appendix A: Matlab script for optical gain analysis | 143 |

LIST OF TABLES

| | |
|--|-----|
| Table 1.1. Basic properties of III-nitride material ¹⁶ | 4 |
| Table 2.1. Wet etching rate of the N-polar and III-polar surface of AlN and GaN single crystal substrates in 1 wt% KOH at 70°C..... | 33 |
| Table 4.1. Maximum net optical gain values at different pumping powers and the estimated gain threshold values for the three investigated AlGaN-based samples..... | 108 |

LIST OF FIGURES

| | |
|---|----|
| Figure 1.1. Schematic image of partial unit cell of a wurtzite III-nitride crystal | 3 |
| Figure 1.2. Schematic image of carrier distribution under forward bias of a p-n junction..... | 8 |
| Figure 1.3. Schematic graphs showing the processes of (a) absorption, (b) spontaneous emission, and (c) stimulated emission. | 16 |
| Figure 1.4. Structure of an AlGaN-based DUV edge emission laser diode showing the stack design, laser cavity and metal contacts | 20 |
| Figure 2.1. Image of the AlN and GaN bulk wafer used to investigate etching behavior.... | 28 |
| Figure 2.2. Optical microscope image of an $\text{Al}_{0.6}\text{Ga}_{0.4}\text{N}$ LPS with 10 μm stripes before KOH etching (a) and after KOH etching (b). | 30 |
| Figure 2.3. Etch depth versus etching time for AlN (a) and GaN (b) single crystal substrates in KOH and KOH/ H_2O_2 solutions at 70°C..... | 34 |
| Figure 2.4. Etch selectivity ($\text{AlN}/\text{Al}_x\text{Ga}_{1-x}\text{N}$) as a function of Al composition under KOH (0.5 wt%, 50°C) etching condition. | 36 |
| Figure 2.5. AFM images of Ga-polar GaN before (a) and after KOH/ H_2O_2 etching for 30min (b). | 37 |
| Figure 2.6. SEM micrographs of N-polar AlN etched in KOH (a), KOH/ H_2O_2 (b) and N-polar GaN etched in KOH (c), KOH/ H_2O_2 (d) at 70°C for 60min..... | 39 |
| Figure 2.7. 60° tilted SEM micrographs of $\text{Al}_x\text{Ga}_{1-x}\text{N}$ LPS grown on sapphire substrate, when $x=1$, before etch (a), $x=1$, after etch (b), $x=0$, before etch (c), $x=0$, after etch (d). N-polar was shown on the left while III-polar was shown on the right within each image | 41 |

| | |
|---|----|
| Figure 2.8. SEM cross-sectional images of hillocks on N-polar AlN (a) and N-polar GaN (b) after etching in KOH at 70°C for 60 min..... | 42 |
| Figure 2.9. Schematic of crystallographic planes of etched hillocks..... | 42 |
| Figure 2.10. Surface molar ratios for N-polar AlN before etching and etched in KOH and KOH/H ₂ O ₂ solutions for 15min..... | 45 |
| Figure 2.11. Deconvoluted O 1s core level peak of a KOH etched N-polar AlN (a) and the oxygen component distribution (b)..... | 46 |
| Figure 2.12. Amplitude AFM images of N-polar AlN etched in KOH/H ₂ O ₂ solution for 15s (a) and 30s (b). | 47 |
| Figure 2.13. Amplitude AFM image of N-polar AlN etched in pure KOH solution for 15s. | 48 |
| Figure 2.14. Plan view SEM image of N-polar AlN etched in KOH solution (a) and illustration showing the development of etching hillock during etching (b)..... | 49 |
| Figure 2.15. Cross-sectional TEM image of AlN (a,b) and GaN (c,d) after KOH etching for 30min. Insets images are electron diffraction patterns with corresponding g vectors. No correlation between hillocks and dislocations is observed. | 50 |
| Figure 3.1. Schematic process flow of natural lithography patterning on GaN or AlN. | 59 |
| Figure 3.2. Lloyd's Mirror interferometer setup used for interference lithography. | 60 |
| Figure 3.3 Schematic process flow of the interference lithography patterning. | 62 |
| Figure 3.4. Schematic showing the setups for (a) integral reflectivity measurements and (b) angle-resolved transmission measurements. | 63 |

| | |
|--|----|
| Figure 3.5. FE-SEM images of AAO on GaN fabricated by the two-step anodization method: (a) 6 min anodization, plan view, (b) 9 min anodization, plan view, (c) 9 min anodization, cross-sectional view | 65 |
| Figure 3.6. AAO pore diameter distribution histogram binned in 5 nm increments for AAO with optimal anodization condition. | 66 |
| Figure 3.7. Plan-view FE-SEM images of GaN nano-porous arrays after etching in Cl ₂ /BCl ₃ 25 sccm/25 sccm for (a) 4 min, (b) 7 min, (c) 15min. | 67 |
| Figure 3.8. Plan-view SEM images of SiO ₂ particle (100 nm diameter) spin coated on a GaN surface: (a) 2 wt% SiO ₂ concentration; (b) 6 wt% SiO ₂ concentration; (c) 10 wt% SiO ₂ concentration..... | 68 |
| Figure 3.9. Plan view FE-SEM images of (a) a 100 nm SiO ₂ sphere monolayer on GaN; (b) GaN nano-pillars after transfer; (c) SiO ₂ sphere monolayer after sphere diameter was reduced; (d) GaN nano-pillars obtained after reducing the sphere size..... | 70 |
| Figure 3.10. Tilted (60°) FE-SEM images of GaN nano-pillars obtained at different conditions: (a) as deposited spheres and 2 min Cl ₂ /BCl ₃ etching; (b) 1 min CF ₄ etching to reduce the sphere size, followed by 2 min Cl ₂ /BCl ₃ etching; (c) as deposited spheres and, 4 min etching; (d) 1 min CF ₄ etching to reduce the sphere size, followed by 4 min Cl ₂ /BCl ₃ etching..... | 71 |
| Figure 3.11. (a,b) FE-SEM images of a monolayer of 200 nm diameter SiO ₂ spheres on GaN and (c) 80° tilted view of GaN nano-pillars after RIE and plasma shrinking. | 72 |
| Figure 3.12. 1D (a) and 2D (b) PR patterning on GaN generated by interference lithography. | 74 |

| | |
|--|----|
| Figure 3.13. 1D (a) and 2D (b) GaN patterning achieved by interference lithography after pattern transfer from PR..... | 75 |
| Figure 3.14. SEM images of 2D AlN arrays with periodicity of (a) 400 nm and (b) 600 nm. | 76 |
| Figure 3.15. Measured integral reflectivity of planar GaN and GaN with nano-pillars of different shapes on the surface..... | 77 |
| Figure 3.16. (a) Fitted integral reflectivity of patterned GaN and (b) calculated reduction of the integral reflectivity after nano-patterning. | 78 |
| Figure 3.17. Angle-resolved transmission spectra of planar GaN and 2D GaN periodic array structures | 80 |
| Figure 3.18. (a) Light intensity profile for planar GaN and (b) comparison between planar GaN and the 2D periodic GaN array..... | 82 |
| Figure 3.19. (a) Room temperature PL spectra of $\text{Al}_{0.5}\text{Ga}_{0.5}\text{N}/\text{AlN}$ MQW structures grown on an AlN substrate before and after nano-patterning collected perpendicular to the sample surface; (b) Integrated PL intensity of planar MQW and nano-pillar-patterned MQW structures collected at different angles..... | 84 |
| Figure 3.20. (a) FDTD simulation domains comprising nano-patterned LED structures on top of a GaN layer and (b) far-field intensity of nano-patterned LED in comparison to planar LED for emission wavelength around 400 nm. | 87 |
| Figure 4.1. Schematic setup of the investigated AlGaN samples. (a) single $\text{Al}_{0.7}\text{Ga}_{0.3}\text{N}$ film, (b) a double heterostructure, and (c) MQW structure | 93 |

| | |
|---|-----|
| Figure. 4.2. Schematic diagram of the variable-stripe-length experimental setup for a collection of the sample luminescence from the edge (a) and sketch of luminescence collected from the edge of the sample and in a 45° configuration (b)..... | 96 |
| Figure 4.3. SEM image (60° tilted with respect to sample surface) of the cleaved single AlGaN epitaxial layer grown on an AlN substrate. The thickness of the AlGaN film is ~300 nm. It indicates a smooth cleavage facet, which is desirable for optical gain measurement.. | 96 |
| Figure 4.4. Spontaneous emission spectra collected at an angle of 45 ° normal to the top surface of the AlGaN epitaxial layer for various pumping powers; (b) Peak intensity as a function of the pumping power for the AlGaN epitaxial layer, the red line shows a linear fit of the data points..... | 98 |
| Figure 4.5. Comparison of the edge emission spectra (solid lines) and the surface emission recorded at an angle of 45 ° normal to the top surface (dashed line) of the single AlGaN film (a), the AlGaN-DH (b), and the AlGaN-MQW (c) structure for pumping powers between 100–800 kW/cm ² | 100 |
| Figure 4.6. Peak emission intensity (black squares) and resulting FWHM (red triangles) with increasing pumping powers for (a) a single AlGaN layer, (b) a DH structure, and (c) a MQW structure measured at room temperature..... | 102 |
| Figure 4.7. TE and TM emission spectra collected from the edge of the single AlGaN layer sample at a pumping power of 1000 kW/cm ² (a) and 50 kW/cm ² (b). All spectra were normalized with respect to the emission maximum of the TM polarized light for easier comparison..... | 104 |

| | |
|---|-----|
| Figure 4.8. Stimulated emission peak intensity as a function of stripe length for (a) the single AlGaN layer, (b) the DH structure, and (c) the MQW samples under different pumping powers of 300 kW/cm ² , 700 kW/cm ² , and 1000 kW/cm ² | 107 |
| Figure 4.9. Maximum optical gain values as a function of the pumping power for three different samples. The gain threshold values were estimated by the intercept of the linear extrapolation of the data with a gain value equals to zero..... | 109 |
| Figure 4.10. Spectral dependency of the net modal gain value for three different pumping power for the (a) single AlGaN layer, (b) DH structure, and (c) MQW sample. | 111 |
| Figure 4.11. Modal gain spectra under low and high pumping powers densities measured at the single AlGaN structure (a); Maximum gain values and the corresponding spectral peak positions as a function of the pumping power for the single AlGaN layer (b)..... | 112 |
| Figure 4.12. Simulated material gain spectra for different carrier concentrations within the (a) single AlGaN layer, (b) the AlGaN based DH structure, and (c) the MQW sample..... | 115 |
| Figure 4.13. Spatial distribution of the simulated fundamental mode and the refractive index profile of the single AlGaN epitaxial layer..... | 118 |
| Figure 4.14. Spatial distribution of the simulated fundamental TE (a), second harmonic TE (b), and third harmonic TE mode within the MQW sample. The refractive index profile is given by the blue curve (right ordinate axis). | 119 |

CHAPTER 1 Introduction

1.1 Dissertation overview

AlN, GaN and their alloys are being actively pursued for optoelectronic applications that take advantage of their tunable wide bandgap and unique properties including chemical stability and spontaneous polarization. The direct bandgap of the binary alloy $\text{Al}_x\text{Ga}_{1-x}\text{N}$ ranges from 3.4 eV (GaN) to 6.1 eV (AlN). This allows for applications such as bio-chemical detection, medical diagnostics and free-space communication. In the last years, AlGaN-based ultraviolet light emitting diodes (UV-LEDs),[1, 2] laser diodes (LDs),[3, 4] AlGaN/GaN heterostructure field-effect transistors (HFETs)[5, 6] and AlGaN/GaN heterojunction bipolar transistors (HBTs)[7] have been reported.

Typically, the performance of AlGaN-based UV-LEDs is inferior compared to that of InGaN-based LEDs. High wall plug efficiencies as observed in InGaN-based blue LEDs[8-10] or AlGaNInP red or yellow LEDs[11-13] have not been demonstrated and will require significant efforts in the future. The main obstacle lies in the unsatisfactory material quality of AlGaN layers due to a lack of defect control during growth and suitable native substrates. Furthermore, light extraction in AlGaN based UV LEDs is found to be below 4% as a result of total internal reflection at the device interface. In regards to AlGaN-based UV-LDs, only few works have been conducted on stimulated emission and gain characteristic, let alone electrically injected UV-LDs. More details related to UV-LEDs/LDs will be discussed in the following chapters and possible solutions will be presented in order to increase the efficiency of AlGaN-based UV-LEDs and reduce threshold values for AlGaN-based UV-LDs.

General information about the basic properties of III-nitrides and related LEDs/LDs will be provided in Chapter 1. Chapter 2 will provide information on selective wet etching to remove AlN substrate of UV-LEDs to increase light extraction. In Chapter 3 light extraction enhancement of AlGaN-based UV-LEDs via substrate patterning, including natural lithography and interference lithography technique will be discussed. In Chapter 4, stimulated emission, polarization properties and gain characteristic of high Al composition AlGaN based LD structures will be investigated. Possible device designs of LD with high modal gain and low threshold values will also be provided. Finally, the work will be summarized in Chapter 5 and an outlook for future development will be given.

1.2 Properties of III-nitrides

III-nitride materials including AlN, GaN, InN and the (pseudo-)binary/ternary alloys among them are considered to be the most important building blocks in semiconductor devices after Si. III-nitrides can crystallize in the wurtzite (Wz) and zinc blende (ZB) structure; samples discussed in this work were all grown in the wurtzite structure. The wurtzite structure belongs to the hexagonal crystal system. For III-nitrides the lattice contains two sets of hexagonal close packed (HCP) sub-lattices of N- and group-III metal atoms, offset by $\frac{5}{8}c$, where c is the lattice parameter along c axis. Figure 1.1 shows a schematic image of the partial unit cell of a wurtzite III-nitride crystal structure. Since the wurtzite crystal is non-centrosymmetric, III-nitride crystals have two distinct orientations. The crystal is either III-polar ([0001] direction) or N-polar ([000-1] direction). Due to the strong difference in electronegativity between the N and group-III metal atoms, a strong

spontaneous polarization is established. It points from the N-atoms to the group-III atoms, and, thus, induces an internal electric field pointing in the opposite direction.

III-nitride materials have a strong III-N bonding, great chemical stability, direct bandgap, high thermal conductivity and high breakdown field.[14, 15] Some basic physical properties are listed in Table 1.1.

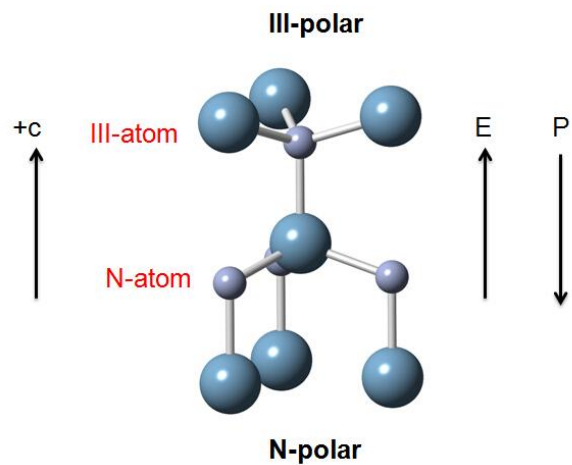


Figure 1.1. Schematic image of partial unit cell of a wurtzite III-nitride crystal.

Table 1.1. Basic properties of III-nitride material.[16]

| Material | | AlN | GaN | InN |
|---|-------------------|----------------------|----------------------|----------------------|
| Lattice parameters | $a_0(\text{\AA})$ | 3.112 | 3.189 | 3.545 |
| | $c_0(\text{\AA})$ | 4.982 | 5.185 | 5.703 |
| E_g (eV, at 300K) | | 6.00 | 3.437 | 0.6 |
| P_{sp} (C/m ²) | | -0.09 | -0.034 | -0.042 |
| Poisson ratio | | 0.203 | 0.183 | 0.272 |
| Thermal Conductivity κ at 300K (W /cm·K) | | 2.85-3.2 | 2.3 | 0.8 |
| Thermal expansion $\Delta a / a$ at 300K (K ⁻¹) | | 4.2×10^{-6} | 5.6×10^{-6} | 2.9×10^{-6} |

Due to a lack of suitable native substrates, development has been based on using foreign substrates for growing epitaxial AlGaN for UV-LEDs/LDs. Sapphire has become a common choice because of its availability with up to a few inches of diameter and a relatively low cost². However, the large lattice mismatch between underlying substrate and GaN/AlN layers is directly responsible for the large dislocation density in the film (Table 1.1). These dislocations have been proven to be deleterious to emission behavior and lifetime of LEDs and LDs[17] as they can act as recombination centers for the electron-hole pairs, thus increasing the non-radiative recombination rate.

In order to overcome the disadvantages related to foreign substrates, development of bulk AlN substrates has been pursued. However, AlN single crystal substrates have only recently become commercially available. They allow for homoepitaxy of AlN, which is the base for high-quality epitaxy of Al-rich AlGaN layers.[1, 18, 19] Using AlN substrates, atomically smooth AlN homoepitaxial layers[19, 20] and pseudomorphic, heteroepitaxial AlGaN layers[21] with superior optical and structural properties were reported.

Homoepitaxial AlN and heteroepitaxial AlGaN on c-plane AlN substrates exhibit excellent optical quality characterized by fine structure of the donor-bound exciton peaks with FWHM less than 0.5 meV and low defect luminescence.[22]

1.3 Growth of III-nitride bulk crystals and epitaxial films

AlN bulk crystals used in this work were grown by the physical vapor transport method (PVT). AlN powder was placed inside a TaC crucible inductively heated in N₂ atmosphere and the pressure varied between 400 and 1000 mbar. A polished seed was thermally fused to the crucible cap at 2250°C. Seeded growth of AlN boules can be achieved with diameters approaching 1.5 inch and an average dislocation density as low as 10³ cm⁻³, as measured by X-ray topography.[23, 24] GaN bulk crystals were grown by hydride vapor phase epitaxy (HVPE) on sapphire substrates followed by substrate removal. Gallium trichloride (GaCl₃) and ammonia (NH₃) were used as gallium and nitrogen precursors, respectively and 1-2 mm thick quasi-bulk crystals can be achieved with dislocation density of ~ 10⁶ cm⁻³. [25]

In the case of III-nitride epitaxial deposition, metalorganic chemical vapor deposition (MOCVD) is typically used. It is a common commercial technique due to large throughputs and film uniformity. In this work, all epitaxial thin films were grown in our in-house-built vertical, cold-walled, rf-heated, low-pressure MOCVD reactor. Triethylgallium (TEG), trimethylaluminum (TMA), and NH₃ were used as Ga, Al, and N precursors, respectively. The growth condition can be controlled by various parameters including temperature, pressure, V/III ratio, diluent gas and the input partial pressure of these precursors species.[19]

All these parameters can be combined in a supersaturation model proposed initially by Koukitu et al. and developed by Mita et al.[26, 27] This was used to relate film properties such as surface morphology and growth mode with the gas supersaturation value. In regards to III-nitride epitaxial thin films, growth on sapphire substrate, using a low temperature (LT) AlN nucleation layer (NL) before the growth of high temperature (HT) III-nitride films, will lead to strain relaxation induced by the lattice mismatch between the III-nitride and underlying substrate. This leads to the improvement of crystal quality and surface morphology.[28] In addition, control of the III-nitride polarity strongly relied on the LT-AlN nucleation layer. If the LT-AlN layer was properly treated, a III-polar epitaxial film could be achieved. On the other hand, when the sapphire substrates were annealed in ammonia (nitrided) at high temperature ($>950\text{ }^{\circ}\text{C}$), the subsequent epitaxial layers were N-polar, where the films exhibit a rough, hexagonal faceted surface morphology.[29, 30] This polarity control scheme is very important and it will be shown later in chapter 2 that $\text{Al}_x\text{Ga}_{1-x}\text{N}$ lateral polar structures (LPS) can be grown on sapphire substrate with alternating N- and III-polar domains of 5 μm to 50 μm . Utilizing wet etching selectivity between III-polar and N-polar, the etch rate of N-polar $\text{Al}_x\text{Ga}_{1-x}\text{N}$ can be estimated by measuring the step height changes between the III-polar and N-polar domains after etching.

$\text{Al}_x\text{Ga}_{1-x}\text{N}$ binary alloys have been pursued for their application to UV-LED and LD due to its tunable bandgap. Due to possible differences in incorporation rate between Ga and Al precursors, a linear relationship between the Al composition of $\text{Al}_x\text{Ga}_{1-x}\text{N}$ layers and the III precursors flows can be obtained only by taking into consideration a correction factor γ [31], which is depended on growth condition such as temperature and NH_3 partial pressure.

In this work, $\text{Al}_x\text{Ga}_{1-x}\text{N}$ epitaxial layers or LPS were grown on sapphire substrate with Al composition of 40%, 50%, 60% 70% and 80%.

1.4 Deep UV Light-Emitting-Diodes (LEDs)

1.4.1 Working conditions and applications

LEDs in various wavelength ranges have been developed for applications such as displays, numerical readout, bio-chemical detection and medical diagnostics.^[32] III-nitride based LEDs using $\text{In}_x\text{Ga}_{1-x}\text{N}$ within the active region emit light from the infrared to near ultraviolet depending on the indium composition in the active region. If $\text{Al}_x\text{Ga}_{1-x}\text{N}$ is used as active region, emission wavelength of 200 nm to 365 nm can be covered.

LEDs are based on electroluminescence. In the early developmental stages, LEDs were developed as simple p-n junctions. In general, n-type and p-type material is brought into contact forming a p-n junction. Under forward bias, a large population of electrons is injected into the conduction band while simultaneously holes are injected into the valence band[33] within a depletion region (Figure 1.2). Carrier relaxation and subsequent recombination of electrons and holes result in emission of photons with energy comparable to the energy of the shallow donor and shallow acceptor pair (DAP) energy of the material. It is worth noting that typically not all recombination is radiative but a fraction of the electrons and holes recombines non-radiatively, giving out heat that dissipates into the crystal lattice.

However, homojunction LEDs are inefficient since the recombination takes place in a wide region around the junction, thereby reducing internal quantum efficiency and enhancing

re-absorption.[33] Double-heterostructures (DHs) or multiple-quantum-well (MQW) structures can reduce these effects. The configuration is designed as single or multiple lower bandgap materials acting as active region, sandwiched between larger bandgap materials acting as cladding layer. By creating a reservoir of electrons and holes, the overlap of their wave functions is increased, resulting in a drastically reduced non-radiative recombination.

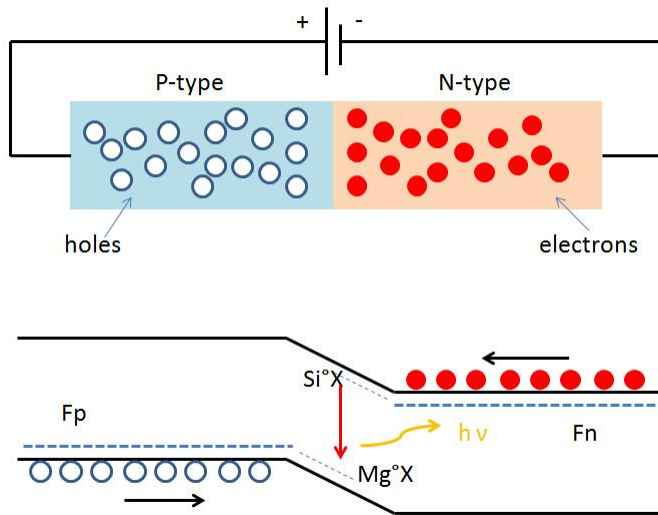


Figure 1.2. Schematic image of carrier distribution under forward bias of a p-n junction

1.4.2 Development of UV-LEDs

The fabrication of a III-nitride based blue LED was first reported by Nakamura.[34] The emission wavelength was centered at 430 nm and output power was 42 μW at a current of 20 mA. Sub-300 nm AlGaN-based deep ultraviolet (DUV) LEDs were first reported by

Zhang et al.[35] in 2002 with a 278 nm peak emission and external quantum efficiency (EQE) of less than 0.05% at 20 mA. The shortest wavelength of 210 nm was reported by Taniyasu et al.[36] four years later. Many efforts were spent on both expanding the wavelength range of UV-LEDs and increasing the quantum efficiency. InGaN-based LEDs with emission at 455 nm are reported to have EQE up to 50% and output power 25.5 mW at 20 mA and 3.1V[37] placing these devices among the most efficient machines known to man. However, compared to InGaN blue LEDs, the EQE of AlGaN-based UV-LEDs is much lower and depends strongly on the emission wavelength. A record EQE as high as 10.4% and output power of 9.3 mW at 20 mA injection current was recently reported by Shatalov[38] for 278nm AlGaN-based UV-LEDs. The reasons for low efficiency of AlGaN-based UV-LEDs are identified as:

- 1) Low injection efficiency into the MQW region caused by low concentration of holes in Al-rich p-AlGaN/p-GaN layer[39] and leakage of carriers away from the active region.
- 2) Low extraction efficiency due to high total internal reflection[39] (small extraction cone and re-absorption in the p-type contact layer).
- 3) Low internal quantum efficiency due to poor crystal quality of AlGaN epitaxial layers caused by underlying threading dislocations and point defects.[40]

Most approaches towards the fabrication of UV and DUV LEDs rely on the use of foreign substrates such as sapphire. As discussed above, bulk AlN substrates allow for high

quality AlN layers with dislocation densities $<10^3$ cm $^{-2}$. The use of these substrates is understood as a possible pathway to overcome current limitations in doping ability (by reducing compensation) and to increase crystal quality of layers and active regions. Ren[41] et al. investigated the surface morphology and strain relaxation pathways of high Al composition AlGaN epitaxial layers grown on AlN single crystal substrates. They demonstrated that the performance of deep UV LEDs on bulk AlN substrate with emission wavelength of 300 nm was superior to those grown on sapphire. Kinoshita[42] et al. reported AlGaN-based DUV-LEDs with emission as low as 268 nm fabricated on HVPE-AlN layers grown on PVT AlN crystals. The output power as high as 28 mW was obtained at an injection current of 250 mA. However, despite these exciting results, comprehensive studies on the optical properties and defect states of AlGaN epitaxial layers and MQWs grown on bulk AlN substrate was not available.

1.4.3. Definition of the quantum efficiency

The performance of an electrically driven light emitter can be evaluated by the wall-plug efficiency[43] (WPE). WPE is defined by the ratio of light output power over input electrical power. It is directly related to η_{EQE} (external quantum efficiency (EQE)) by the relationship $WPE=EQE \times$ Feeding efficiency. Feeding efficiency is the ratio of the mean energy of the photons emitted and the total energy that an electron-hole pair acquires from the power source. EQE can be expressed by:

$$\eta_{EQE} = \eta_{inj} \cdot \eta_{UQE} \cdot \eta_{extr}, \quad (1.4.1)$$

where η_{inj} denotes as the injection efficiency, the proportion of electrons or holes that are injected into the active region, η_{IQE} represents the internal quantum efficiency, which is the proportion of radiative recombination from electron-hole pairs, and η_{extr} is the extraction efficiency, or the fraction of photons escaping the device over the total amount of emitted photons. It should be noted that internal quantum efficiency (IQE) is highly dependent on the material quality, while EQE is related to light path design and packaging design of the emitters.

1.4.4 Light extraction in AlGaN-based UV-LEDs

As mentioned above, the fraction of light escaping from the device (the light extraction efficiency) plays a critical role for the experimentally observed low EQE values of DUV LEDs. Thus, increasing the extraction efficiency seems to be crucial in attempts to increase the LEDs external quantum efficiency.

The reason for the low light extraction efficiency is the total internal reflection (TIR), which occurs at the transition from a material with a high refractive index (n_1) to a material with a low refractive index (n_2). For this case a critical angle θ_c can be defined as the largest incident angle at which the light incident upon the semiconductor-air interface is not completely captured inside the semiconductor due to TIR. Its relation with the refractive index of semiconductor and air can be found with $\theta_c = \arcsin(n_2/n_1)$. The solid angle encased by the critical angle for light extraction is called the “escape cone”. If the escape cone is small, only a small fraction of light can be extracted, resulting in a low EQE. Since III-

nitrides have high refractive index as compared to sapphire, this problem becomes significant for AlGaN-based DUV LEDs grown on AlN single crystalline substrates. Assuming that the emission source is homogenous and isotropic (ignoring, e.g., reflection from the metal contact), the proportion of light extracted out can be calculated as: $\frac{2\pi r(r - r\cos\theta)}{4\pi r^2} = \frac{1 - \cos\theta}{2} = \sin^2 \frac{\theta}{2} \sim \frac{\sin^2 \theta}{4} = \frac{1}{4n^2}$. Here, r , θ , and n denote as the distance between light source and interface, incident angle, and refractive index of the LED substrate, respectively. In the case of an AlGaN-based DUV-LED on an AlN substrate with emission wavelength at 260 nm, one can estimate the extraction efficiency to be <5%, considering a refractive index of 2.3 for AlN;[44] the rest of the light falls outside of the escape cone of the device due to TIR.[45] As a result, the light is trapped inside the LED and eventually re-absorbed. Thus, the achievable EQE for conventional AlGaN based LEDs is limited to values below 5%.

It must be noted that the calculated value of 5% for the extraction efficiency only holds true for a plane and smooth semiconductor-air interface. Taking into account geometrical considerations, a suitable design can significantly increase the extraction efficiency of light out of the active region of an LED. LED research has provided different solutions, such as for example, a hemispherical dome made of resin or silicone which is usually used in the package of LEDs emitting in the visible range. In an ideal case, when the emission is considered as a point source (Lambertian source), a spherical shape dome covered on top of the LED assures that the sphere interface is perpendicular to the light direction.[46, 47]

Other methods to increase the light extraction efficiency in III-nitride based LEDs emitting in the visible include the use of a thick window layer for light extraction from the side of the film,[12] flip-chip design,[48] implementation of distributed Bragg reflectors (DBR) to reflect the light from bottom of the substrate,[49] and truncated-inverted-pyramid (TIP)[50, 51] structures. Flip-chip, wire bonding as well as micro pyramid arrays have also been discussed in regard to efficiency enhancement.[52] In addition to the sophisticated LED designs discussed above, simple surface roughening of either the window layer or substrate of LED devices has proven to be efficient in increasing light extraction efficiency. Methods to achieve surface roughening include reactive-ion etching (RIE),[53] wet etching,[54] and laser lift-off.[55] The general idea of surface roughening is that at the semiconductor-air interface, the incident angles of the light are randomized and by this escape cones are generated in different directions, increasing the probability of photons to escape from the LED.[45, 54] Many results on successful application of surface roughening are available in literature; Recently Huh et al.[45] reported that Pt metal clusters used as wet etching mask for surface roughening of the p-GaN cladding layer of InGaN-based LEDs may enhance the efficiency by 62%.

It was suggested that further improvement of the light extraction efficiency can be achieved by surface roughening via ordered or periodic structures rather than random surface roughening due to a shorter light escape path length.[56] Periodicity and feature size of the ordered structures need to be on the same order of magnitude as the wavelength of light. Therefore, periodic nanostructures are able to interact with light on a wavelength scale, allowing for better light propagation management. Possible techniques in achieving periodic

nanostructures include electron-beam lithography or nano-imprint lithography.[57-59] Byeon et al. reported that nano-imprint lithography coupled with RIE can create a square lattice array with a periodicity of 520 nm. They also showed that such an ordered roughening applied to an InGaN/GaN MQW LED with emission wavelength of 490 nm, and up to 2.6 times increase in the emission intensity can be achieved.[59]

Up to now, most of the light extraction techniques discussed above were applied to III-nitride-based LEDs emitting in the visible range. Only preliminary data on AlGaN based DUV-LEDs is available.[60-62] However, as discussed above, the light extraction efficiency plays a significant role for the EQE of DUV-LEDs which highlights the necessity of comprehensive studies. In order to get a better understanding of the influence of LED design and surface roughening mechanisms and eventually demonstrate pathways to increase the EQE in DUV-LEDs, two different techniques for increasing light extraction efficiency are discussed in this work (Chapter 2 and Chapter 3). It will be demonstrated that by applying wet or dry etching processes, the AlN substrate can be removed, thinned, or patterned, thus providing enhanced light extraction efficiency.

1.5 UV-Laser Diodes and its characterization

1.5.1 General property of stimulated emission

Despite the significant progress made in AlGaN-based DUV-LEDs,[63] electrically pumped DUV-LDs have not been realized. Generally speaking, a laser diode structure is similar to that of an LED but it requires a light waveguide, a resonant cavity created by

reflecting mirrors at each end of the waveguide, which can be as simple as cleaved semiconductor faces, and needs to support higher input and output power density. The emission characteristics of an LED and LD are different, with LD emission being sharp, polarized, and coherent.

As previously mentioned, LEDs emit light generated via spontaneous emission, where electrons located in the excited states (conduction band) recombine with holes in the ground states (valence band), emitting a photon. In contrast, laser diodes work using population inversion and stimulated emission. The basic differences between stimulated and spontaneous emission are depicted in Figure 1.3. Absorption (a) occurs when an incident photon excites an electron from the valence band into an empty state in the conduction band (or any other transition between two states such as an acceptor state.) The excited electron may recombine with the empty state in a lower band via spontaneous emission (b). In this case phase, polarization and direction of the emitted photon is random. However, if the excited state is relaxed due to the field of a passing photon,[33] stimulated emission (c) will generate a second photon with the same wavelength, same phase, same polarization and same direction as the incident photon. Following the Einstein coefficients, stimulated emission is the opposite process to absorption. Since lasers need to provide population inversion, laser diodes typically operate at higher pumping power density; lasing is only observed above the laser threshold, which depends on various factors including crystal quality.

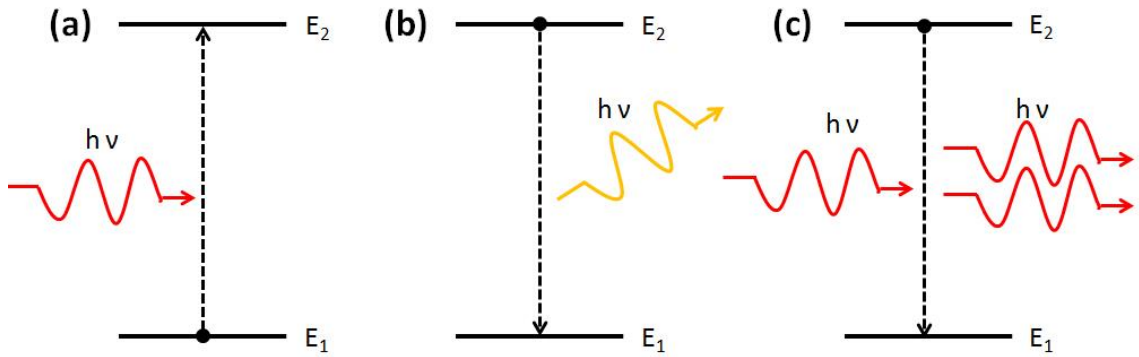


Figure 1.3. Schematic graphs showing the processes of (a) absorption, (b) spontaneous emission, and (c) stimulated emission.

The main lasing condition (population inversion) can be expressed by comparing quasi-Fermi level of the electrons and holes. Under non-equilibrium condition, one can define the electron and hole distribution via the quasi-Fermi levels:

$$f_n(E) \cong \exp\left(\frac{E_{fn} - E}{k_B T}\right) \quad (1.5.1)$$

$$f_p(E) \cong \exp\left(\frac{E - E_{fp}}{k_B T}\right), \quad (1.5.2)$$

where E_{fn} and E_{fp} are quasi-Fermi levels for electrons and holes, respectively. $E_{fn} - E_{fp}$ represents the degree of deviation from equilibrium. Absorption rate and stimulated emission rate can then be expressed by:

$$r_{abs} = P[1 - f_n(E_2)]f_p(E_1)N_p(E) \quad (1.5.3)$$

$$r_{st} = Pf_n(E_2)[1 - f_p(E_1)]N_p(E), \quad (1.5.4)$$

where P is the transition probability and $N_p(E)$ is the density of photons of energy $h\nu$. In order to have net light amplification, more light needs to be generated via stimulated emission than it is absorbed. Thus, the condition $r_{st} > r_{abs}$ must be met. Careful comparison shows that for lasing the condition $E_{fn} - E_{fp} > E_g$ has to be achieved. This means, that the quasi-Fermi level separation must be larger than the bandgap and the energy of the emitted photons in order to achieve lasing. This is called population inversion. Population inversion is a necessary condition for lasing, but not sufficient. Another important condition, optical gain will be introduced in the following section.

1.5.2 Optical gain and laser diode structure

Lambert-Beer's law describes the change of light intensity when it passes through an absorbing material:

$$I = I_0 \exp(-\alpha x), \quad (1.5.5)$$

where I_0 is the incident intensity at $x=0$ and α is absorption coefficient of the medium. Taking into account that absorption and stimulated emission are opposite but similar processes, this equation can be used to understand lasing as well. For a laser, α is interpreted as the gain value and may be written as:

$$\alpha = (N_1 - N_2) \frac{B_{21} n_r}{c}. \quad (1.5.6)$$

Here, N_1 and N_2 are electron populations at ground state and excited state and, B_{21} is the Einstein coefficient for stimulated emission with recombination from level 2 to level 1. In the case of population inversion $N_2 > N_1$, we can obtain the gain coefficient (material gain) g as:

$$g = -\alpha = (N_2 - N_1) \frac{B_{21} n_r}{c}. \quad (1.5.7)$$

In this case, the light intensity changes as a function of distance in the gain medium as:

$$I = I_0 \exp(gx). \quad (1.5.8)$$

The gain coefficient represents the material's capability in light amplification. Positive gain value is a prerequisite to achieve lasing in a semiconductor laser diode.

A common laser bar structure is shown in Figure 1.4. The structure consists of an optical cavity where stimulated emission takes place. The cavity has the length L and is fabricated either by RIE or cleaving. The length of the cavity determines the separation of longitudinal modes and can be described as:

$$\Delta\lambda \sim \frac{\lambda^2}{2Ln_{eff}}. \quad (1.5.9)$$

The width, W , of the cavity defines the transversal modes. For single mode lasers, the relationship between W and emission wavelength λ can be described as:

$$W \cdot \sqrt{n_{ridge}^2 - n_{etched}^2} < \frac{\lambda}{2}. \quad (1.5.10)$$

where n_{ridge} and n_{etched} represent refractive index of the ridge waveguide region or etched region (air or oxide passivation layer).

Metal contacts are deposited on n and p-type cladding regions which have a larger bandgap than the active region. If the laser is pumped (electrically or optically), light is emitted through the front mirror. At first, some photons are generated via spontaneous emission in the active region which in this case is illustrated as a MQW. These emitted photons travel back and forth in the waveguide region and are reflected at the mirrors. If population inversion is reached, stimulated emission will take place. Eventually the pump power reaches the laser threshold value and the device starts lasing. The device shown in Figure 1.4 is a typical edge emission laser diode, which is named so because the emission is extracted from the edge of the structure. It needs to be noted that this is different from the case of LED where light is emitted in all directions (because it is dominated by spontaneous emission) and the light is mainly extracted from the back surface (through the substrate).

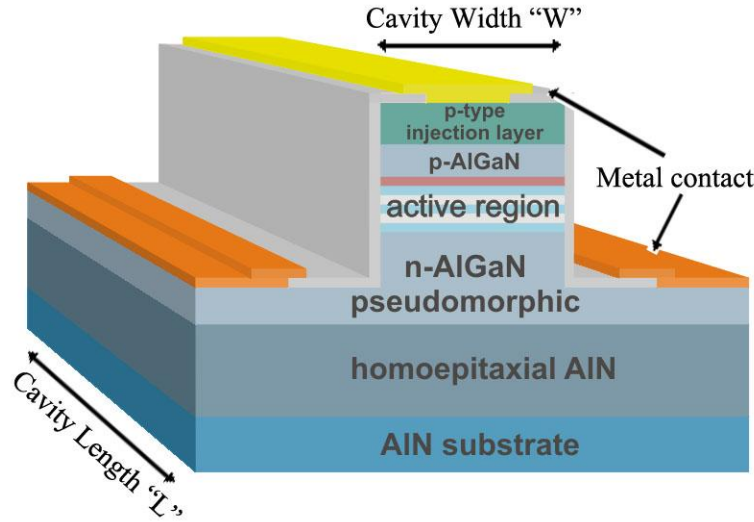


Figure 1.4. Structure of an AlGaN-based DUV edge emission laser diode showing the stack design, laser cavity and metal contacts.

Losses in the laser structure include emission through the back and front mirror, re-absorption in the waveguide, and scattering. Taking into account material's gain and these losses, after one round trip inside the cavity, the light intensity is given by:

$$I = I_0 R_1 R_2 e^{2(g-\gamma)L}. \quad (1.5.11)$$

where R_1 and R_2 are the reflectivity of the front and back mirrors and γ represents waveguide losses including re-absorption and scattering. In order to maintain the intensity of emitted light (I is equal to I_0) the losses and the gain must cancel each other. This gives the definition of the threshold gain value:

$$g_{threshold} = \gamma + \frac{1}{2l} \ln \frac{1}{R_1 R_2}. \quad (1.5.12)$$

In other words, a device will only lase if the gain is greater than the threshold gain $g > g_{\text{threshold}}$.

1.5.3 Deep UV laser diodes applications

Laser diodes are widely used for applications such as free-space communication, laser pointers, CD/DVD/Blu-ray reading/writing, curing, laser printing, scanning, high-density data storage[64, 65] etc. Since bio-molecules and DNA have strong absorption and resonance at wavelengths around 240 -260 nm, DUV-LDs are very promising for applications in biological or chemical detection. However, no DUV-LDs with emission below 300 nm are available. The reasons for the unavailability of DUV laser diodes are similar to those listed for LEDs and include the growth of high quality AlGaN epitaxial layers as well as effective n- and p-doping in providing enough carrier injection in the active region. It should be pointed out that because LDs work at higher input power to achieve population inversion, their operation is much more sensitive to material quality.[40]

Optically pumped stimulated emission from GaN was first observed in 1971 by Dingle et al.,[66] yet, due to a lack of sufficient p-doping capabilities, electrically injected LDs were not reported until 1996 by Nakamura.[10] Optically pumped AlGaN or AlGaInN based UV-LDs with wavelength ranging from 240 nm to 370 nm were reported by various groups.[67-69] The shortest wavelength of electrically pumped LDs only reached 336 nm, even though the shortest wavelength of 237 nm optically pumped AlGaN based LD grown on AlN single crystal substrate was recently reported.[70] Reduction of dislocation density in the active AlGaN layers in DUV-LDs via growth on bulk AlN substrates is envisioned as

pathway to reducing the lasing threshold. Efforts have been made by various groups and reports include the work of Wunderer et al. who reported an optically pumped laser diode grown on AlN substrates with emission wavelength of 267 nm and threshold power density of 126 kW/cm^2 .[71] Similarly, Xie et al.[72] reported that by using single crystalline AlN substrates with threading dislocation densities of less than 10^4 cm^{-2} record low thresholds of 84 kW/cm^2 for optically pumped 264 nm laser structures can be achieved.[73, 74]

Despite these encouraging results, the challenges for the growth of DUV LDs are still tremendous. First of all, effective p type doping is hard to realize in DUV LDs and hinders hole injection due to high activation energy of accepter states and formation of compensation defects. Secondly, there is still lack of understanding of stimulated emission, optical gain and polarization characteristic for the emission from AlGaN epitaxial layers and their heterostructures. Systematic studies of the gain spectra of AlGaN and its heterostructures on AlN substrates is crucial in providing in-depth understanding of the intrinsic properties of this material system and guidance for future device development. Thus, in Chapter 4, the stimulated emission, optical gain spectra, and polarization properties of AlGaN epitaxial layers grown on AlN single crystalline substrate are presented. Simulation result on gain spectra as well as optical confinement will also be presented in comparison with experimental data, and comments on optimal LD structure design will be provided.

CHAPTER 2 Selective wet etching of AlN, GaN, and $\text{Al}_x\text{Ga}_{1-x}\text{N}$

2.1 Substrate removal for light extraction enhancement in DUV-LEDs

Due to a lack of suitable native substrates, foreign substrates have been used for epitaxial growth of AlGaN based UV LEDs and LDs. Sapphire is a common choice because of its availability with diameters of up to 4 inches[75] and a relatively low costs. However, the large lattice mismatch between the substrate and the AlGaN films leads to a large dislocation density in the films. Dislocations have been proven to be deleterious to emission behavior of LEDs/LDs[17] as they can act as non-radiative recombination centers for electron-hole pairs and leakage paths, and significantly reduce the efficiency and lifetime of the devices.

Recently, AlN single crystal substrates grown by the physical vapor transport (PVT) method with sufficient size and quality have become available allowing for homoepitaxial growth of AlN. They are a prerequisite for the growth of high-quality AlGaN epitaxial layers[1, 18, 19] used for DUV-LEDs and LDs. Consequently, atomically smooth AlN[19, 20] and pseudomorphic AlGaN layers[21] grown on the AlN bulk substrate were reported and dislocation distribution and strain relaxation in such layers were also discussed. Taking the advantage of high crystalline quality AlN substrate, electrically driven AlGaN based DUV LEDs[1] at emission wavelength of 265 nm were successfully fabricated and optically pumped AlGaN based DUV LDs[4] with sub-300 nm emission were demonstrated.

Although the quality of epitaxial AlGaN layers is superior, DUV-LEDs grown on bulk AlN are not commercially available yet. Since the LED light is typically coupled out through the back-side, impurities in the substrate, which cause a high UV absorbance, are found to be a major challenge in LED fabrication. Specifically, a strong UV absorption band around 265 nm in AlN single crystal substrates limits the efficiency (EQE and WPE) of DUV-LEDs. Recently, it was shown that substitutional carbon on the nitrogen site of AlN is responsible for this absorption band.[76] However, carbon is a common impurity during the growth of bulk AlN. Thus, a reduction of carbon to suppress the DUV absorption seems challenging. A possible alternative to address this problem would be to develop a selective etching process which would sufficiently thin or even remove the AlN substrate and consequently reduce the absorption in the device.

Established methods for substrate removal for III-nitride devices include laser-lift-off, reactive ion etching (RIE), and wet etching. Laser-lift-off has been used for removing sapphire substrates. The illumination of the dislocation-rich GaN at the sapphire-GaN interface with pulsed (high power density) UV light leads to a local decomposition of the GaN, which facilitates lift off.[77] However, due to a lack of dislocations and contrast at the AlN/AlN interface, this technique is not expected to work for homoepitaxially grown films on AlN substrates. RIE suffers from a relatively low etching rate and introduction of plasma-related damage.[78] Besides, RIE etching provides no selectivity between the AlN substrate and AlGaN layers, which would necessitate a highly controlled and uniform process. Compared to these techniques, wet etching has the advantage of low surface damage and low cost while being readily available for large area fabrication.

Although long discussed and applied throughout literature, wet etching of nitrides is challenging and not fully understood. Due to the strong bonding, III-nitrides are usually inert to chemical attack at room temperature.[79] Therefore, in most cases, wet etching of III-nitride materials involves immersion of the sample into aqueous etchants or molten salts at elevated temperatures. Zhuang et al. reviewed etching of bulk AlN crystals and epitaxial layers in potassium hydroxide (KOH).[80, 81] A defect-selective etching behavior was proposed. Etching hillocks of various sizes were observed on the N-polar surface and hexagonal etch pits were observed on the Al-polar surface. Furthermore, a higher etching rate of the N-polar over the III-polar surface was observed. Similar behavior and etch morphology was also observed in KOH [82, 83] or H₃PO₄ [84] etched GaN epitaxial layers and bulk crystals.[85]

However, the above aggressive etching technique cannot serve the purpose of controllable selective etching in material processing and device fabrication. There are only limited reports on wet etching of III-nitrides in aqueous solutions.[86] Etch behavior of AlN and GaN is still not well established and no systematic study on selective etching of AlN compared to GaN and AlGaN, which can be applied to substrate removal or thinning in AlGaN-based devices, is available. Additionally, no data about the influence of the crystal quality (specifically dislocation density) on the etching behavior of AlN and GaN is available. However, if defect-selective etching is prevalent and the dislocation density is decreased from 10⁹ cm⁻² (heteroepitaxial thin films[87, 88]) to less than 10⁴ cm⁻² (i.e. PVT grown AlN), etching behavior is expected to be different.[89, 90] Therefore, it is crucial to develop an etching process for high-quality AlN and GaN bulk crystals under mild and

controllable conditions to achieve a smooth surface with well-known removal rates, while avoiding damage to the device layers during substrate removal.

In this chapter, the KOH wet etching behavior of III-Nitride crystals, including etch rate, selectivity, surface morphology, crystallographic planes, surface stoichiometry as well as the influence of dislocations on the etching behavior are discussed. The etch rate of N-polar and III-polar high-quality AlN and GaN single crystal substrates and selectivity in AlN and $\text{Al}_x\text{Ga}_{1-x}\text{N}$ epitaxial layers are compared. Based on the observations, a novel etching mechanism is proposed and the potential of KOH etching to remove the AlN substrate in DUV-LED fabrication discussed. This is the first comprehensive study of this sort on high-quality III-nitride crystals and in absence of copious dislocations.

2.2 Experimental design

In order to be applicable for the removal of AlN substrates from DUV-LEDs, a mild and controllable etching with smooth etch surface is desired. Due to advantageous surface morphology and lower impurity incorporation, III-nitride devices are typically grown in the III-polar direction. Thus, for native substrates, the N-polar side is on the back side. In order to avoid any damage to the LED itself and to ensure a sole removal of the substrate, a high selectivity between N-polar and III-polar material is crucial. Furthermore, a high selectivity between the AlN substrate and $\text{Al}_x\text{Ga}_{1-x}\text{N}$ cladding layers with a significantly higher etching rate of AlN compared to $\text{Al}_x\text{Ga}_{1-x}\text{N}$ or GaN is also desired. This would allow for a complete removal of the substrate where the cladding layer would act as an etch stop. Last but not

least, a smooth and uniform etch surface is needed for uniform light extraction and heat dissipation.

High quality AlN and GaN bulk crystals were used for this etching study. GaN single crystal wafers were obtained from *Kyma Inc*. These wafers were grown by hydride vapor phase epitaxy (HVPE) on sapphire substrates with subsequent substrate removal.[91] AlN single crystal wafers were obtained from *Hexatech Inc*. Single crystalline AlN boules were grown by PVT and wafers were obtained by cutting the boules perpendicular to the c-axis with off-cut of $\sim 0.7^\circ$ toward the m-plane. Eventually, a combination of mechanical and chemo-mechanical polishing (CMP)[19] ensured that the AlN and GaN wafers could be considered “epi-ready”. Figure 2.1 shows an optical image of the GaN and AlN single crystal substrates. Dislocation densities for the AlN and GaN wafers were estimated to be lower than 10^4 cm^{-2} and 10^6 cm^{-2} , respectively.[24, 25, 91] These wafers were diced into small pieces and weighed before being immersed into either KOH aqueous solution or a combination of KOH and H₂O₂ aqueous solution. The etching was followed by DI water rinsing for 5 min and N₂ gas blow-drying. The etch rate was determined either directly from a change of the thickness of the wafer or indirectly from the weight change:

- For the thickness change method, the N-polar or metal-polar face were partially covered by 50 nm Ti/ 10 nm Au deposited by e-beam evaporation to act as an etching mask. Following the KOH etching and cleaning, the metal mask was removed in a hot HCl solution and then the step height was recorded using a Veeco Dektak 150 Profilometer.

- For the weight change method, which aims at the calculation of an overall etch rate of AlN and GaN, the etching depth r was calculated as $r = \Delta w / \rho A t$. Δw is the weight loss of the sample after etching, which was measured by a Mettler Toledo Microbalance XS105 series with 10 µg resolution, ρ is the density of the wafer, t is the etching time, and A is the area of the basal plane. Here, A is considered constant even for the long periods of etching. This is based on the fact that the etching of the side facets of the wafer can be neglected because of a comparably smaller surface area and relatively low etching rate.

Measurement errors of the etching rate may originate from systematic errors of micro-balance and optical microscope when the sample weight and basal plane area are determined.

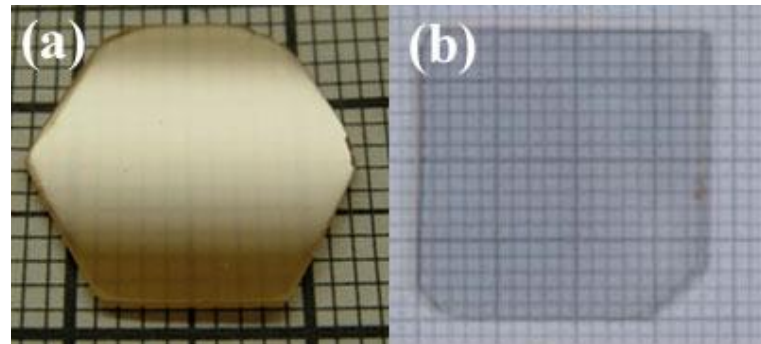


Figure 2.1. Image of the AlN and GaN bulk wafer used to investigate etching behavior.

AlGaN bulk crystals are not available. Consequently, investigation of the etching selectivity between AlN and $\text{Al}_x\text{Ga}_{1-x}\text{N}$ ($0 \leq x \leq 1$) was performed using epitaxial films with thickness around 800 nm grown by MOCVD on 2-inch sapphire substrates. Using XRD, the

dislocation density of these films was estimated to be around 3×10^{10} cm $^{-2}$.^[92] The investigated films were fabricated as Lateral-Polarity-Structures (LPS) with alternating 10 μm wide III-polar and N-polar stripes.^[93] In order to determine selectivity and etching rates, substrates with epitaxial films were cut into small pieces and immersed into KOH aqueous solution. Due to the inertness to etching of the III-polar material, LPS are ideal structures for KOH etching experiments. The change of the height difference between the III-polar and N-polar stripe is a simple but reliable measure of the etching rate. An optical microscope image of an as grown Al_{0.6}Ga_{0.4}N LPS (a) and of the structure after 5 min KOH etching (b) is shown in Figure 2.2. The 10 μm wide stripes with alternating III-polar and N-polar orientation can be clearly distinguished. After the KOH etching procedure, the III-polar material remains unchanged. In contrast the N-polar stripes are significantly darker. Cross sectional SEM images (not shown) indicated that the KOH etching led to a significant removal of the N-polar AlGaN while the III-polar material was not altered. Further details are discussed below.

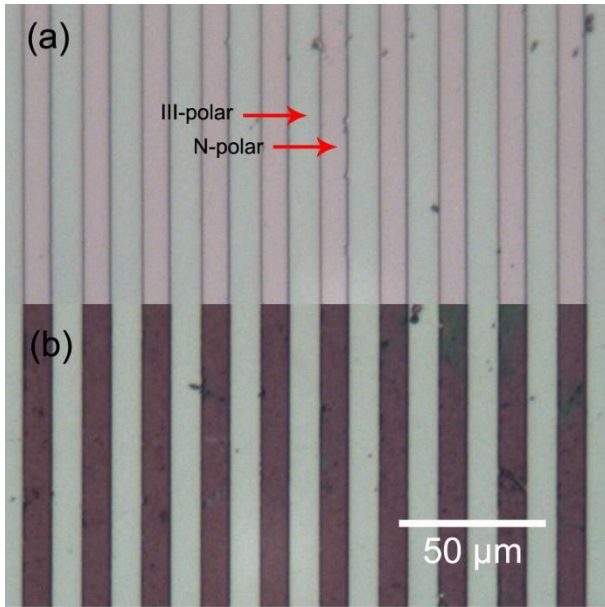


Figure 2.2. Optical micrograph of an $\text{Al}_{0.6}\text{Ga}_{0.4}\text{N}$ LPS with $10 \mu\text{m}$ stripes before KOH etching (a) and after KOH etching (b).

The surface morphology of the etched AlN and GaN bulk crystals was characterized by an Olympus BH-2 differential interference contrast (DIC) optical microscope, a JEOL JSM-6400 Scanning Electron Microscope (SEM) operating at 5 kV and a JEOL JSPM-5200 Atomic Force Microscope (AFM) working in tapping mode. The N-polar AlN surface chemistry was characterized by X-ray Photoelectron Spectroscopy (XPS) to determine the molar ratios and bonding of Al, O and N after etching in KOH and KOH/H₂O₂ solutions. A VG Instruments hemispherical analyzer and an x-ray source producing Al K α radiation housed in an analysis chamber with 10^{-10} Torr base pressure, were employed. The spectrometer work function was calibrated using Au 4f_{7/2} photoelectron line at 84.0 eV. All reported binding energies include correction for sample charging determined by the binding

energy shift in the adventitious C 1s line from 284.6 eV. All spectra were fitted with Voigt profiles. Low resolution survey scans and high resolution core level spectra were acquired using pass energies of 50 eV and 20 eV, respectively. Finally, the relationship between the etching hillocks and underlying dislocations were investigated by looking at cross-section two-beam bright field and dark field Transmission Electron Microscopy (TEM) on etched N-polar AlN. $g=(1-100)$ and $g=(0002)$ imaging conditions were applied to distinguish the screw type and edge type dislocations.

2.3 The influence of the Al composition on the etch rate and selectivity

The etch rates of AlN and GaN single crystal substrates for both polarities in a 1 wt% KOH solution at 70°C are shown in Table 2.1. The N-polar surface has an etch rate exceeding 500 nm/min for AlN and 40 nm/min for GaN. In contrast, the etch rate of the metal polar surface is found to be below 2 nm/min for both AlN and GaN. These results are consistent with previous reports claiming that the N-polar GaN or AlN etch significantly faster than the respective metal-polar surfaces.[80] The extremely high etching selectivity between N-polar and III-polar in III-nitride crystals were attributed to the different bonding conditions of N-polar and III-polar surfaces. It was claimed that hydroxide ions in KOH solutions has difficulties in approaching and thus attacking metal atoms in III-polar III-nitride due to a large repulsion between negatively charged OH- ions and three occupied dangling bonds of nitrogen.[94] However, in the N-polar surface, there is only one dangling bond on top of nitrogen atom, thus chemical attack becomes easier.[94] As mentioned above, the Al-polar surface on AlN single crystal substrates is usually used for the epitaxy needed

for the fabrication of LEDs, thus, the selectivity between the N-polar and metal-polar surfaces is found to be sufficient to remove the AlN substrate while keeping the metal-polar epitaxial layer practically intact.

Table 2.1 also indicates that the overall AlN etch rate was much higher than that of GaN under the same conditions. Comparing AlN and GaN a high etching selectivity of 13 is demonstrated. Based on the Arrhenius equation, the activation energies of wet etching GaN and AlN were experimentally determined to be 0.59 eV and 0.67 eV, respectively. The ratio of AlN/GaN etching activation energy of ~1.14 agrees well with the atomic bond strength difference,[95] but actually in contrast with the etching selectivity. Therefore, it is reasonable to believe that wet etching of III-nitride is more likely to be controlled kinetically instead of thermodynamically. It has widely been accepted that the wet etching of III-nitride happens in the format below:[94]



KOH acts as a catalyst and also dissolves Ga_2O_3 or Al_2O_3 forms on N-polar surface. In fact, XPS was conducted on etched N-polar AlN surface (as shown in section 2.5), demonstrating a 20% mole fraction of oxygen. The mole fraction of oxygen on top of N-polar GaN was previously reported to be 10%,[94] indicating that Al_2O_3 or $AlO_x(OH)_y$ are more likely to form than Ga_2O_3 , which agrees well with the high etching selectivity between

AlN and $\text{Al}_x\text{Ga}_{1-x}\text{N}$ / GaN. These observations make wet etching a promising method for substrate removal for LEDs grown on AlN.

Table 2.1. Wet etching rate of the N-polar and III-polar surface of AlN and GaN single crystal substrates in 1 wt% KOH at 70°C.

| | Etch rate (N-polar) [nm/ min] | Etch rate (metal-polar) [nm/ min] | Polar selectivity (N / III) |
|-----|----------------------------------|--------------------------------------|-----------------------------|
| AlN | 500±150 | 1.6±0.6 | ~300 |
| GaN | 40±4 | 1.9±0.3 | ~20 |

Hydrogen peroxide (H_2O_2) is known to be a strong oxidizer. It was also reported that adding H_2O_2 into an acid solution could introduce an etching selectivity between different materials due to the intentionally enhanced oxidation behavior.[96, 97] It was proposed that adding hydrogen peroxide into KOH may lead to a further increase of the selectivity in III-nitrides as well. However, there are no reports on the etching behavior of an H_2O_2 /alkaline solution for nitride materials. Using the setups and samples described above, H_2O_2 was added into KOH aqueous solution. For a mixture with final H_2O_2 concentration of 10 wt%, the etch rate, surface morphology, and surface stoichiometry of GaN and AlN were investigated.

Figure 2.3 shows a comparison between the etch depth obtained from KOH and KOH/ H_2O_2 solution as a function of etching time for N-polar AlN and GaN. A non-linear etch rate for longer etching times is observed for both AlN and GaN. Again, the observed etch rate of AlN is about 30 times higher than that of GaN independent of the used solution. In addition, an increased etching rate of the KOH/ H_2O_2 solution is observed. H_2O_2 leads to

approximately 120% greater etching depth for AlN and 30% greater depth for GaN. A possible explanation of the higher etch rate due to the addition of H₂O₂ is based on its ability of being an oxidizer. An oxide formation due to the H₂O₂ on top of the N-polar surface is proposed. This oxidized surface is more vulnerable to KOH which in return leads to the observed higher etching rate. The increased etching selectivity between AlN and GaN confirms the proposed mechanism of oxidation since the formation of oxygen-aluminum compounds is energetically more favorable than gallium-oxygen compounds,[98] which indicates a stronger oxidation of AlN.

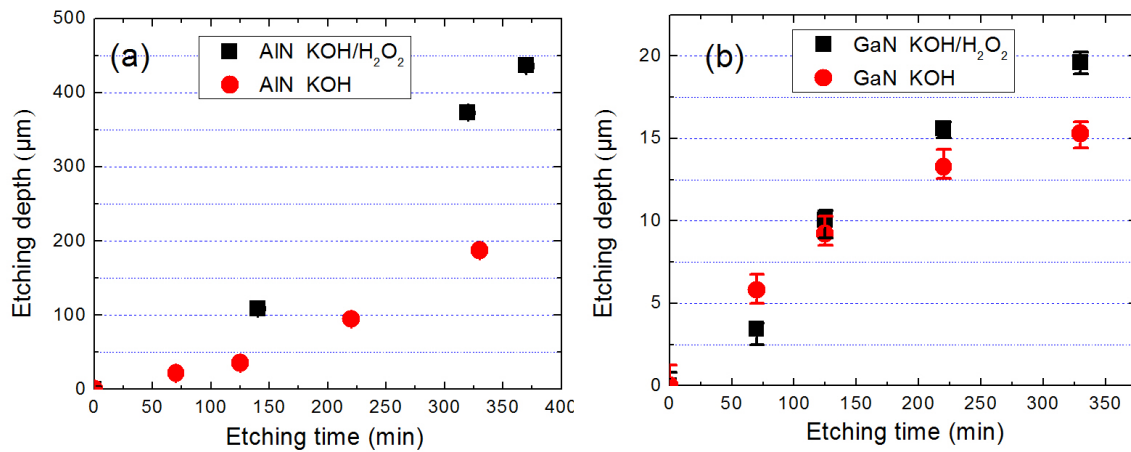


Figure 2.3. Etch depth versus etching time for AlN (a) and GaN (b) single crystal substrates in KOH and KOH/H₂O₂ solutions at 70°C.

To further investigate the etching selectivity between AlN and Al_xGa_{1-x}N, similar wet etching was performed on Al_xGa_{1-x}N LPS grown on sapphire substrates. Due to the relatively small thickness of the Al_xGa_{1-x}N LPS of around 800 nm, a reduced etching rate was desired.

This was achieved by using a lower KOH weight concentration (0.5 wt %) and lower temperature (50°C). The selectivity between N-polar AlN over N-polar $\text{Al}_x\text{Ga}_{1-x}\text{N}$ as a function of Al composition is shown in Figure 2.4. An etching selectivity greater than 1 is observed over the full compositional range of AlGaN. It is further observed that the selectivity increases as Al composition decreases. Large error bars came from the thickness measurement due to the pyramidal etching morphology. The etching selectivity between AlN and GaN LPS is approximately 12 ± 2 . Considering etching of AlN and GaN bulk crystals under KOH solution, etch selectivity between N-polar AlN and GaN is approximately 13, which fits well with the data achieved in $\text{Al}_x\text{Ga}_{1-x}\text{N}$ LPS. Dislocation densities inside AlGaN LPS are several magnitudes higher than that of bulk AlN and GaN material, yet the selectivity remains the same, indicating that under this mild etching condition, dislocation does not play a role in etching behavior. The formation and development of etching hillocks could only be attributed to different bonding conditions of crystallographic planes, which is an intrinsic property of III-nitride crystal structure.

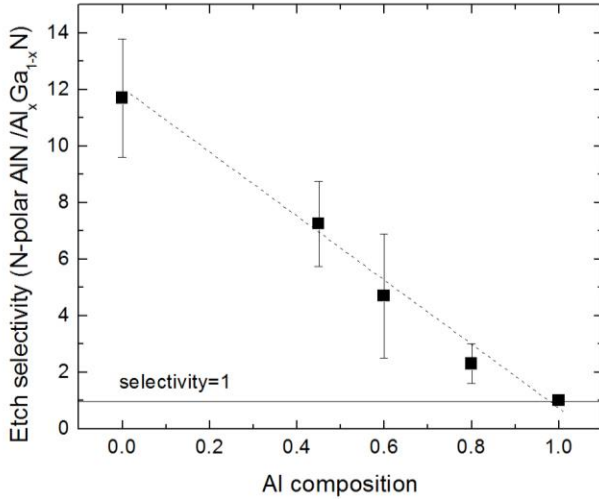


Figure 2.4. Etch selectivity ($\text{AlN}/\text{Al}_x\text{Ga}_{1-x}\text{N}$) as a function of Al composition under KOH (0.5 wt%, 50°C) etching condition.

2.4 The influence of KOH etching on the surface morphology

Knowing the surface morphology of an etched semiconductor is crucial to understand the underlying etching processes and assess the applicability of the method for device processing. Figure 2.5 shows AFM images of the Ga-polar surface of a GaN substrate before and after KOH/H₂O₂ etching. It is important to remember that the metal-polar AlN and GaN surfaces are practically inert to wet etching for standard etching times (Table 2.1). A flat surface with bilayer steps was observed for the un-etched sample. The spacing of the steps strongly depended on the miscut of the crystals and varied across the samples. Etching of the wafer in a KOH/H₂O₂ solution at 70°C for 30 minutes led to an increase of oxides and hydroxides on the surface (white dots in Figure 2.5) and a reduction of the bilayer step structure. The RMS roughness of the surface on a 5×5 μm² scan before and after etching in

KOH/H₂O₂ was 0.08 nm and 0.27 nm, respectively. This suggested that the KOH-based solution does not alter the morphology of the Ga-polar surface. A similar behavior was observed for the Al-polar AlN surface (not shown).

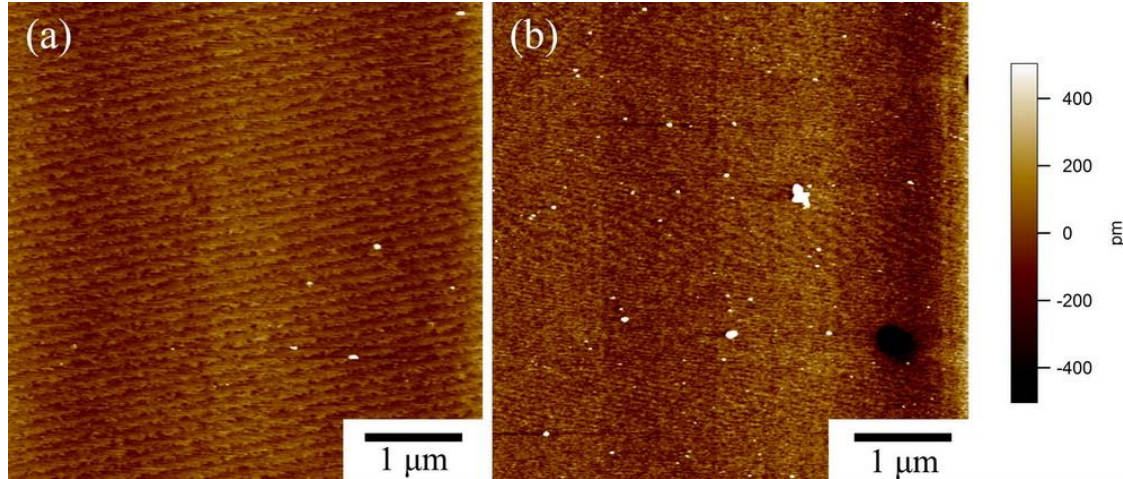


Figure 2.5. AFM images of Ga-polar GaN before (a) and after KOH/H₂O₂ etching for 30min (b).

Due to the high etch rates, the N-polar surfaces of AlN and GaN undergo significant changes if exposed to the KOH/H₂O₂ solution. Figure 2.6 shows SEM micrographs of N-polar AlN and GaN etched in KOH and KOH/H₂O₂ solutions at 70°C for 60 minutes. After etching, the N-polar surfaces are covered with oriented hexagonal hillocks. Orientation of the hillocks followed the main crystallographic axis of the wafer. Size and distribution of the hillocks varies locally and throughout the wafer and no obvious grouping is recognized. For the N-polar AlN surface, the 1 wt% KOH solution creates hillocks with diameters ranging from 1–10 μm. The hillock size decreases dramatically to approximately 0.1–3 μm when the

KOH/H₂O₂ solution is used instead. This suggests a smoothening effect related to the oxidization ability of the hydrogen peroxide. It is also worth noting that the hillocks on the KOH/H₂O₂ etched N-polar AlN surface exhibit a reduced symmetry and seem to be distributed even more randomly compared to the KOH etched surface. Obviously, the pyramid-shaped hillocks tend to decompose into smaller structures if H₂O₂ is involved in the etching process. The formation mechanism of the hillocks and the smoothening effect of H₂O₂ will be discussed in the next section 2.5.

The N-polar GaN surface exhibits hillocks with sizes around 5 μm. Overall the surface looked less random compared to N-polar AlN. Adding H₂O₂ hardly altered the size and distribution of the hillocks. A hillock density of $5 \times 10^6 \text{ cm}^{-2}$ was observed for the KOH etched AlN and both etched GaN surfaces presented in Figure 2.6. An increased hillock density of $2 \times 10^7 \text{ cm}^{-2}$ was observed for KOH/H₂O₂ etched AlN. Both of these values are significantly larger than the dislocation density of the AlN and GaN bulk crystals. This indicates that for samples with low dislocation density the KOH etching process is unlikely to be related to these dislocations.

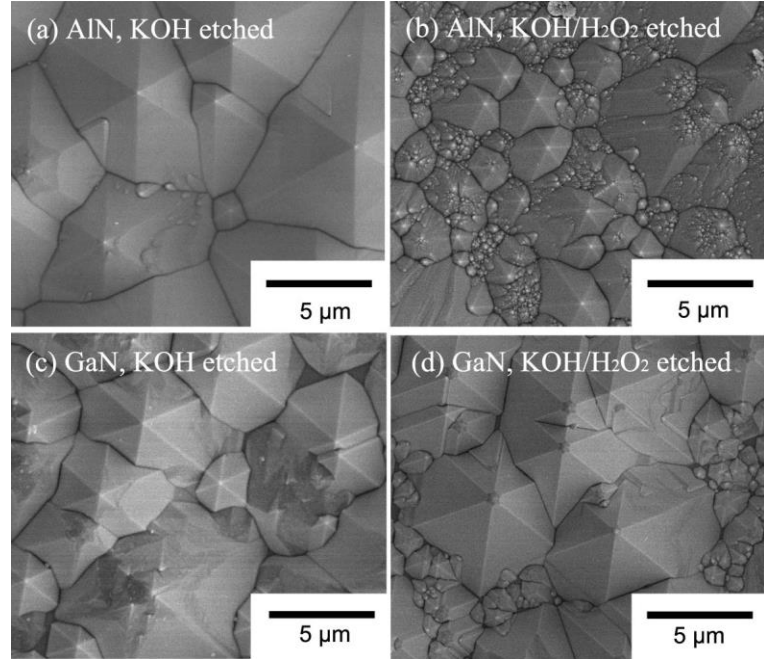


Figure 2.6. SEM micrographs of N-polar AlN etched in KOH (a), KOH/H₂O₂ (b) and N-polar GaN etched in KOH (c), KOH/H₂O₂ (d) at 70°C for 60min.

The surface morphology of an AlN LPS and a GaN LPS before and after KOH etching are shown in Figure 2.7. The as grown N-polar face of AlN and GaN epitaxial films on sapphire show a columnar structure (Figure 2.7(a)) and hexagon shape structure (figure 2.7(c)), respectively. In contrast, the metal polar surfaces look smooth and fully coalesced. AFM measurements confirm these observations as they reveal an RMS roughness below 0.5 nm for the III-polar surface and an RMS roughness above 10 nm for the N-polar surfaces. The observed surface roughness is related to the growth mode of N-polar material. It is believed that it could be optimized using appropriate growth conditions.

After etching for 2 minutes under a mild condition with 0.5 wt% KOH at 50°C, etching hillocks can be observed only on the N-polar surfaces of the AlN and AlGaN LPS. At the inversion domain boundary between the N-polar and Al-polar AlN an etching sidewall starts to appear (indicated by the red arrow in Figure 2.7(b)), indicating that the N-polar AlN etches faster than the Al-polar material. For the GaN LPS, the height difference between the Ga-polar and N-polar material hardly changes. This observation corresponds to the larger etch rate of AlN over GaN; etching time and conditions are too weak to allow for significant N-polar GaN height change. It is worth noting that the selectivity between the N- and III-polar materials is still existent despite the fact that the surfaces of as-grown N-polar AlN and GaN epitaxial films are different to those of bulk crystals. Therefore, wet etching behavior does not depend on the surface morphology of the as grown crystal, but rather depends on the Al composition in $\text{Al}_x\text{Ga}_{1-x}\text{N}$.

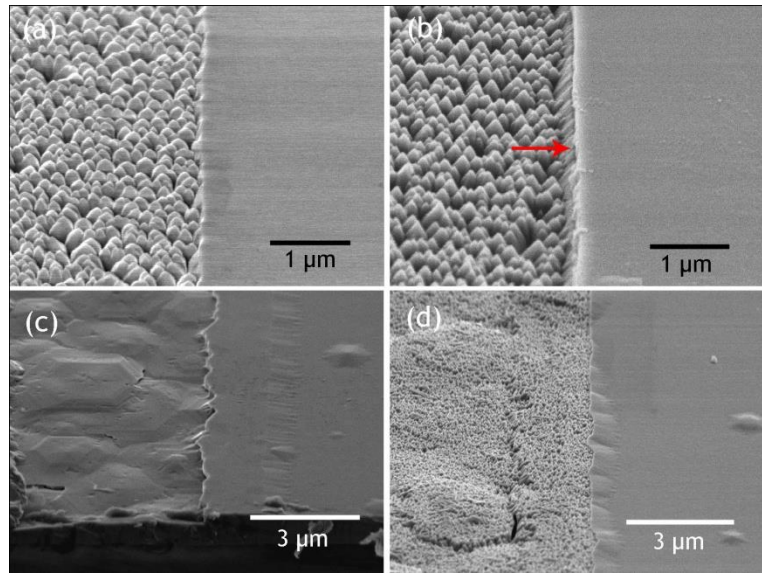


Figure 2.7. 60° tilted SEM micrographs of $\text{Al}_x\text{Ga}_{1-x}\text{N}$ LPS grown on sapphire substrate, when $x=1$, before etch (a), $x=1$, after etch (b), $x=0$, before etch (c), $x=0$, after etch (d). N-polar was shown on the left while III-polar was shown on the right within each image

In order to better understand the KOH etching mechanism and the formation of the hexagonal hillocks, SEM was performed on cleaved N-polar AlN and GaN after immersing the samples into the KOH solution at 70°C for 60 min (Figure 2.8). The angle θ between the basal plane and the edge of bounding pyramids was measured to be $58\pm2^\circ$ and $60\pm2^\circ$ for AlN and GaN samples, respectively. Based on the results from Figure 2.8 a schematic of the etching hillocks was developed and shown in Figure 2.9 (a). The values for the angles θ correspond to 63° and 62° for the angles between the basal and bounding pyramidal planes for AlN and GaN samples, respectively (indicated in figure 2.9 (b) as angle φ). In a perfect wurtzite AlN and GaN crystal, the angles φ between the $\{000\bar{1}\}$ and $\{10\bar{1}\bar{1}\}$ planes are 61.6° and 62° , respectively. These values are very close to the estimations from the SEM images.

This indicates that the pyramids are formed by the $\{10\bar{1}\bar{1}\}$ family of planes. Compared to the $\{000\bar{1}\}$ basal planes, these semi-polar pyramidal planes have smaller number of crystal bonds and are chemically more stable.

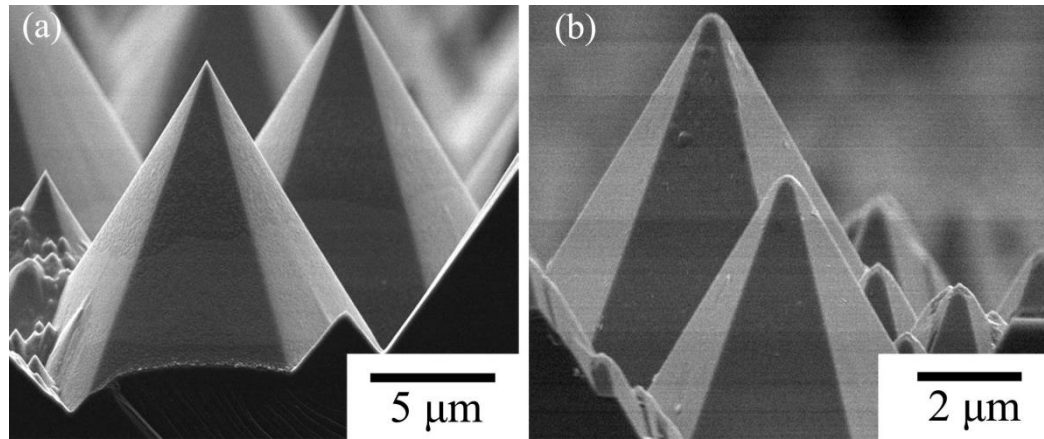


Figure 2.8. SEM cross-sectional images of hillocks on N-polar AlN (a) and N-polar GaN (b) after etching in KOH at 70°C for 60 min.

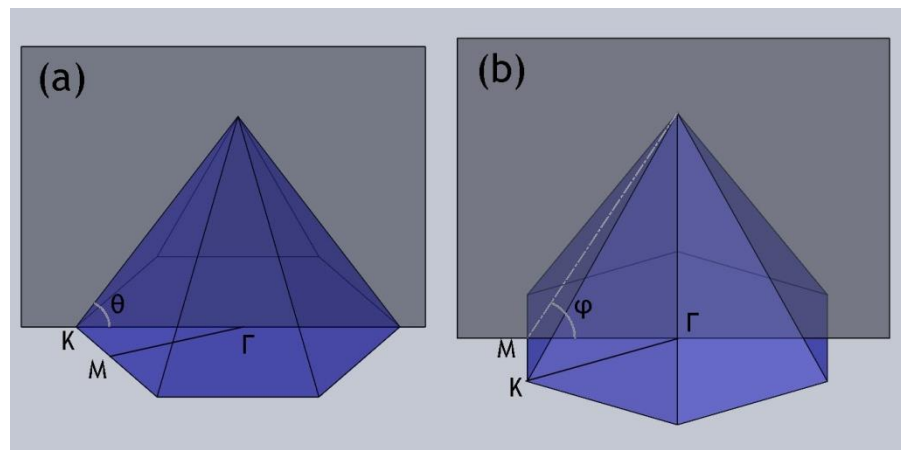


Figure 2.9. Schematic of crystallographic planes of etched hillocks.

2.5 Surface stoichiometry investigation on etched surfaces and investigation of the H₂O₂ smoothening mechanism

In order to better understand the smoothening effect observed in KOH/H₂O₂ etched N-polar AlN and GaN, XPS studies were performed. In general, XPS can be used to determine the chemical state of a surface. Here, the state of the surface is compared for samples etched with KOH and KOH/H₂O₂ solutions. High resolution core level scans for Al 2p, N 1s, and O 1s were performed as these are the main species determining the surface composition of AlN during the etching process.[99] The peak areas were fitted with Voigt peaks and used to determine the surface molar ratios of these species. It should be mentioned that surface roughness can influence the XPS results. Roughness leads to a greater surface area, which may result in a higher total XPS signal count. However, for a particular surface morphology (e.g. hillocks with 60° between pyramid surface and basal plane), the intensity ratio of different elements (Al, N and O in our case) will be constant. Therefore, it is valid to compare the XPS data between KOH-etched N-polar AlN surface and KOH/H₂O₂-etched surface with regards to Al/N, O/N and O/Al molar ratios.

Figure 2.10 shows the molar ratios of Al/N, O/N and O/Al before and after the etching the N-polar AlN surface either in 1 wt% KOH or 1 wt% KOH/10 wt% H₂O₂ solution at 70°C for 15 min. Before etching, an Al/N ratio of 1.1 was found. Assuming a 1:1 stoichiometry between the Al and N in the bulk AlN, the remaining quantity represents extra Al bonded with other species. For Al, an affinity to O is known and formation of an aluminum oxide or hydroxide is expected. KOH etching leads to an increase of the Al/N ratio

to 1.2 and an increase of the O/Al and O/N ratios as well. Adding H₂O₂ into the KOH solution causes a further enhancement of oxide/hydroxide on the etched surface. This suggests stronger oxidation of the surface. The surface energies of the {000̄1} and {10̄1̄1} planes are different due to their different atomic bonding conditions.[100, 101] Following the SEM images presented above, it was concluded that for KOH etched samples the {000̄1} planes were attacked first (fast etching planes) and dominant {10̄1̄1} planes were formed (survival of slow etching planes). H₂O₂ in KOH etchant is expected to act as a strong oxidizer. Thus, there will be fast formation and dissolution of oxides and hydroxides on the surface, resulting in a fast and uniform etching perpendicular to the sample surface. As a result, the etched surface of AlN in H₂O₂/KOH will remain relatively smooth. This explanation is in agreement with the results from SEM presented in Figure 2.6(b), where the small hillocks caused by H₂O₂ tended to be rounded instead of faceted, suggesting a suppression of the {10̄1̄1} planes.

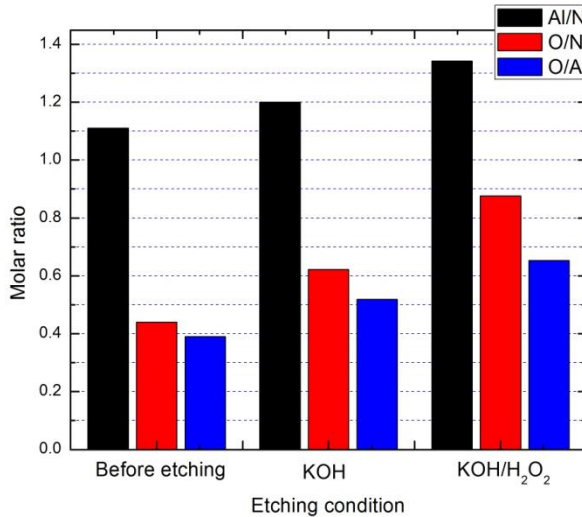


Figure 2.10. Surface molar ratios for N-polar AlN before etching and etched in KOH and KOH/H₂O₂ solutions for 15min.

The specific oxide or hydroxide species on the AlN surface can be identified by their binding energy. In Figure 2.11(a), an O 1s core level peak obtained from a KOH etched AlN bulk crystal and its deconvolution into three components with binding energies of 530.3 eV, 531.7 eV, and 532.8 eV are shown. The three deconvoluted peaks are attributed to O²⁻, OH⁻, and H₂O, respectively.[99, 102] Similar spectra were acquired for KOH/H₂O₂ etching. The molar ratios of O²⁻: OH⁻: H₂O were found to be approximately 1:3:1 and 3:5:2 for the KOH etched and KOH/H₂O₂ etched samples (Figure 2.11(b)), respectively. It was found that the N-polar AlN sample after etching in KOH/H₂O₂ solution had a higher oxide and lower hydroxide level on the surface than the sample etched in KOH.

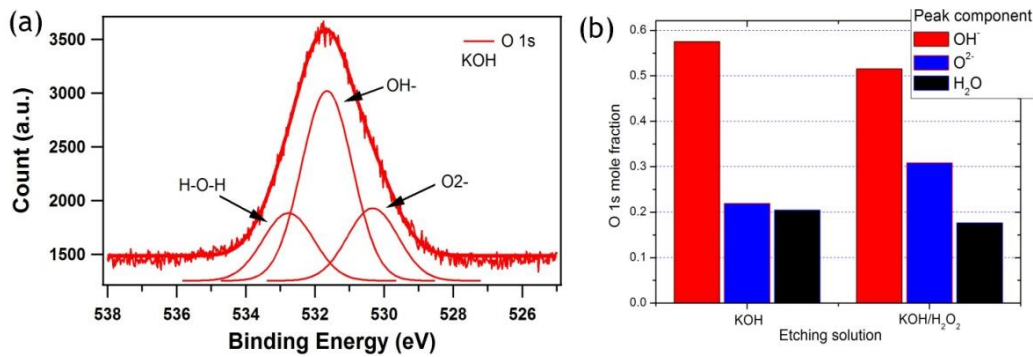


Figure 2.11. Deconvoluted O 1s core level peak of a KOH etched N-polar AlN (a) and the oxygen component distribution (b).

2.6 Etching hillock development and etching mechanism

Etching of III-nitrides in molten NaOH-KOH is considered to be an aggressive method. Reports claim that etching with this etchant is dislocation-related. Typically, it results in the formation of large etching hillocks[101] or pits[88] which can be counted and used for determination of the threading dislocation density.[101] However, as demonstrated above, KOH etching of bulk AlN and GaN results in the formation of hillocks with a density of 10^5 - 10^6 cm⁻² which is far above the dislocation density in these samples and excludes dislocations as origin of the etching mechanism. In order to better understand the etching mechanism, the development of the etching hillocks are further investigated in this section. In addition to AFM and SEM results, TEM was used to confirm the hypothesis that hillock formation is not related to underlying dislocations.

N-polar AlN bulk crystals were etched in 1 wt% KOH or 1 wt% KOH/10 wt% H₂O₂ solution at 70°C for short time periods, below 60 s, and investigated using AFM amplitude

images. As shown in Figure 2.12 the formation of small hillocks with diameter of less than 50 nm starts immediately with the etching process (etching time \sim 15s). As etching time increases, the hillocks become larger and the crystallographic planes become more pronounced (Figure 2.12 (b), etching time \sim 30s). Taking into account the high hillock density and the fact that this density is decreasing as a function of etching time, it is unlikely that these features are related to the threading dislocations of the sample.

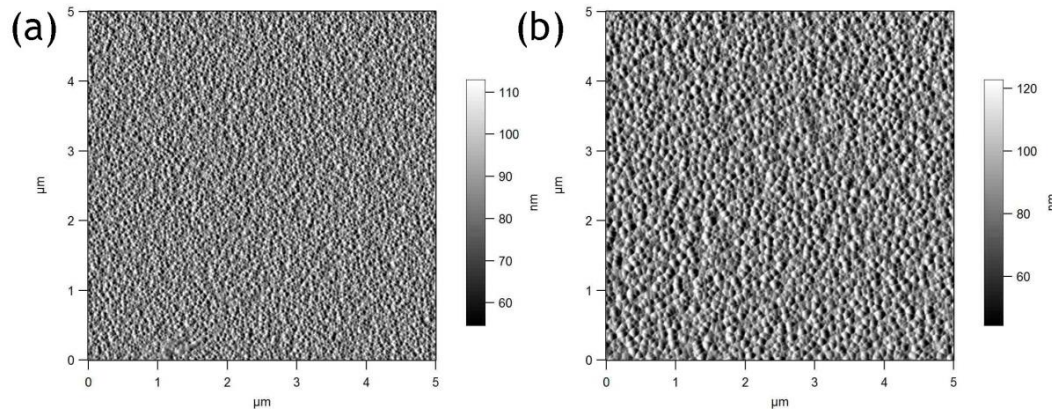


Figure 2.12. Amplitude AFM images of N-polar AlN etched in KOH/H₂O₂ solution for 15s (a) and 30s (b).

Figure 2.13 shows the surface morphology of N-polar AlN after etching in pure KOH aqueous solution for 15s. The observed etching hillocks are much larger than those obtained from etching in KOH/H₂O₂ solution. This result corresponds well with the SEM result shown in Figure 2.6 and the observation of a smoothening effect of the hydrogen peroxide.

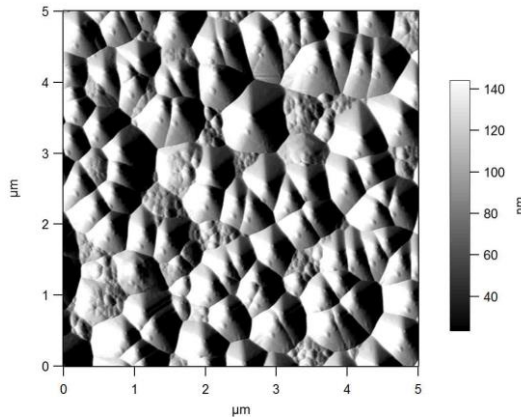


Figure 2.13. Amplitude AFM image of N-polar AlN etched in pure KOH solution for 15s.

Longer etching time of AlN in KOH leads to an increase of the hillock diameter to several micrometers which cannot be effectively imaged by AFM. Therefore, SEM was used instead. Figure 2.14(a) shows an SEM image of the N-polar AlN after 90 min etching in KOH aqueous solution. It is observed that smaller hillocks start to merge together with larger hillocks, leading to the observed increase in hillock diameter. A possible model describing the etching mechanism and hillock formation is depicted in Figure 2.14(b). The blue and yellow lines represent the surface before and after etching, respectively. Blue arrows indicate the direction of the chemical attack. The etching procedure starts with the formation of $\{10\bar{1}\bar{1}\}$ planes. Subsequently, hillocks containing these planes as side facets are uniformly etched and continuously formed and annihilated. The variation of the hillock size is explained as an imbalance of the local etching condition. As indicated by the red arrow in Figure 2.14(b), a low local etch rate variation caused by, for example, chemical diffusion or the existence of dislocations inside the crystal will result in a larger hillock compared to its

neighbors. If this process continues, the smaller neighboring hillocks will merge into the larger, leading to an overall increase of hillock diameter and roughness and decrease of the hillock density.

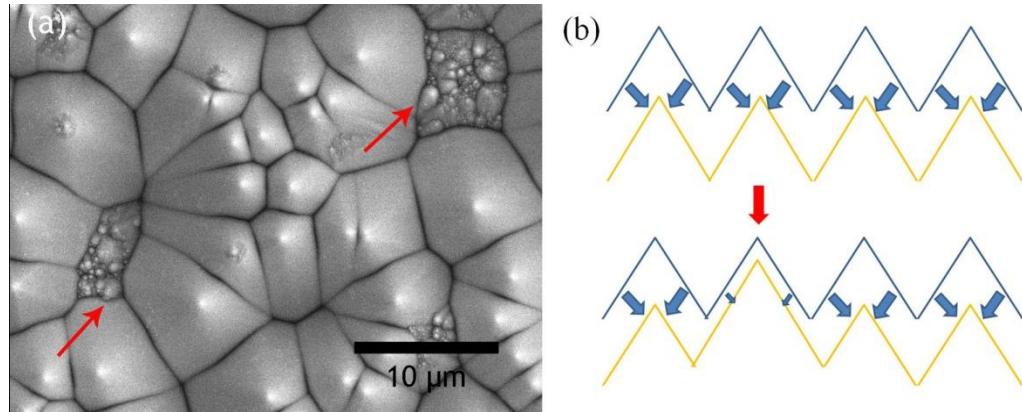


Figure 2.14. Plan view SEM image of N-polar AlN etched in KOH solution (a) and illustration showing the development of etching hillock during etching (b).

The development of etching hillocks is found to be a consequence of the difference of the etch rate of different crystallographic planes. It was clearly shown that it is not related to dislocations in the samples. In order to further prove this finding, cross-sectional TEM was performed on the N-polar AlN and GaN after KOH/H₂O₂ etching at 70°C for 30 minutes. As shown in Figure 2.15 no dislocations were observed beneath the hillocks for either of the two samples (GaN and AlN) and both diffraction conditions (screw and edge dislocation). This is deemed the ultimate proof that the etching hillocks are not related to dislocations. This is

different to molten salt etching where the etching pits/hillocks are used as identifiers of dislocations.

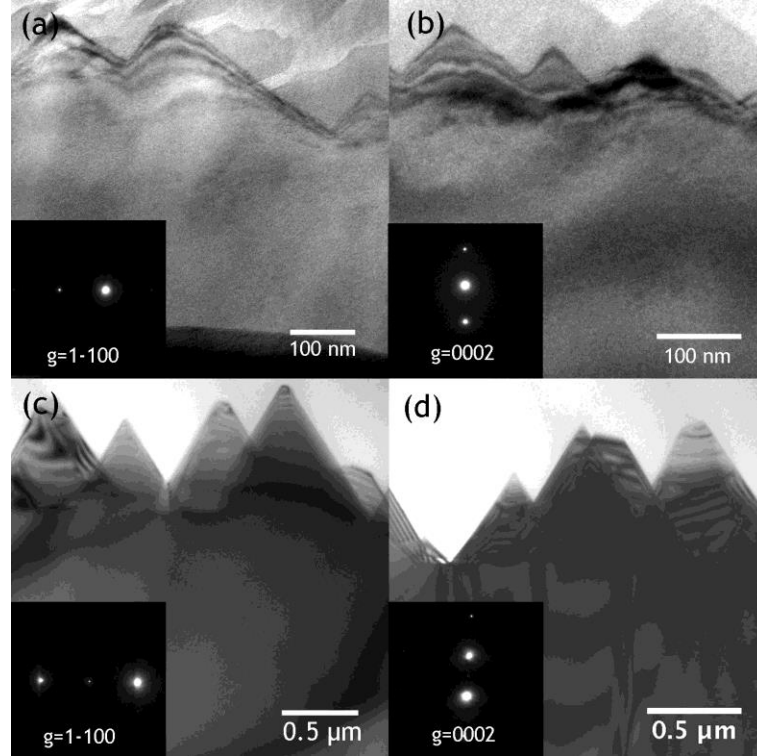


Figure 2.15. Cross-sectional TEM image of AlN (a, b) and GaN (c, d) after KOH etching for 30min. Insets images are electron diffraction patterns with corresponding g vectors. No correlation between hillocks and dislocations is observed.

2.7 Conclusion

In this chapter, the etching behavior of AlN and GaN single crystals as well as AlGaN epitaxial layers in KOH and KOH/H₂O₂ solutions was studied. It was found that the N-polar AlN surface had an etch rate higher than 1 μ m/min while the Al-polar surface had an etch

rate as low as 1.6 nm/min under the same conditions, resulting in a polarity selectivity of about 900 in favor of the N-polar surface. Polarity selectivity was observed also in GaN, with an etch rate that reached about 40 nm/min and 1.9 nm/min for the N-polar and Ga-polar surfaces, respectively. As aluminum composition increases in $\text{Al}_x\text{Ga}_{1-x}\text{N}$ epitaxial layers, an increase of the etch rate was observed.

Further experiments were performed to get a better understanding of the etching mechanism of KOH. Hexagonal hillocks terminated by $\{10\bar{1}\bar{1}\}$ planes are found to start to appear at the early stage of etching. Their diameter is found to increase from less than 50 nm to larger than 5 μm with time. This is explained by the inhomogeneity of the local etch rate. A model was developed and depicted. Adding H_2O_2 into the KOH solution resulted in a higher selectivity and a smoother surface after etching. Based on XPS results, this surface smoothening is attributed to an oxidation effect of the nitride surface, which suppresses $\{10\bar{1}\bar{1}\}$ faceting. Finally, cross-sectional TEM studies confirmed that the KOH etching hillocks are not related to threading dislocations.

It is found that KOH-based aqueous etching can be used as substrate thinning procedure or to remove the AlN substrate used for fabrications of AlGaN-based DUV-LED. This will help to increase light extraction efficiency in DUV-LED.

CHAPTER 3 Surface patterning of III-nitrides

3.1 Surface patterning for light extraction efficiency enhancement in DUV-LEDs

Even though the internal quantum efficiency of AlGaN based multiple quantum wells (MQWs) can reach values of 64%,[103, 104] DUV-LEDs still suffer from low external quantum efficiency (EQE). The reason for this low EQE is that III-nitride-based DUV LEDs have a low extraction efficiency of less than 5% due to high total internal reflection (TIR) caused by the difference of the refractive index at the semiconductor to air interface. Many approaches aiming to increase the light extraction efficiency are discussed throughout literature. This includes surface roughening/patterning techniques, nano-masking RIE, wet etching, electron-beam lithography, and nano-imprint lithography.[47] Among these techniques, e-beam lithography is one of the most investigated methods. Typically, it is used to create sub-micron sized periodic structures on the active region or window layer of the LED[57, 58, 105] structures. Diameters as small as 100 nm and periodicity of 180 nm were demonstrated and a several-fold intensity increase of the emitted light was achieved.[105] However, these techniques are time consuming, limited to small areas, and expensive. New approaches which can overcome these limitations include natural lithography[106, 107] and interference lithography.[108]

In this chapter, results from natural lithography and interference lithography are applied to fabricate nanostructure patterns on III-nitride substrates and AlGaN/AlN MQW structures. The optical properties of processed structures including integral reflection, transmission, and photoluminescence are investigated and compared to as-grown samples.

Different patterning methods, periodicities, sizes, and shape of nanostructures are investigated to determine their influence on the light extraction efficiency and far-field intensity profile. Overall, an enhancement of emission light intensity using a nano-patterning technique is demonstrated. It is found that, since it results in the best periodicity and well-defined structures, interference lithography is the foremost technique. Finally, the influence of periodic structures, including photonic crystals on the AlN transmissivity based DUV-LEDs is investigated using finite-difference-time-domain (FDTD) simulations. Theoretical and experimental results are compared and a good agreement is found.

3.1.1 Natural lithography technique

Recently, self-assembling monolayer masks and anodic aluminum oxide (AAO) fabrication have become commercially available. Based on these new techniques, a novel pattern transfer method called “natural lithography” has drawn an increasing amount of attention. Natural lithography based on a natural colloidal self-assembly phenomenon was first demonstrated by Fischer et al.[109] Nowadays, SiO₂ spheres,[110, 111] polystyrene (PS)[112] spheres, or the self-ordered AAO[113, 114] are used as etching masks for nanostructure pattern transfer. All methods can be used to create large-area patterns at low cost, which is advantageous for industrial applications. However, only very limited results for III-nitrides and specifically for AlN and AlGaN are available. Dai et al.[115], for example, fabricated AAO on n- and p-cladding layers of InGaN-based LEDs. After drying etching, patterns with 160 nm diameter pores were transferred on the LED and a 72% enhancement of the output power was observed. Various groups have used the SiO₂/PS

patterning method for the fabrication of nano-pillar arrays on top of LEDs and demonstrated many-fold increase of EQE and output power.[107, 116-118]

In this work, AAO was fabricated either by two-step anodization of Al foil followed by a transfer process to the LED device,[119] or by direct anodization of an Al thin film on the LED substrate. Subsequently, RIE was applied to transfer the pattern from AAO to the LED.[106, 120] In the case of SiO₂ or PS pattern transfer, SiO₂/PS spheres were coated on top of the LEDs. The sphere underwent a self-assembling into a hexagonal closely packed array which then acted as a hard mask for subsequent dry etching.

3.1.2 Interference lithography technique

As result of this work, it was found that due to the monodispersity of self-assembled nanoparticles the achieved patterns from natural lithography were typically inhomogeneous. This usually led to a loss of periodicity during mask preparation. Thus, a new patterning method, which allowed for periodic structures had to be found. Compared to natural lithography, interference lithography (IL) is found to be applicable for the generation of highly periodic structures and is at the same time very cost-effective and easily scalable.

Interference lithography is also called holography because two coherent laser beams interfere with each other and produce a sinusoidal intensity pattern. If used in combination with a photoresist film on a substrate, highly periodic patterns can be achieved. Both 1D and 2D patterns can be created. The transfer from photoresist to the sample is typically done by RIE. In contrast to conventional photolithography, interference lithography can create sub-micron features below the diffraction limit. In addition, no hard mask is needed during the

process, thus avoiding contamination.[108, 121, 122] Seo[123] and coworkers presented 2D concave hemisphere-shaped pattern on indium-tin-oxide (ITO) layer of GaN-based LEDs with 200 and 400 nm periodicity. For such patterns a 34% enhancement of output power was demonstrated.

3.1.3 Photonic crystals

In addition to increasing the extraction efficiency due to surface roughening, periodically patterned structures can also lead to a highly directional beam profile due to the so called photonic crystal effect.[124] A Photonic Crystal (PhC) is a periodically patterned material in 1D, 2D, or 3D with feature size on the order of the wavelength of interacting light. Distributed Bragg reflectors (DBRs), 2D triangular or square lattice of hole/pillar slabs, and opal represent 1D, 2D, and 3D PhCs, respectively. 2D PhCs are considered to be useful for LEDs as they can enhance light extraction and increase EQE.

Enhancement of light extraction using 2D PhCs can be achieved in two ways. First, if the dimensions of the PhC are tuned to be half of the emission wavelength ($\lambda/2$), a Photonic Bandgap (PBG) is created.[125] In such a system, lateral propagation of light falling within the photonic bandgap is prohibited. Thus, light can only travel perpendicular to the semiconductor-air interface leading to an enhanced extraction efficiency.[126] This condition is called “Strong PhC”. The second way is due to a “Weak PhC” phenomenon. This condition is more common in LEDs. Weak PhCs are generated by periodically arranged slabs of finite thickness. This leads to a periodic change (air/semiconductor) of the refractive index and creates a “cutoff lattice constant”[127] for the structure. Light modes with wavelength λ

become “leaky modes”[128] and can be scattered to free space if the lattice constant of PhC is larger than the cutoff lattice constant Λ_{cutoff} . In other words, the emitted radiation from the dipole source will either couple to the guided modes of the dielectric slab or to radiation modes. For a higher percentage of radiation modes, larger extraction efficiency is achieved. For a weak PhC, no PBG exists and the periodic structure only acts as surface grating. The above mentioned cutoff lattice constant is given by:

$$\Lambda_{cutoff} = \frac{\lambda}{1 + n_{eff}}. \quad (3.1.1)$$

Here, n_{eff} is the effective refractive index of the PhCs region.[129] PhCs possess unique advantages for light extraction applications in LEDs. In the case of random surface roughening, photons will be bounced back and forth until they eventually reach the escape cone or are re-absorbed. In LEDs with PhCs on the surface, a shorter light escape length is provided and parasitic absorption is reduced. In addition, commercial LEDs typically require emission to be collected in a specific solid angle. PhC-patterned LEDs offer better control over the directionality of light emission. Wierer et al.[57] demonstrated that far-field emission pattern of conventional GaN-based blue LEDs is nearly Lambertian whereas the radiation pattern of PhC-patterned LEDs is heavily modified with an increased radiance perpendicular to the interface.[130]

3.2 Natural lithography and interference lithography for III-nitrides

The GaN templates used in this study were grown in a vertical, cold-walled, RF-heated, low-pressure MOCVD reactor.[131] Triethylgallium (TEG) and ammonia were used as Ga and N precursors, respectively and N₂ was used as diluent gas. Growth temperature was controlled at 1040°C and the V/III ratio was fixed at 100. 1.3 μm thick GaN was grown on c-sapphire substrate. 600 nm AlN was grown on c-sapphire substrates at growth temperatures around 1200-1250°C and V/III ratios of 1500-2000. The AlGaN/AlN MQW structures on single crystal AlN substrates were also grown by MOCVD with structures consisting of 500 nm Al_{0.7}Ga_{0.3}N and 10 pairs of Al_{0.5}Ga_{0.5}N/AlN (1.6 nm well/4 nm barrier).

Natural lithography was used to fabricate both nano-porous and nano-pillar structures on III-nitride and MQW structures. III-nitride nano-porous structures were achieved via AAO surface patterning. A schematic of the fabrication process is shown in Figure 3.1 (a). First, the samples were ultrasonically cleaned sequentially in acetone, methanol, and deionized water for 5 min each. Then a 200 nm Al/10 nm Ti metal stack was deposited on the sample by e-beam evaporation. The sample was immersed into 0.3 M oxalic acid solution in water and a two-step anodization was performed.[132, 133] The first step aimed to create small dimples with Al₂O₃ porous structures in the Al thin film. An electrical potential of 40 V was applied during the first anodization process for 5 min, followed by wet etching under 0.2 M/0.4 M chromic acid/phosphoric acid mixture at 60°C. The etching was applied in order to partially remove the porous aluminum. The second anodization process led to the oxidation of Al and arrangement into highly organized Al₂O₃. The second anodization was

performed under the same condition as the first step. Subsequently, etching with 5 wt% H₃PO₄ at room temperature was performed in order to widen the AAO pores. The nano-porous structures generated by AAO were then transferred to the underlying GaN or AlN by reactive ion etching using a TRION Minilock system with a Cl₂/BCl₃ plasma with flow rates of 25/25 sccm. The pressure was set as 70 mTorr and the RIE power was 100 W. Different etching times, ranging from 4 min to 15 min were applied to investigate the influence of etching time on pore morphology.

In order to compare the nano-porous structures generated by AAO with its complementary nano-pillar structures, surface patterning using SiO₂ spheres was also performed. A schematic of the process flow for patterning via SiO₂ spheres is shown in Figure 3.1 (b). First, the GaN or AlGaN/AlN MQW substrates were cleaned as described above. The cleaning was followed by immersion in 1:1 H₂O₂/H₂SO₄ solution to make the surface hydrophilic. Suspension with 100 nm and 200 nm diameter SiO₂ spheres in water solution (Nissan Chemical) was spin-coated on the substrates to form a closely-packed monolayer. RIE with CF₄ 50 sccm plasma was used to reduce the dimensions of the SiO₂ spheres followed by Cl₂/BCl₃ plasma to achieve nano-pillar structures. After pattern transfer via RIE, AAO and SiO₂ monolayer masks were removed in HF/water solution followed by sonication in acetone/methanol/DI water for 5 min each.

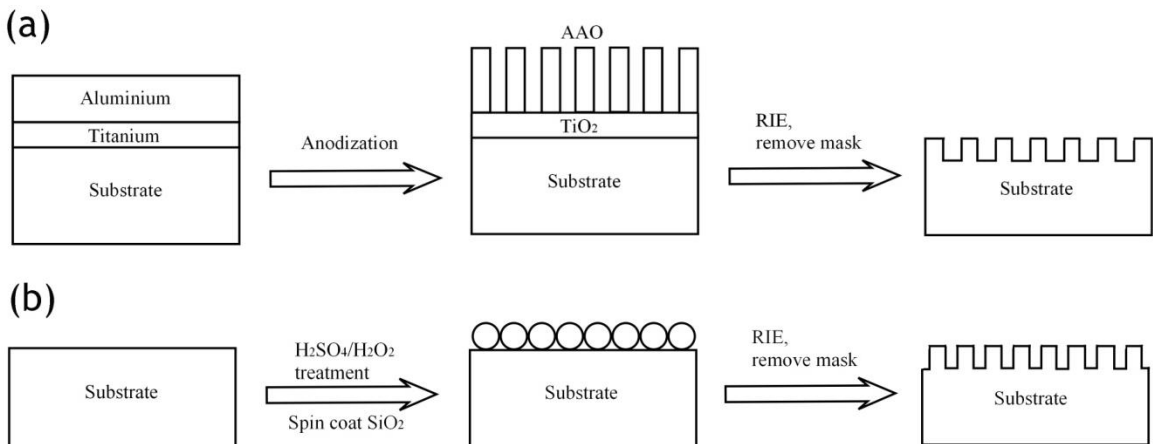


Figure 3.1. Schematic process flow of natural lithography patterning on GaN or AlN.

The nano-porous and nano-pillar structures fabricated via AAO and SiO₂ spheres were found not to have long-range periodicity due to the nature of mask preparation (purely random arrangement of the nanostructures). Therefore, interference lithography was done, using a Lloyd's Mirror interferometer setup as shown in Figure 3.2, to achieve periodic structures.

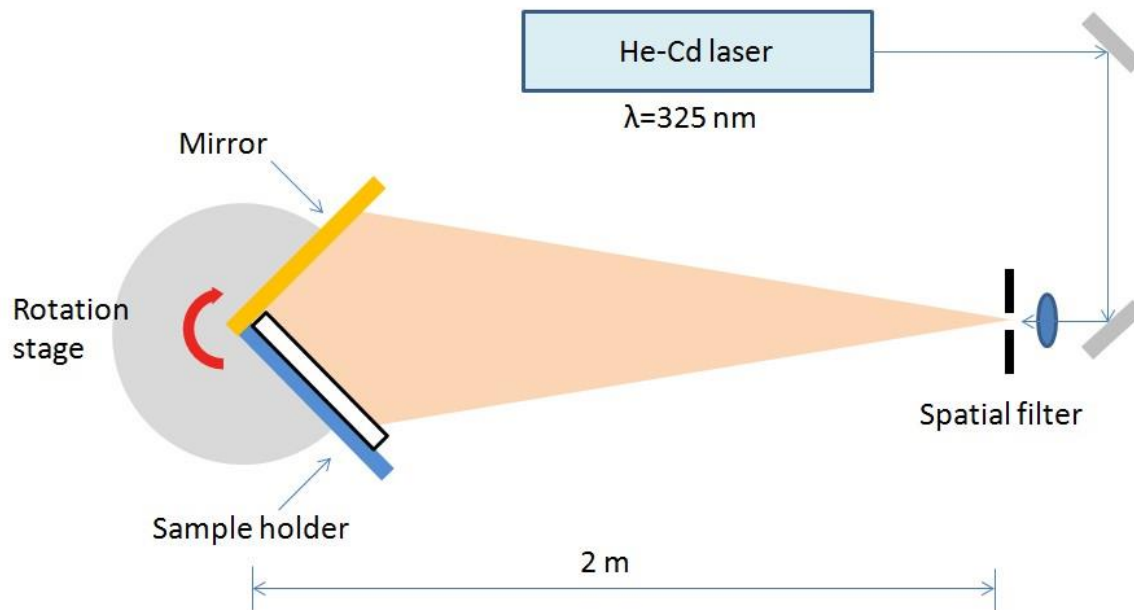


Figure 3.2. Lloyd's Mirror interferometer setup used for interference lithography.

For a Lloyd's Mirror interferometer, the mirror is perpendicular to the sample holder. The light reflected from the mirror interferes either constructively or destructively with the light shedding directly on the sample. This interference leads to a periodic intensity pattern on the sample coated with photoresist. The rotary stage shown in Figure 3.2 allows to change the angle at which light is incident on the sample, thereby changing the periodicity under which the sample is patterned:

$$\Lambda = \frac{\lambda}{2n \sin \theta} \quad (3.2.1)$$

Here, Λ is the periodicity of the pattern, λ is the wavelength of the laser, n is the refractive index of the medium (typically air), and θ is the incident angle. The used setup utilizes a He-Cd laser with 325 nm emission wavelength as the light source. Initially, the light passes through a spatial filter, which provides a clean Gaussian beam by removing interference from dust particles. The sample which is covered with photoresist (PR) is attached to the sample holder and will encounter an approximately plane-wave front after the beam reaches out for 2 meters. A 1D pattern can be achieved by a one time exposure, while 2D patterns can be achieved by two subsequent exposures with the sample placed in two perpendicular directions. However, due to the limit of the beam size, the effective area of interference lithography was restricted by the setup. Furthermore, the pattern shape was only limited to 1D or 2D periodic feature in comparison to standard photolithography.

A schematic of the process flow for interference lithography including the etching and cleaning steps is shown in Figure 3.3. An Anti-Reflection-Coating (ARC) was used to reduce the light reflection from the interface between the photoresist and sample, which could disturb the exposure of the photoresist. The thickness of the ARC needed to be optimized for each periodicity in order to achieve an optimal anti-reflection effect. A *MatLab* program was used to estimate the individual thickness of the ARC.[134]

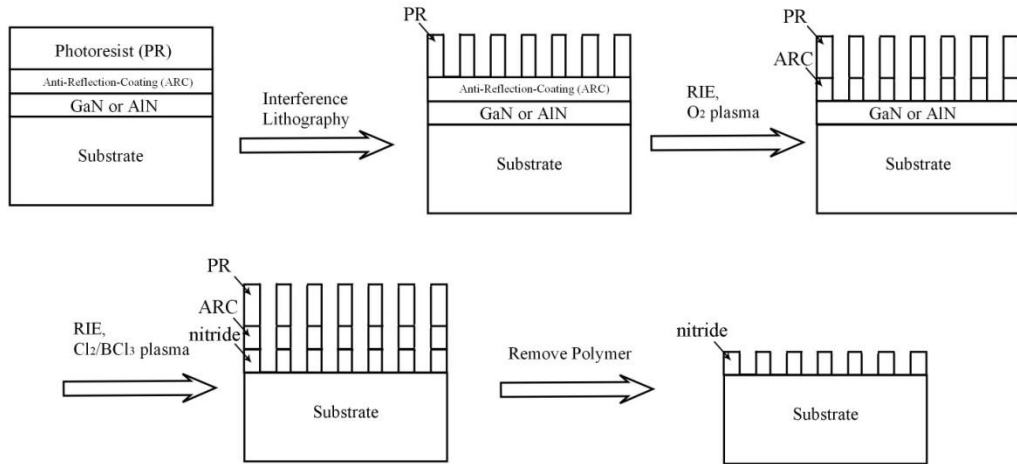


Figure 3.3 Schematic process flow of the interference lithography patterning.

The surface morphology of the patterned GaN and AlN thin films and AlGaN/AlN MQW structures was characterized by a JEOL JSM-6400 field emission scanning electron microscope (FE-SEM) operating at 5 kV. Integral transmission/reflection of as-grown and patterned structures was determined using a 2-inch integrating sphere from Thorlabs, which was connected to a Princeton Instruments Acton SP2750 0.75 m high-resolution monochromator with a 150 grooves/mm grating and attached CCD via an optical fiber. A schematic of the setups for integral reflectivity measurements and angle-resolved transmission measurements are shown in Figure 3.4.

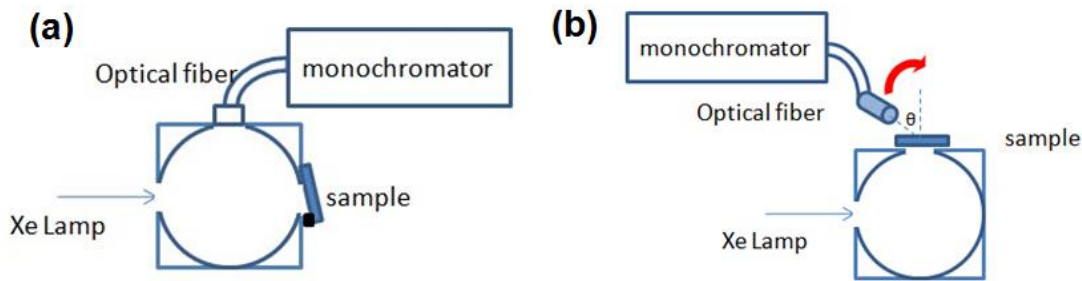


Figure 3.4. Schematic showing the setups for (a) integral reflectivity measurements and (b) angle-resolved transmission measurements.

As shown in Figure 3.4, collimated light from a Xe gas-discharge lamp is coupled into the integrating sphere through its entrance port. For integral reflection measurements, samples were attached opposite to the entrance port of the integrating sphere such that the light source was incident at 8° to the surface normal (to reduce total reflection back to the entrance port). The value of the integral reflectivity R can be calculated by

$$R = \frac{I_s}{I_r}, \quad (3.2.2)$$

where I_s is the intensity of the reflected light with the sample in the integrating sphere and I_r is the intensity of reflected light from a highly-reflective material (the cap of the integrating sphere).

Angle-resolved transmission measurements with collection angle ranging from -45° to 45° at a 2° resolution were conducted by putting the sample at the exit port of the

integrating sphere using an optical fiber attached to a rotation stage. Transmission T is then calculated using

$$T = \frac{I_s}{I_b} \quad (3.2.3)$$

where I_s denotes the intensity when the sample was attached to the integrating sphere, and I_b represents the intensity when no sample was placed on the port.

Photoluminescence (PL) spectra of the patterned and planar AlGaN/AlN MQW structures were recorded using an ArF laser emitting at 193 nm incident on the sample surface at 45°. The luminescence signal was collected at 0°, 15°, 30° and 45° normal to the sample surface and recorded using the Princeton Instruments Acton SP2750 0.75m high-resolution monochromator with attached CCD. Finally, a simulation of the far-field intensity profile was performed using the “Lumerical” FDTD solution package.

3.3 Surface morphology of patterned III-nitride surfaces

3.3.1 Nano-porous and nano-pillar GaN fabricated by natural lithography

The surface morphology of AAO on GaN films was analyzed in order to understand the influence of process parameters on size and structure of the nano-porous pattern. Figure 3.5 (a) and (b) show plan-view SEM images of AAO on top of GaN/sapphire processed with 6 min and 9 min anodization time, respectively. Increasing the anodization time by three minutes leads to an increase of the pore diameter from ~20 nm to ~65 nm. While shorter anodization time leads to compact films without visible pores, it is found that

anodization times longer than 9 minutes leads to degradation of the AAO. Consequently, 9 min anodization time is deemed to be optimal for pattern transfer.

The diameter of the pores and size distribution is crucial for the optical properties of the patterned surface. A histogram of the size distribution is shown in Figure 3.6. The average diameter is found to be around 65 nm. The average inter-pore distance was estimated to be around 100 nm, indicating a well-pronounced separation of the individual pores. However, no long-range periodicity is seen and some of the pores were connected to each other. This non-uniformity arose primarily for two reasons: (1) the 200 nm Al film on GaN was too thin to form highly ordered AAO cell structure, and (2) the insulating GaN/sapphire substrate beneath the Al film influenced the current flow during anodization, which led to the inhomogeneity of the AAO cell size.[135, 136] Figure 3.5 (c) shows the cross-sectional view of the AAO on top of GaN after 9 min anodization time. Straight inner-walls, which are desirable for the RIE pattern transfer, can be observed.

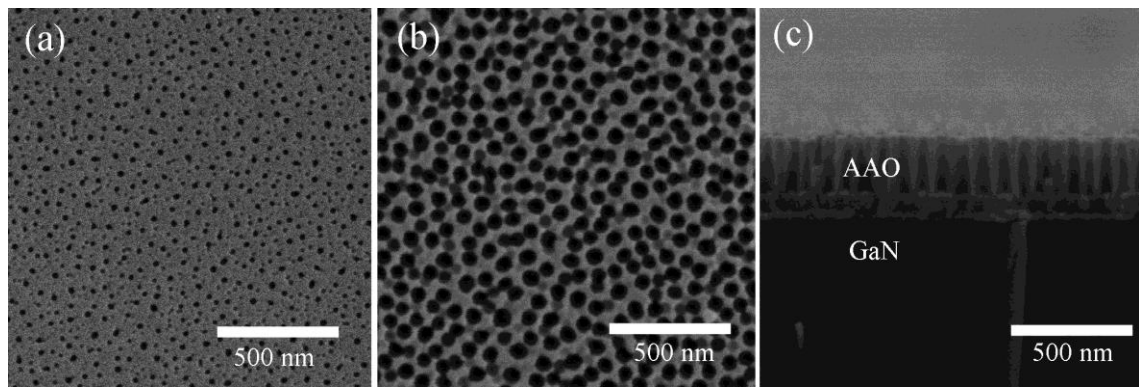


Figure 3.5. FE-SEM images of AAO on GaN fabricated by the two-step anodization method: (a) 6 min anodization, plan-view, (b) 9 min anodization, plan-view, (c) 9 min anodization, cross-sectional view.

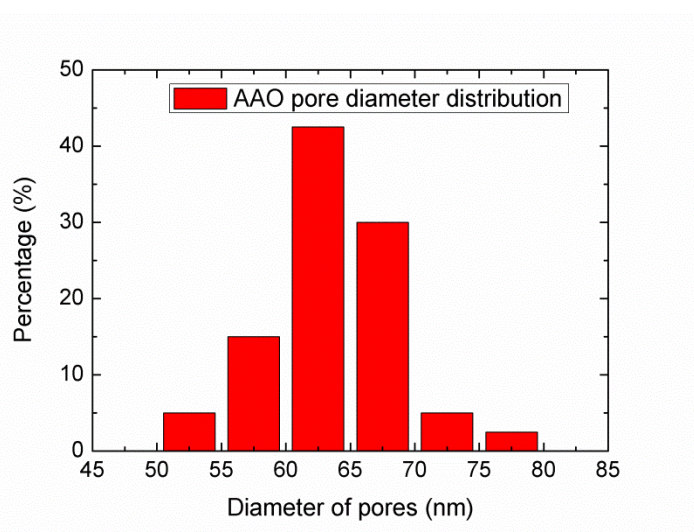


Figure 3.6. AAO pore diameter distribution histogram binned in 5 nm increments for AAO with optimal anodization condition.

Using the optimized AAO mask on the GaN film, different etching times were applied to transfer the pattern from AAO to GaN. Figure 3.7 shows the surface structure of etched GaN layers recorded with SEM as a function of the Cl_2/BCl_3 plasma etching time. It is evident that the pore diameter and pore depth increase with etching time. The optimal etching time was established to be around 7 minutes with resulting pore diameters around 50 ± 15 nm, whereas the inter-pore distance of 100 nm remained the same as for the original AAO mask. The pore density was estimated to be $7.8\times 10^9 \text{ cm}^{-2}$ and $1.2\times 10^{10} \text{ cm}^{-2}$ for 4 min and 7 min etching, respectively. The pore density for 7 min etching was similar to the density of holes in the AAO mask shown in Figure 3.5 (b), demonstrating a complete pattern transfer. Finally, Figure 3.7 (c) shows that a further increase of the etching time to 15 min led to a decrease in the quality of the nano-porous structure due to pore coalescence.

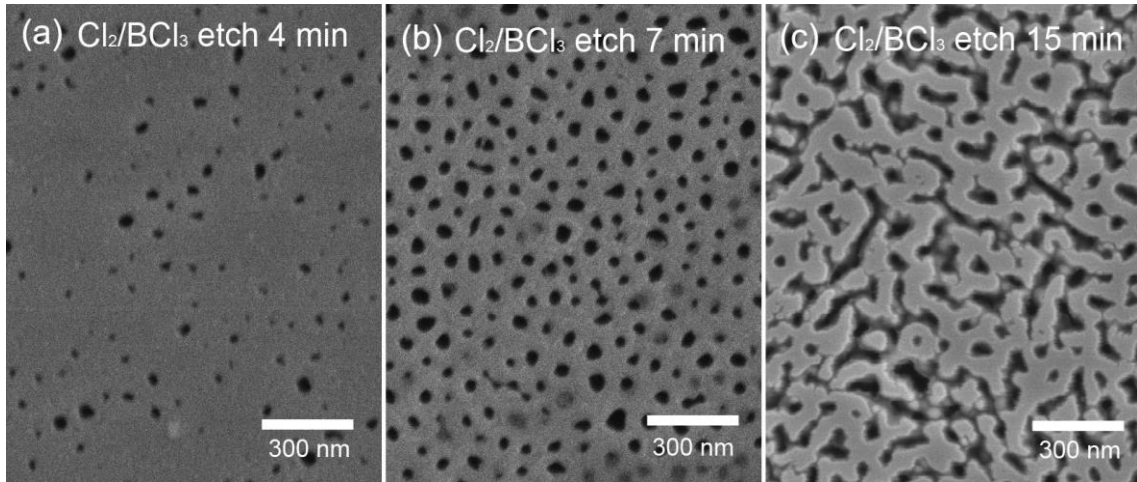


Figure 3.7. Plan-view FE-SEM images of GaN nano-porous arrays after etching in Cl_2/BCl_3 25 sccm/25 sccm for (a) 4 min, (b) 7 min, (c) 15min.

Nano-pillar structures were fabricated on both GaN and AlGaN/AlN MQW samples. As shown in the process flow in Figure 3.1 (b), a monolayer of SiO_2 spheres was used as a mask. In order to achieve a SiO_2 monolayer, the sample surface treatment condition, spinning condition, and SiO_2 solution concentration, which are all critical factors of the process, needed to be well understood. It was found that if the GaN or AlGaN/AlN MQW structures were not treated with $\text{H}_2\text{SO}_4/\text{H}_2\text{O}_2$ acid to increase hydrophilicity, SiO_2 sphere coverage was low and patches of SiO_2 blobs were seen on the surface. Optimal spin speed for the coating was found to be 7000 rpm in combination with 4000 rpm/s ramping speed. This ramping condition ensures a uniform spin coating over the whole 2 inch wafer. The concentration of SiO_2 aqueous solution is crucial for the surface coverage and formation of the monolayer. Thus, different concentrations of SiO_2 aqueous solution were tried and their influence on monodispersity was investigated. Figure 3.8 shows plan view SEM images of 100 nm

diameter SiO_2 spheres coated on a GaN surface. Suspension concentrations ranging from 2 wt% up to 10 wt% were applied. 2 wt% SiO_2 solution led to less than 50% coverage of the surface (assuming a 100% coverage of the surface when SiO_2 was closely packed), while 10 wt% SiO_2 solution resulted in more than one layer of SiO_2 spheres. Consequently, 6 wt% is found to be the optimal concentration. For this concentration a packing efficiency of ~80% can be achieved. It should be mentioned that the as-received SiO_2 nanoparticle had a large range of size distribution (75 nm to 112 nm), and that this poor monodispersity is believed to be the main reason for the loss of periodicity during monolayer coating.

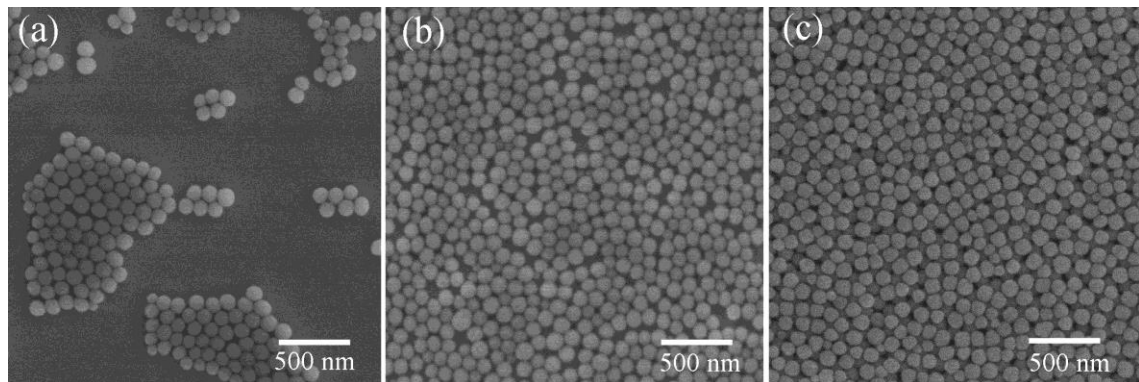


Figure 3.8. Plan-view SEM images of SiO_2 particle (100 nm diameter) spin coated on a GaN surface: (a) 2 wt% SiO_2 concentration; (b) 6 wt% SiO_2 concentration; (c) 10 wt% SiO_2 concentration.

Following the formation of the SiO_2 monolayer mask, GaN nano-pillar structures were fabricated using RIE. Figure 3.9 (a) and (b) show a plan-view FE-SEM image of a SiO_2 monolayer (100 nm diameter) on GaN, and GaN nano-pillars after 2 min of Cl_2/BCl_3 etching, respectively. Interconnected pillars can be seen. The diameter at the top of the pillars was

100 ± 15 nm, which is similar to the average SiO_2 sphere size. The average inter-pillar distance was estimated to be 130 ± 20 nm.

The interconnectivity of the pillars is expected to be negative for the possible enhancement of the light extraction. So far, only for free-standing dielectric pillar structures that introduce a gradual change of the effective refractive index in the patterned region has been found to have a positive effect either experimentally or theoretically.[137, 138] In order to completely separate the nano-pillars, the size of the spin-coated SiO_2 spheres was reduced to 80 nm via CF_4 plasma etching under the RIE/ICP power of 100W/100W. As shown in Figure 3.9 (c), there was no obvious sign of aggregation of adjacent SiO_2 spheres in the monolayer mask or disruption of the ordering after the reduction of the sphere size. Figure 3.9 (d) shows the morphology of the nano-pillar structure after subsequent pattern transfer. Compared to Figure 3.9 (b) the gap between the pillars was increased and the pillars were mostly free-standing.

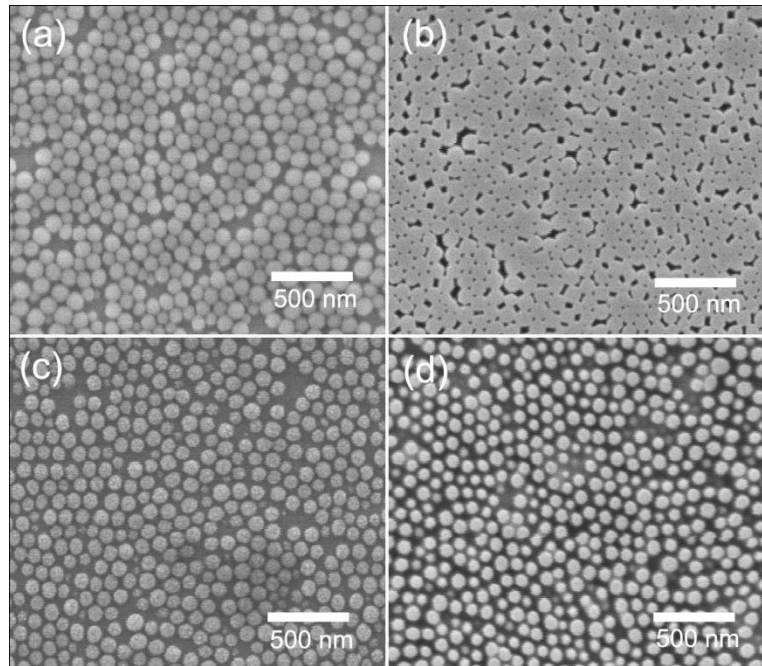


Figure 3.9. Plan view FE-SEM images of (a) a 100 nm SiO_2 sphere monolayer on GaN; (b) GaN nano-pillars after transfer; (c) SiO_2 sphere monolayer after sphere diameter was reduced; (d) GaN nano-pillars obtained after reducing the sphere size.

The height of the nano-pillar structures generated by SiO_2 spheres can be controlled by changing the RIE time. Figure 3.10 shows 60° tilted FE-SEM images of the GaN pillars after different etching times. Nano-pillars generated from spheres without (a, c) and with (b, d) ICP CF_4 shrinking are compared. It can be seen that without the reduction of the SiO_2 sphere diameter, the GaN nano-pillars remained interconnected. On the other hand, isotropic etching in CF_4 as short as 1 min reduced the sphere size sufficiently to increase the gap between pillars and generate free-standing structures. The height of free-standing GaN nano-pillars was 110 ± 20 nm and 180 ± 10 nm for 2 min and 4 min Cl_2/BCl_3 etching, respectively.

Taking into account data from 1 min and 6 min etching (not shown), a linear etch rate of approximately 50nm/min is estimated.

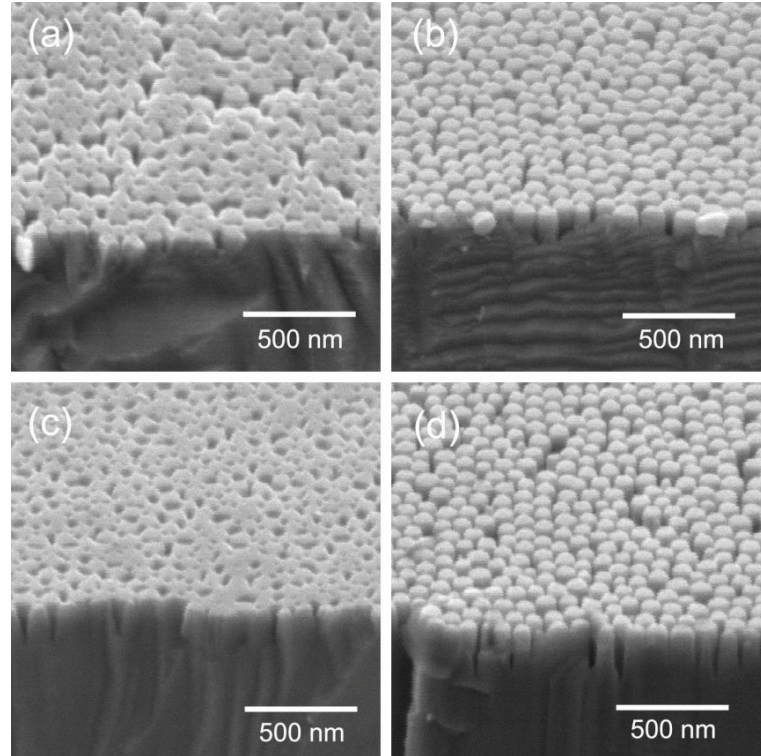


Figure 3.10. Tilted (60°) FE-SEM images of GaN nano-pillars obtained at different conditions: (a) as deposited spheres and 2 min Cl_2/BCl_3 etching; (b) 1 min CF_4 etching to reduce the sphere size, followed by 2 min Cl_2/BCl_3 etching; (c) as deposited spheres and, 4 min etching; (d) 1 min CF_4 etching to reduce the sphere size, followed by 4 min Cl_2/BCl_3 etching.

As shown in Figure 3.9, the inter-pillar distance can be controlled by the size of the SiO_2 spheres. So far, the morphology of GaN nano-pillar structures fabricated by 100 nm diameter SiO_2 spheres and the influence of shrinking was investigated. Similar spin-coating and RIE conditions were also applied to SiO_2 spheres with 200 nm diameter. Figure 3.11 (a)

and (b) show plan-view FE-SEM images of a monolayer formed by 200 nm diameter SiO₂ spheres on GaN. Using a 20 wt% SiO₂ solution led to the highest surface coverage and most uniform particle distribution across the wafer. Comparing Figures 3.9 and 3.11, it is found that the 200 nm diameter SiO₂ monolayer showed a slightly better local periodicity than the monolayer formed by 100 nm diameter SiO₂ spheres. This is probably due to an improved size distribution as the sphere diameter becomes larger. Pattern transfer was applied from the SiO₂ monolayer to the GaN thin film and a SEM image of the resulting nano-pillar structure is shown in Figure 3.11 (c). The nano-pillars are found to be uniform in diameter and closely packed after they were fabricated utilizing 1 min CF₄ plasma shrinking followed by 4 min Cl₂/BCl₃ etching.

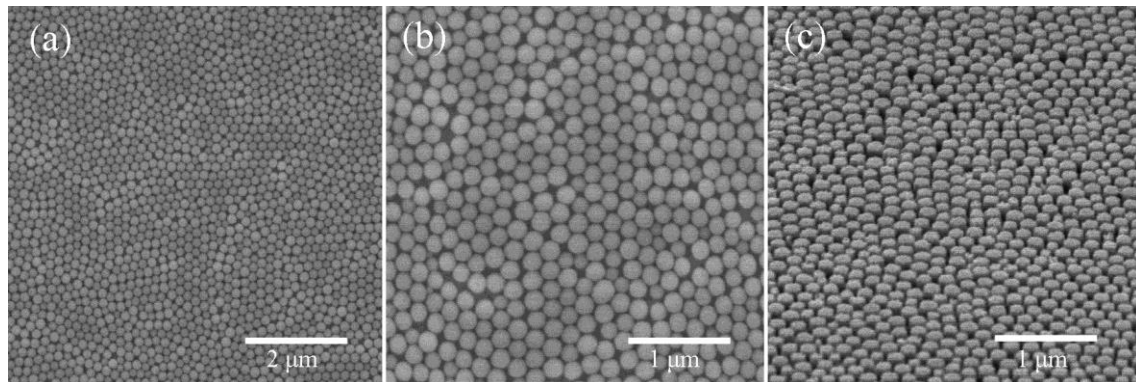


Figure 3.11. (a,b) FE-SEM images of a monolayer of 200 nm diameter SiO₂ spheres on GaN and (c) 80° tilted view of GaN nano-pillars after RIE and plasma shrinking.

In summary, nano-porous structures and nano-pillar structures were fabricated via natural lithography techniques. It was demonstrated that the pore size or pillar diameter can

be controlled by AAO anodization condition and SiO₂ particle shrinking, respectively. In addition, inter-pore and inter-pillar distance can be controlled by changing anodization electrolyte and SiO₂ particle size, respectively. Furthermore, the depth of the pores or height of the pillars can be controlled by applying different RIE etching times. Consequently, natural lithography is found to be highly controllable in a mass-production setting, and cost-effective compared to other nanostructure fabrication techniques and deemed to be useful for LED applications. However, despite these advantages, patterns achieved by natural lithography offered only low short-range periodicity, which excluded them from the application for photonic crystals. Thus, a new technique, which offered the same advantages as natural lithography in combination with long-range periodicity was developed.

3.3.2 1D and 2D III-nitride periodic arrays fabricated by interference lithography

Interference lithography generates patterns using interference of laser light. These interference patterns are typically highly periodic and that interference lithography is expected to be a promising technique for inexpensive, highly periodic structures in mass production. However, only very limited results on interference lithography applied to III-nitrides are available in literature.[108, 139, 140]

SEM images of photo-resist (PR) on GaN patterned using the interference lithography technique, as illustrated in Figure 3.3, is shown in Figure 3.12. A 1D (a) and 2D (b) pattern is shown. The periodicity was 200 nm for both patterns. A sharp contrast of the developed and un-developed PR was achieved by controlling the exposure dose and developing time.

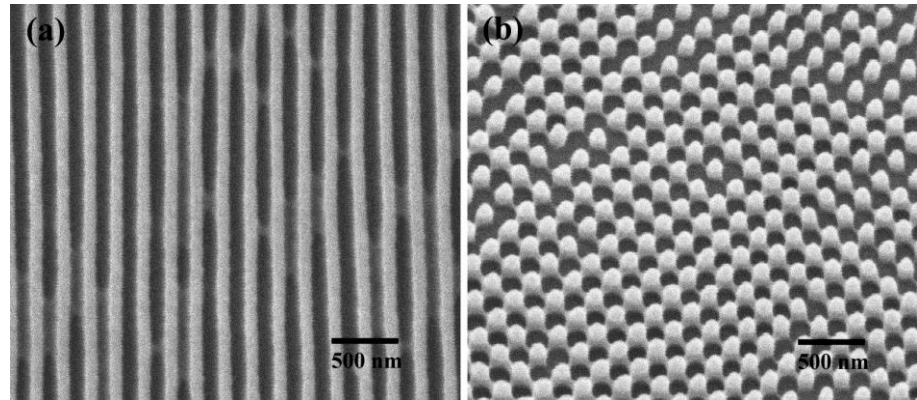


Figure 3.12. 1D (a) and 2D (b) PR patterning on GaN generated by interference lithography.

Subsequently, the periodic structures were transferred from PR to the GaN substrate using RIE. Figure 3.13 shows the 1D and 2D GaN arrays. The periodicity of the GaN patterns is found to be 200 nm, which followed the periodicity of the patterned PR and demonstrated successful 1:1 pattern transfer. Throughout literature, this is the smallest periodicity achieved on GaN and AlN thin films so far using interference lithography. Fabrication of the nano-walls and nano-pillars on areas as large as 1 inch was demonstrated. The wafer size was limited solely by the setup and up-scaling can be achieved by using an advanced interference lithography system. Periodic nanostructures with the achieved feature size are able to interact with light on the wavelength scale, thus allowing for better light propagation management, including light extraction efficiency enhancement in DUV-LEDs.

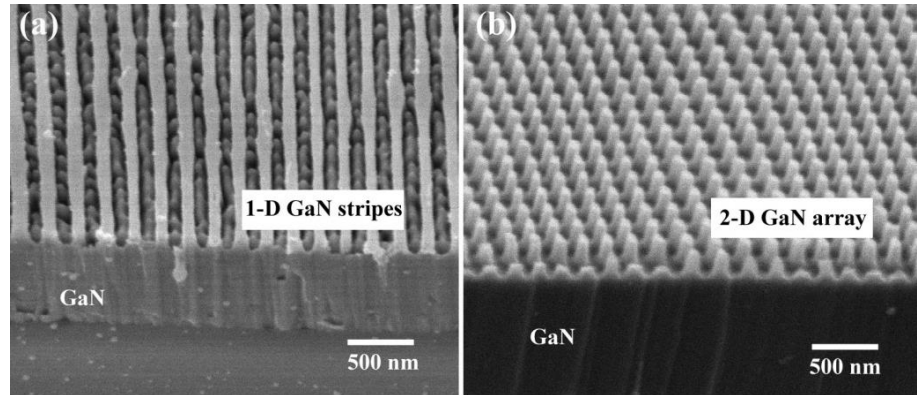


Figure 3.13. 1D (a) and 2D (b) GaN patterning achieved by interference lithography after pattern transfer from PR.

Eventually patterning of AlN was investigated. Patterning of AlN on sapphire followed the same process as for the GaN samples. Structures with periodicity ranging from 400 to 600 nm were fabricated. SEM images of the patterned AlN surface are shown in Figure 3.14. Similar to the natural lithography, the shape and height of the pillars, and the inter-pillar distance can be controlled by the RIE process conditions. This provides various opportunities to optimize the pattern with regards to enhanced light extraction efficiency in nano-patterned LED. In the next section, optical properties including integral reflection/transmission and photoluminescence spectroscopy of nano-patterned structures are investigated and the influence of the nanostructure periodicity on light extraction efficiency is studied.

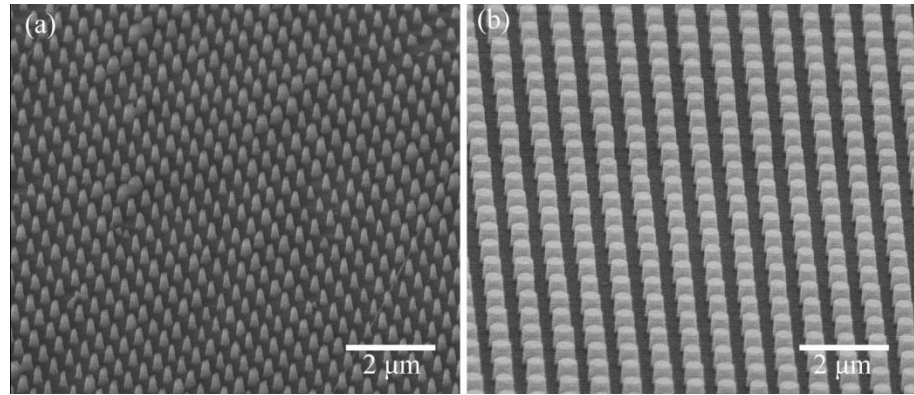


Figure 3.14. SEM images of 2D AlN arrays with periodicity of (a) 400 nm and (b) 600 nm.

3.4 Optical properties of patterned III-nitrides

3.4.1 Integral reflectivity of nano-patterned structures

In order to investigate the influence of the patterning technique on the optical properties, the integral reflection was measured. Figure 3.15 shows reflectivity of planar (as grown) GaN, inter-connected and free-standing pillars fabricated by the natural lithography, and 2D arrays fabricated using the interference lithography. It can be seen that the reflectivity of the as grown GaN sample is the highest of all structures. The periodic oscillation of the reflectivity with wavelength corresponds to thickness fringes of the GaN film. Calculated thickness from these fringes is approximately 1.2 μm, which is in agreement with cross-sectional SEM data. A reduced reflectivity is observed for all patterned samples. The anti-reflective effect of the patterned surface is further visible through the reduction of the thickness fringes. An increased separation of the thickness fringes for the nano-pillar patterned structures is observed. This corresponds to a decreased effective thickness of the

GaN layer due to material loss from RIE. Comparing the interconnected and free-standing GaN nano-pillars, a lower integral reflectivity over the whole investigated wavelength range can be observed for the latter. However, among all investigated structures, periodic GaN nano-pillars fabricated by interference lithography showed the lowest reflectivity and only minor thickness fringes. These observations underline the importance of the periodicity for anti-reflection coatings in III-nitrides.

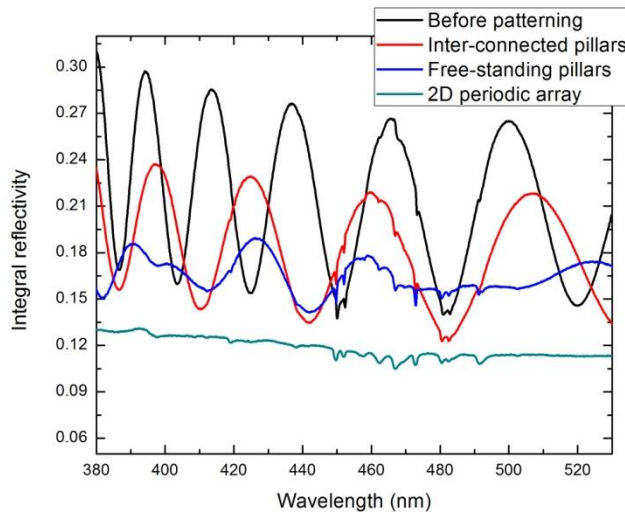


Figure 3.15. Measured integral reflectivity of planar GaN and GaN with nano-pillars of different shapes on the surface.

The interference fringes in Figure 3.15 hinder a direct comparison of the reflectivity values of the samples. In order to obtain comparable values for the integral reflectivity, the curves were fitted based on the light interference equation:

$$R = 2\sqrt{R_1 R_2} \cos \delta , \quad (3.4.1)$$

where R represents the measured reflectivity from the interference effect, R_1 and R_2 represents the reflection of the original coherent light coming from the front and back interface, and δ denotes the phase shift given by:

$$\delta = \frac{4\pi n}{\lambda} d \cos \theta \pm \pi . \quad (3.4.2)$$

Here, n is the refractive index of the material,[44] d is thickness of the film (1.3 μm), λ denotes the wavelength, and θ represents the angle of refraction (8°). The fitting of the data from Figure 3.15 using Equation (3.3) is shown in Figure 3.16 (a).

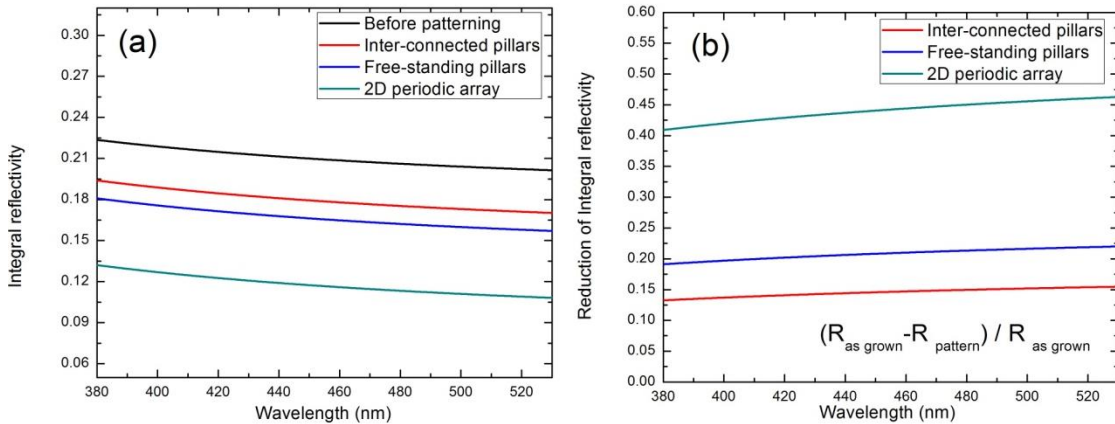


Figure 3.16. (a) Fitted integral reflectivity of patterned GaN and (b) calculated reduction of the integral reflectivity after nano-patterning.

Ideally, a patterned film would reduce reflectivity in order to allow for a better out-coupling of light. Figure 3.16 (b) shows the effective reduction of the reflectivity as a function of wavelength for the investigated patterns normalized to the as grown planar GaN. Here, the reduction of the reflectivity was calculated using

$$\frac{R_{\text{as grown}} - R_{\text{pattern}}}{R_{\text{as grown}}} . \quad (3.4.3)$$

An up to 22% decrease of the reflection due nano-patterning using natural lithography is observed. Furthermore, a 45% decrease of light reflection was achieved for samples with the highly periodic nano-patterning using the interference lithography. Since the light propagation is symmetric in both directions, the reduced reflectivity corresponds to significantly higher light extraction efficiency. If absorption was neglected in the substrate, a 45% decrease of light reflection (from 22% to 12%) of nano-patterned structures using interference lithography results in a 13% increase of transmission (from 78% to 88%). This result shows the potential of using nano-pillar patterned structures for DUV-LEDs. In addition, the result also agrees well with theoretical predictions[141] claiming that periodic nano-structures outperform random roughened nanostructures in enhancing the light extraction efficiency.

3.4.2 Angle-resolved transmission of nano-patterned structures

In order to further support the conclusions made from integral reflection measurements, angle-resolved transmission measurements were conducted on planar GaN and 2D periodic GaN structures fabricated by interference lithography. Transmission was recorded depending on wavelength and collection angle and a pseudo-3D image as shown in Figure 3.17 was generated.

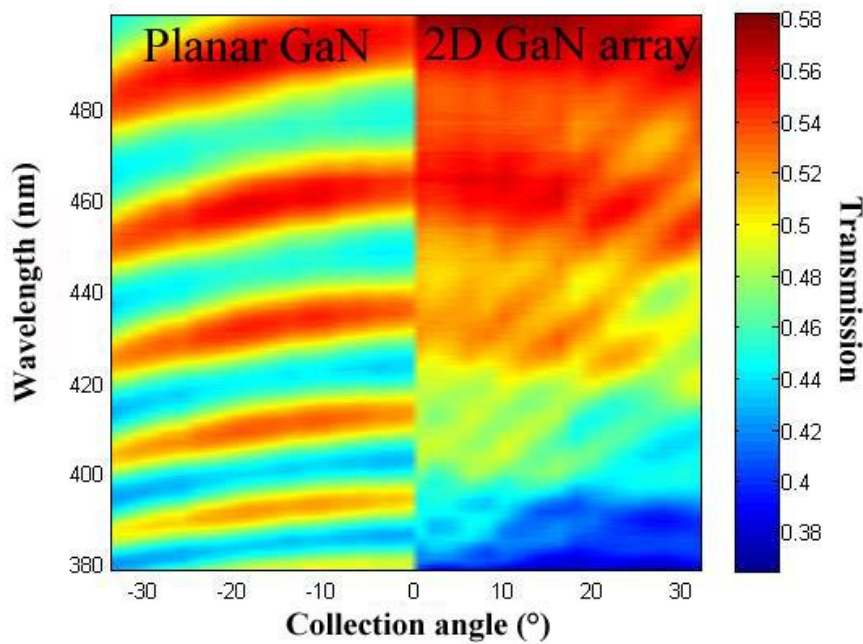


Figure 3.17. Angle-Resolved transmission spectra of planar GaN and 2D GaN periodic array structures.

The color bar in Figure 3.17 represents transmitted light intensity. The left side of the graph represents the transmission of planar GaN. A few nearly-horizontal lines with high

transmission are observed. These lines can be explained by thickness fringes from the GaN film as they were observed in the reflectivity measurements in Figure 3.15 as well. Such thickness fringes are not observed for the 2D periodic GaN arrays. This is explained by the anti-reflective behavior of the patterned surface. Instead, diagonal lines are observed. Such features were previously reported for angle-resolved photoluminescence spectra[142] of nano-patterned GaN/InGaN MQW structures. The diagonal lines are attributed to photonic crystal streaks. They arise from the folding of guided modes at the Brillouin Zone (BZ) boundary of the photonic crystal which become leaky when the modes are above the light line.[124, 142] This indirectly proves that the 2D pattern acts as a photonic crystal.

The transmission of the planar and patterned GaN at 400 nm as a function of collection angle was extracted from Figure 3.17. Figure 3.18 (a) shows the normalized intensity profile for planar GaN. It can be described by a Lambertian distribution ($I = (\cos \theta)^2$ -red line). The intensity profile of planar GaN and 2D periodic GaN arrays is shown in Figure 3.18 (b). An enhancement of the transmission is observed for all angles. In addition, several spikes at low angles are observed for patterned GaN exclusively. These spikes correspond to the diagonal lines in Figure 3.17 and are explained by light dispersion due to the photonic crystal effect. Integration over all angles highlights an enhancement of 13% for nano-patterned structures compared to planar structures, which fits perfectly with the value obtained from the integral reflection measurement (Figure 3.16 (b)).

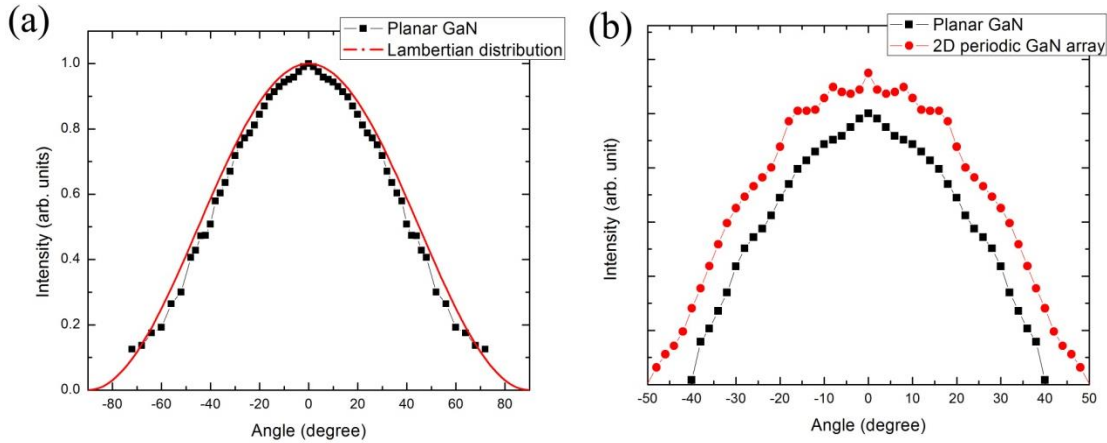


Figure 3.18. (a) Light intensity profile for planar GaN and (b) comparison between planar GaN and the 2D periodic GaN array.

3.4.3 Angle-resolved photoluminescence spectra of nano-patterned MQW structures

In order to test the potential of the investigated lithography techniques on LED structures, nano-patterning was also performed on AlGaN/AlN MQW structures on AlN single crystal substrate. The fabrication process for these samples was similar to what was described above for GaN films. A SiO₂ sphere monolayer was used as etching mask. The MQW structure consisted of ten pairs of AlGaN/AlGaN quantum well/barrier layer and patterned structures penetrating through the MQW active region. PL spectra were collected at different angles and compared to the planar MQW samples, aiming at providing direct evidence of enhanced light extraction due to nano-patterning.

As shown in Figure 3.19 (a) an increase of the MQW-related luminescence is observed after nano-pillar fabrication. Furthermore, a blue shift of the peak maximum of approximately 40 meV is observed for the sample with the patterned surface. Such a peak

shift corresponds to a reduced electrical field of 2.5×10^5 V/cm, however, the reason causing the reduced electrical field cannot be attributed to the relaxation of compressive strain inside the AlGaN/AlN MQW active region due to the opposite directions of the spontaneous and piezoelectric polarizations. Figure 3.19 (b) shows the integrated PL intensity of the nano-patterned and planar MQW structures collected at different angles. A 30% increase of the PL intensity integrated over all angles was achieved for nano-patterned MQW samples due to light diffraction from the corrugated nitride/air interface. A quantitative way to distinguish the effect of light extraction enhancement was described by Ondic et al.: [143]

$$I_{pattern}(\theta) = K(\theta) \cdot I_{planar}(\theta) \quad (3.4.4)$$

$$K(\theta) = A_{pattern}(\theta) C_{exe} \left(1 - \frac{\Delta V}{V_0}\right) \left(1 + \frac{\Delta S}{S_0}\right). \quad (3.4.5)$$

$I_{pattern}(\theta)$ and $I_{planar}(\theta)$ are the integrated intensities of the nano-patterned and planar MQW structures detected at one particular angle. $K(\theta)$ represents the enhancement factor which contains contributions from the enhancement of the extraction efficiency ($A_{pattern}(\theta)$), the enhancement of laser coupling into the patterned structure (C_{exe}), and a term considering the effect of partial removal of active region during patterning (ΔV and V_0 stand for the volume of the active medium that has been taken away and initial volume of the active medium). The last term, $(1 + \frac{\Delta S}{S_0})$, represents the change of the surface area of the active region due to patterning. Taking into account the experimental values

$$C_{exe} = 1.3 \quad 1 - \frac{\Delta V}{V_0} = 0.6 \quad 1 + \frac{\Delta S}{S_0} = 0.98, \quad (3.4.6)$$

a value of $A_{pattern}(\theta) \approx 1.7$ is calculated for the nano-patterned AlGaN/AlN MQW structures. This result clearly shows that a 70% enhancement in light emission can be expected due to light diffraction from the nano-patterned nitride/air interface.

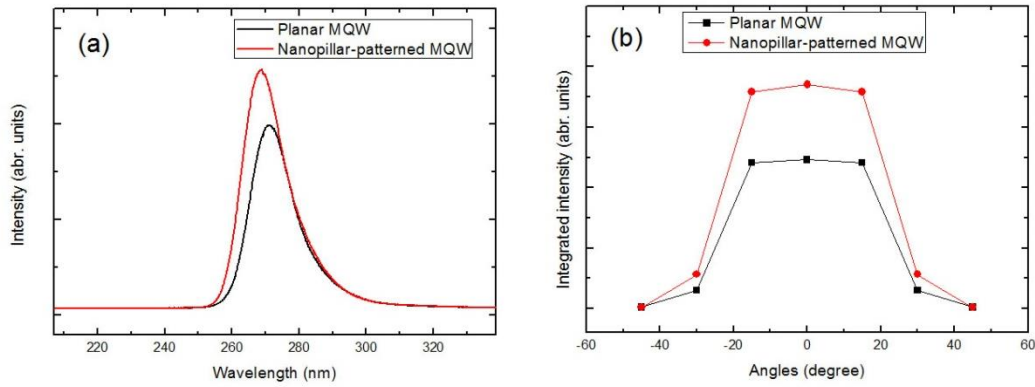


Figure 3.19. (a) Room temperature PL spectra of $\text{Al}_{0.5}\text{Ga}_{0.5}\text{N}/\text{AlN}$ MQW structures grown on an AlN substrate before and after nano-patterning collected perpendicular to the sample surface; (b) Integrated PL intensity of planar MQW and nano-pillar-patterned MQW structures collected at different angles.

3.5 FDTD simulation of the light extraction efficiency and the far-field emission profile of DUV-LEDs

As discussed in this chapter, an optimized design for DUV-LEDs with patterned surface is highly desired. Simulation of the device structure and its properties has proven to be useful for optimization.[124, 144] In the past, conventional ray-tracing method,[145]

Monte Carlo simulations,[146] and finite-difference time-domain (FDTD)[147] method have been used to simulate the light propagating behavior in nano-patterned LEDs. However, it was reported that the ray-tracing method may not be suitable for simulation of structures with sub-wavelength features.[148] Therefore, in this work FDTD simulations were performed to predict the influence of nanostructures on the light extraction efficiency. FDTD is a common simulation tool with the Maxwell solver (calculating electromagnetic field distribution) for the design, analysis, and optimization of optoelectronic devices with arbitrary geometry. Figure 3.20 (a) shows a schematic image of the simulated device design. The yellow rectangle marks the actual simulation domain. It consisted of 4 μm thick GaN acting as an LED. Similar to the 2D GaN arrays fabricated by interference lithography, the surface of the LED was covered with nano-pillars with the periodicity of 200 nm and 200 nm height. The light source was a randomly polarized dipole placed in the center of the GaN region. It was approximately 2 μm away from the top surface. An emission wavelength of 400 nm was simulated for direct comparison to the experimental angle-resolved transmission measurements (Figure 3.17) and intensity profiles (Figure 3.18(b)). The Perfectly-Matched-Layer (PML) boundary condition was applied to simulate absorbing side walls. Only light that reaches the top surface where surface patterning was performed was recorded and the comparison of far-field emission pattern between planar surface LED and nano-patterned LED was simulated. The actual LED can be treated as a combination of thousands of simulation domains repeated in a 2D array, and the active region of the LED can be interpreted as a line source in the middle of the GaN film.

The simulated far-field emission profiles of planar GaN and nano-patterned GaN-LEDs are shown in Figure 3.20 (b). As expected, the far-field intensities of planar GaN-based LEDs were nearly Lambertian. In contrast, the far-field intensity of the nano-patterned LED was modified with increased intensity at particular angles, especially normal to the structure. This is very similar to the observed experimental results. The simulated integrated emission intensity of the nano-patterned LEDs was 32% higher than that of a planar LEDs. The experimental enhancement factor calculated from Figure 3.18 (b) (13% higher) is lower than the theoretical prediction shown by FDTD simulation, which could be explained by a non-ideal periodic structure or light re-absorption inside GaN.

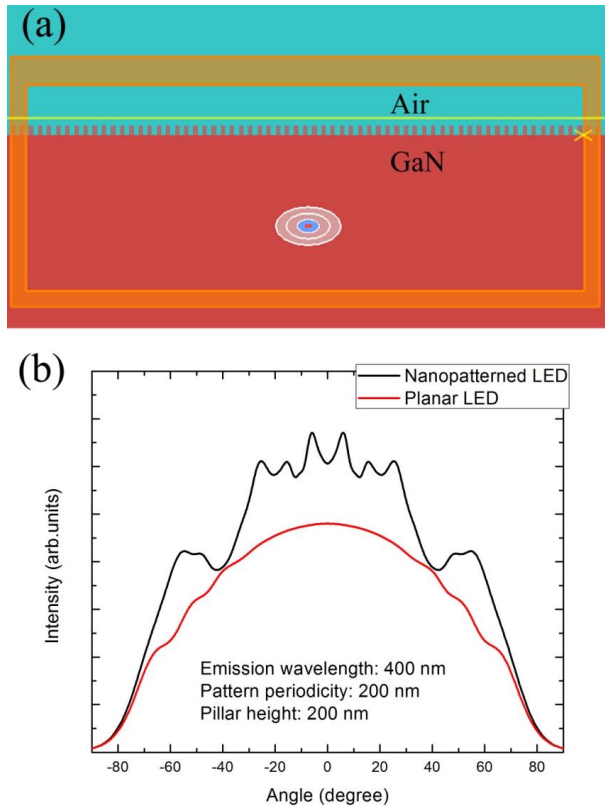


Figure 3.20. (a) FDTD simulation domains comprising nano-patterned LED structures on top of a GaN layer and **(b)** far-field intensity of nano-patterned LED in comparison to planar LED for emission wavelength around 400 nm.

3.6 Conclusions

The fabrication of nano-porous and nano-pillar structures on III-nitride substrates and Al_{0.5}Ga_{0.5}N/AlN MQW structures via natural lithography and interference lithography was demonstrated. It was shown that the natural lithography approach using AAO and SiO₂ sphere monolayers resulted in nano-porous material, inter-connected nano-pillar and free-standing nano-pillars with spacing of 100-130 nm. However, all patterns fabricated using

natural lithography offered only short-range periodicity. In contrast, the interference lithography approach led to both 1D and 2D long-range periodic nano-wall or nano-pillar structures with periodicity continuously adjustable from 200 nm to 1.5 μ m. Integral reflectivity measurement demonstrated a decrease of the reflectivity for GaN nano-pillars compared to planar GaN. It was concluded that this should allow for higher extraction efficiency in LEDs with patterned surface. Interestingly, 2D periodic GaN arrays showed the lowest reflectivity value. This demonstrates the unique advantage of the interference lithography. Angle-resolved transmission measurement of periodic 2D GaN array structures further confirmed that nanostructure-patterned LEDs had higher extraction efficiency as well as a highly directional emission profile compared to planar LEDs due to the light dispersion effect at the periodically varying semiconductor-air interface. Nano-patterned AlGaN/AlN MQW structure revealed a higher PL intensity compared to planar MQW structure, corresponding to an enhancement in light extraction efficiency in nano-patterned AlGaN-based DUV-LED. Finally, FDTD simulation of III-nitride based LEDs with nanostructures on top demonstrated that nano-patterning leads to 32% higher total far-field intensity in comparison with conventional planar LED at emission wavelength of 400 nm. In addition, a good agreement between the theoretical and experimental value was achieved. This is one of the first investigations on the influence of natural lithography and interference lithography on emission properties of DUV LEDs.

CHAPTER 4 Stimulated emission and optical gain measurements in AlGaN based Laser Diode structures

4.1 The influence of modal gain and gain threshold on the performance of laser diodes

Recent improvements of the crystalline quality and doping behavior of AlGaN films has led to a significant impact on the performance and lifetime of AlGaN based deep UV-LEDs.[63] However, electrical pumping of high Al content laser diodes (LDs) emitting at wavelengths below 320 nm have not been demonstrated.[65, 67-69, 149] Reliable p-type conductivity is still the main challenge to achieve electrical driven p-n junctions. Consequently, optical pumping above the bandgap of the AlGaN devices is still the only characterization technique to investigate the optical quality of the lasing region in DUV-LDs. [4, 149] The lasing threshold measured by optical pumping can be used as guidance for device design and structure optimization. Recently, optically pumped state-of-the-art AlGaN-based DUV-LDs grown on AlN substrates were achieved having a threshold of 84 kW/cm² at 264 nm.[74, 149] However, an improved understanding of the optical gain achieved within AlGaN-based materials is still crucial to further improve DUV-LD in terms of low lasing threshold, high output power and high efficiency.[150] As mentioned in Chapter 1, the gain coefficient, g (material gain) is a direct measure of material's potential for light amplification. In most cases, the material gain is proportional to the pumping threshold. In heterostructures like laser diodes, the active region or gain medium is usually sandwiched between two waveguiding or cladding layers that have a smaller refractive index. They provide an optical wave confinement in the direction perpendicular to the wafer surface and

toward substrate. The overlap between the active region and the field distribution of the confined optical mode is affected by different factors including the thickness of the active layer, and refractive index contrast between the active and the cladding layer. A non-ideal confinement results in mode penetration into the substrate region and therefore optical losses. The effective overlap between the optical mode and the active region is defined by the optical confinement factor Γ :

$$\Gamma = \frac{\int_{active} E^2(x) dx}{\int_{all} E^2(x) dx}. \quad (4.1.1)$$

where x is the growth direction. Taking into consideration the optical confinement, the net modal gain is presented as below, where G is modal gain and α_{int} is the internal loss:[151]

$$G = \Gamma g - \alpha_{int}. \quad (4.1.2)$$

The gain coefficient depends on the steady state carrier concentration in the active region. If the carrier concentration increases, the gain coefficient also increases. A positive modal gain is achieved if Γg overcomes the losses ($\Gamma g > \alpha_{int}$). Detailed techniques in measuring modal gain values will be discussed in the next section.

The gain characteristics of GaN and $Al_xGa_{1-x}N$ materials have been analyzed both theoretically[152, 153] and experimentally.[40, 154] For example, the influence of the temperature and the Al content on the stimulated emission and gain threshold (transparency condition, when gain surpasses loss) of AlGaN materials were investigated by Mickevicius et al. and Schmidt et al.[154, 155] They observed an increase of the threshold power density

with increasing the Al content between 8% and 35%. Furthermore, it was observed that the gain value decreases from GaN to AlGaN with increasing Al-concentration.[156] However, most of this work is focused on the gain characteristic of AlGaN materials having an Al content below 35%.

Investigations on Al rich alloys are limited due to their poor material quality. Typically, the AlGaN layers were grown heteroepitaxially on sapphire[40, 154] or SiC substrates.[64] The large lattice mismatch between the substrates and the film led to a high dislocation density and increased associated point defect incorporation. They act as non-radiative centers significantly limiting the optical quality of the epitaxial films. In contrast, as single crystalline AlN substrate with low dislocation density became available, the homoepitaxial growth of large gain and low lasing threshold AlGaN LD structures was enabled. As mentioned in Chapter 1, AlGaN LD structures grown on AlN single crystalline substrate resulted in record low thresholds value of 84 kW/cm² for sub-300 nm lasing.[73, 74] Therefore, systematic studies of the gain characteristic of bulk AlGaN and AlGaN-based heterostructures grown on AlN substrates will lead to in-depth understanding of the intrinsic properties of this material system and provide guidance in the device design.

In this chapter, the gain spectra and gain thresholds of a single AlGaN layer, an AlGaN double-heterostructure (DH), and an Al_{0.5}Ga_{0.5}N/Al_{0.7}Ga_{0.3}N Multiple-Quantum-Well (MQW) structure grown by metalorganic chemical deposition (MOCVD) on top of bulk AlN substrates were investigated.[22][23, 24] Stimulated emission was observed from 250 nm to 270 nm with material gain values of up to 60 cm⁻¹. The lowest gain threshold was achieved at

150 kW/cm² for the MQW structure. In addition 6-band k·p simulation was carried out to theoretically calculate the material gain spectra as well as the mode distribution for all structures. They allow to improve the design of the LD structures in order to achieve higher modal gain values and lower lasing thresholds.

4.2 Experiment procedure

Three different high Al content AlGaN structures were investigated: (a) a single AlGaN film, (b) a double heterostructure, and (c) a MQW structure. A schematic sample structure is shown in Figure 4.1. The single AlGaN film sample consists of a 200 nm thick AlN homoepitaxial film followed by a nominal 300 nm thick Al_{0.7}Ga_{0.3}N layer. The DH structure consists of 500 nm thick Al_{0.7}Ga_{0.3}N, a 20 nm Al_{0.6}Ga_{0.4}N and a 10 nm Al_{0.7}Ga_{0.3}N top layer, grown on a 200 nm thick AlN homoepitaxial layer. Finally, the MQW structure consists of a 200 nm thick AlN homoepitaxial layer, a 500 nm thick Al_{0.7}Ga_{0.3}N layer and 10 pairs of wells and barriers of Al_{0.5}Ga_{0.5}N/Al_{0.7}Ga_{0.3}N (1.6 nm wells/4 nm barriers). Atomic force microscopy (AFM) investigations of all three samples exhibited a smooth surface morphology characterized by bi-layer steps. The related root mean square (RMS) values are less than 0.3 nm within a 5×5 μm² scan area. Further details on the epitaxial growth and the preparation of the AlN substrates can be found elsewhere.[19, 22]

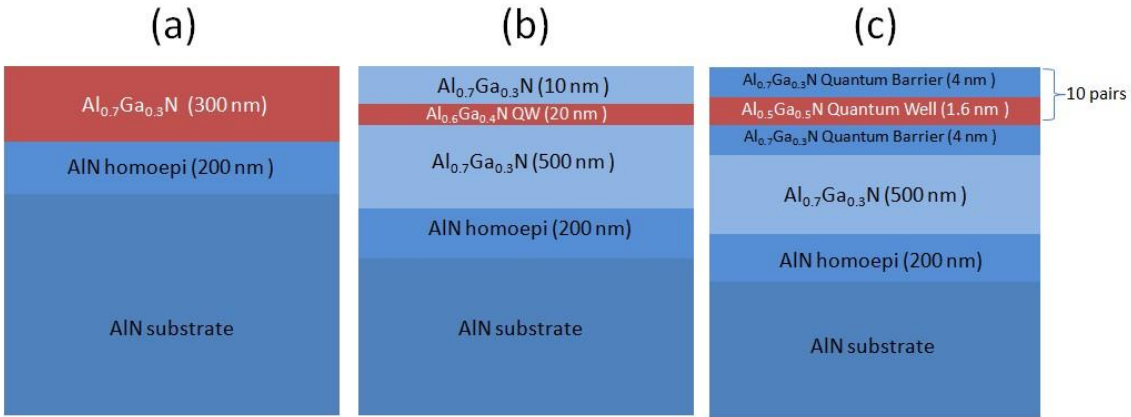


Figure 4.1. Schematic setup of the investigated AlGaN samples. (a) single Al_{0.7}Ga_{0.3}N film, (b) a double heterostructure, and (c) MQW structure.

To measure the modal gain, the variable-stripe-length (VSL) method was used.[157, 158] The details of the setup are shown in Figure 4.2 (a). In the VSL method, the spontaneous and stimulated emission from a sample is collected as a function of the excitation length, l , illuminated on the sample surface (stripe pattern). The relation between the intensity of the emission and the excited stripe length on the sample surface can be described as:

$$I_{ASE}(l, \lambda) = \frac{A}{G(\lambda)} (e^{G(\lambda)*l} - 1), \quad (4.2.1)$$

where $I_{ASE}(l, \lambda)$ is the amplified spontaneous emission intensity, A is a constant related to the spontaneous emission intensity, and G denote the modal gain.

As pumping source, a pulsed Argon-Floride (ArF) laser with excitation at a wavelength of 193 nm, a repetition rate of 10 Hz, and a pulse width 5 ns was used. The laser

spot was focused by a cylindrical lens in order to achieve a homogeneous excitation stripe on the sample surface (along m -direction of the sample). The width of the stripe was approximately 100 μm . The stripe length (l) could be varied between 100 μm and 900 μm by using a motorized one-dimensional slit placed between the cylindrical lens and the sample. To allow measurements at different sample positions, the sample was mounted on a micrometer translation stage, which provided variable positioning in the x, y, and z direction. The distance between the slit and the sample surface was controlled to be as small as possible in order to avoid the effects of Fresnel diffraction at the edges of the slits. Diffraction causes an inhomogeneous pumping power profile across the excited region on the sample and large uncertainty in stripe length estimate. In our setup, a distance of approximately 1 cm was used within the constraint of the setup.

The luminescence signal was collected perpendicular to the excitation laser through a cleaved m -facet of the sample by using an optical fiber (Figure 4.2 (a)). The fiber was attached to a Princeton Instruments Acton SP2750 monochromator having a focal length of 0.75 m and a 150 lines/mm grating. Finally a Peltier-cooled charge-coupled device (CCD) camera was used to acquire the spectra. In addition, the emission at a detection angle of 45° with respect to the sample surface normal was recorded, see Figure 4.2(b).

In order to allow measurements of the gain threshold of our AlGaN based structures the pumping power of the laser was reduced by neutral density filters. The specific excitation power density for each filter-laser assembly was determined by a Coherent Labmax-Top™ laser power meter appropriate to account for the whole spot size of the laser beam. Excitation

dependent measurements were performed over a broad range of excitation powers changing by more than one order of magnitude and variable stripe length. Furthermore, the polarization dependence of the edge emission was analyzed using an Alpha-BBO Glan-Laser polarizer placed in front of the monochromator entrance slit.

The intensity of the edge emission is highly affected by the cleaving of the sample. Several requirements are necessary to achieve consistent and comparable experimental results: (1) a smooth cleavage edge to reduce light scattering at the cross-sectional surface; (2) perpendicular alignment of the cleaved edge with respect to the sample surface, so that the edge emission can be collected by an optical fiber. At a distance of 1 cm from the sample edge, a numerical aperture of 0.22 was obtained. A cross-section SEM image of the single AlGaN layer is shown in Figure 4.3. It exhibits a smooth m-plane surface. The estimated thickness of approximately 300 nm matches well with previous XRD result. It is worth noting that not every edge position on the sample provides a good quality cleavage. Depending on the position, the stimulated emission intensity and the calculated gain values vary by about 20%. In the present work, the highest intensity or gain value achieved on a particular sample was used.

The measured experimental results were also compared to simulated gain spectra and the calculated mode distribution properties using the *Silvaco* device simulation packages. Since this commercial simulation package does not allow computing the device characteristics under optical pumping, an electrical injection was assumed instead.

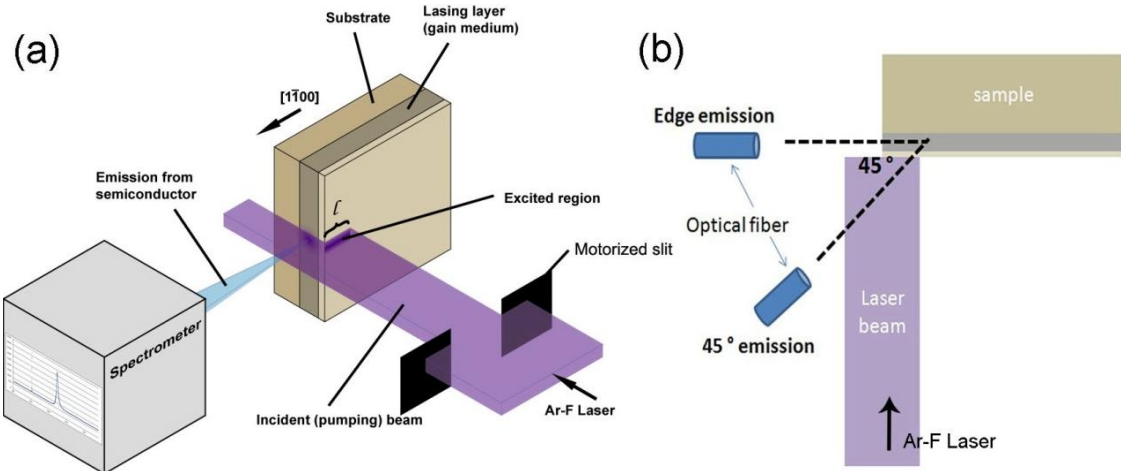


Figure 4.2. Schematic diagram of the variable-stripe-length experimental setup for a collection of the sample luminescence from the edge (a) and sketch of luminescence collected from the edge of the sample and in a 45° configuration (b).

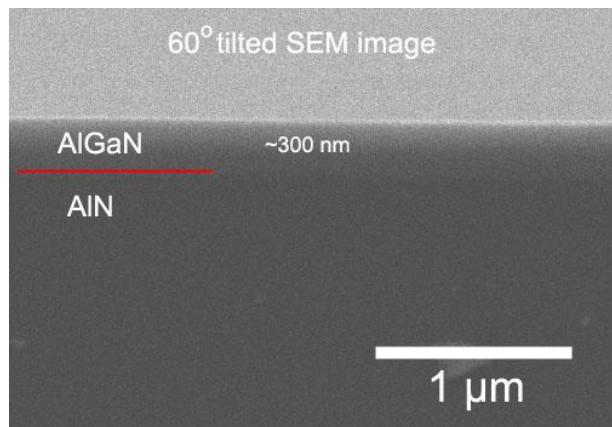


Figure 4.3. SEM image (60° tilted with respect to sample surface) of the cleaved single AlGaN epitaxial layer grown on an AlN substrate. The thickness of the AlGaN film is ~ 300 nm. It indicates a smooth cleavage facet, which is desirable for optical gain measurement.

4.3 Stimulated emission and polarization characteristics of AlGaN heterostructures

In order to compare the stimulated emission with spontaneous emission, the surface emission was first collected at an angle of 45° to the surface normal of the epitaxial c-plane under low pumping power ($<50 \text{ kW/cm}^2$). As an example, the emission spectra and the peak intensity as a function of pumping power for the single AlGaN epitaxial layer are shown in Figure 4.4. A broad emission peak having a FWHM larger than 7 nm centered at 246 nm was observed. The spectral peak position indicated an Al composition of the AlGaN film of 70% if bowing parameter of 1.08 eV was used.[44] With moderate increase of the pumping power, no peak shift attributed to band filling or renormalization effects was observed. The peak intensity exhibited a linear behavior with increasing excitation power density in the range of the considered pumping powers below 50 kW/cm^2 . A similar dependency is expected for a spontaneous emission behavior since the recombination rate is proportional to the concentration of electron-hole pairs generated by the incident laser. An equivalent spontaneous emission action is observed for the DH as well as the MQW structure for pumping powers below 50 kW/cm^2 .

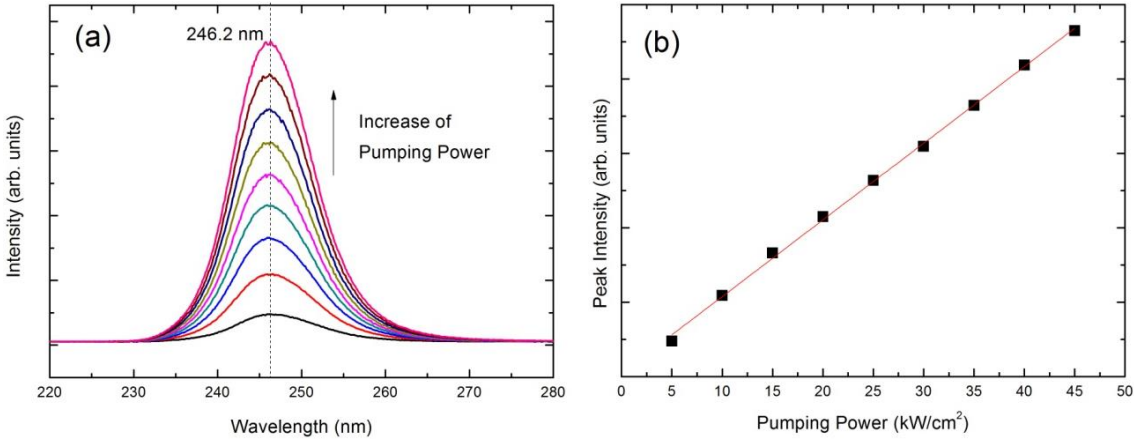


Figure 4.4. Spontaneous emission spectra collected at an angle of 45° normal to the top surface of the AlGaN epitaxial layer for various pumping powers; (b) Peak intensity as a function of the pumping power for the AlGaN epitaxial layer, the red line shows a linear fit of the data points.

A comparison of the edge emission spectra of the single AlGaN layer, the AlGaN DH structure, and the AlGaN MQW structure under various pumping powers above 50 kW/cm² are shown in the Figure 4.5 (solid lines). All structures show a similar excitation dependent behavior. As an example, the power dependency is explained in detail for the single AlGaN epitaxial layer shown in Figure 4.5 (a). For small pumping powers, the edge luminescence exhibits a broad peak similar to the surface emission. However, when the pumping power is increased to about 400 kW/cm², a sharp emission peak emerges on top of the spontaneous emission peak (blue line in Figure 4.5 (a)). Since the length of the excited stripe on the sample is far above the absorption length, the emitted light is either absorbed or amplified via stimulated emission. The ratio between the absorption and emission processes depends on the excitation density (population inversion), which can be elegantly described by the Einstein coefficient. For high excitation densities, the probability of stimulated emission increased

drastically and led to a dominant sharp stimulated emission peak over the spontaneous emission. The stimulated emission related peak was located at the long-wavelength-side of the spontaneous emission peak, probably due to stronger re-absorption at the high-energy parts of the spontaneous emission spectrum. Upon increasing power density, a slight blue shift of less than 0.8 nm was observed. It could originate from a gradual filling of localized states.[159]

The edge emission of the DH and the MQW structures (Figure 4.1 (b) and (c)) was characterized following the same procedure. The spectra are shown in Figure 4.3 (b) and (c). According to the single AlGaN layer, narrow edge emission peaks dominate the spectra at high pumping powers. Depending on the intended Al composition of the different active regions of the three structures, the emission peak energies are shifted. However, the achieved line widths of the stimulated emission peaks are comparable for all structures. The same holds true for the spontaneous emission distribution collected from the top surface of the samples.

The shape of the spontaneous emission peak is found to be asymmetrically broadened, or even consisting of multiple peaks for the DH and MQW structure. This may result from composition and thickness non-uniformity within the nanoscale active region of these structures. In addition, the observed peak separation between the spontaneous and the edge emission is smaller in case of the investigated heterostructures (DH, MQW) compared to the single AlGaN film. The strong confinement of the carriers could result in weaker re-absorption of light on the low energy side of the spontaneous emission peak. Consequently

the stimulated emission line arises at energies close to the maximum of the spontaneous emission distribution.

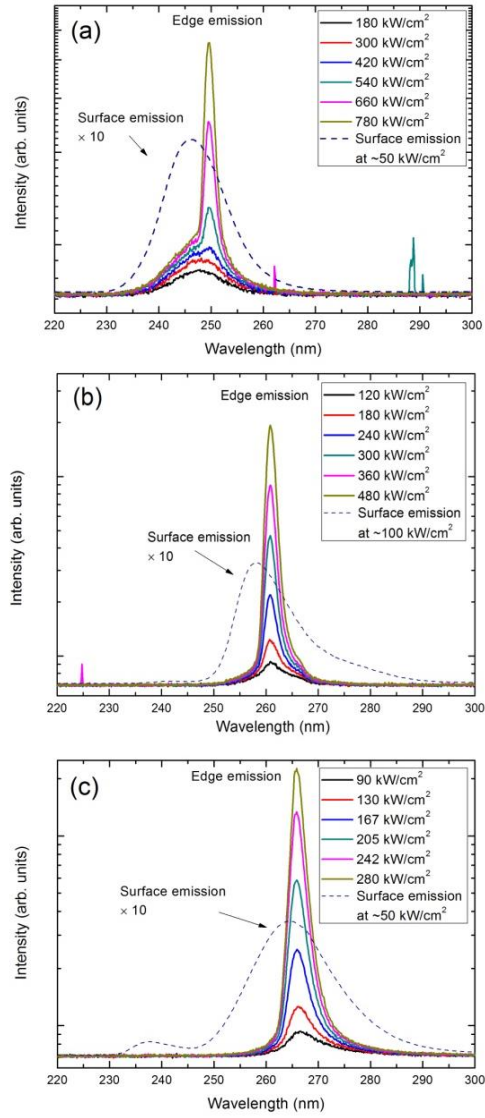


Figure 4.5. Comparison of the edge emission spectra (solid lines) and the surface emission recorded at an angle of 45° normal to the top surface (dashed line) of the single AlGaN film (a), the AlGaN-DH (b), and the AlGaN-MQW (c) structure for pumping powers between 100–800 kW/cm².

Figure 4.6 shows the quantitative values of the peak intensity and the FWHM of the edge emission of the single AlGaN layer, DH structure, and MQW structure as a function of pumping power. A super-linear enhancement of the peak emission intensity is observed, suggesting the onset of light amplification via stimulated emission.[64, 155] This fact is further confirmed by the FWHM of the emission peak, which underwent a radical reduction, down to 1.8 nm, within the same power density range. From the change of the slope of the stimulated emission intensity and the drop of the FWHM, the onset of stimulated emission was observed at pumping powers of less than 400 kW/cm², 200 kW/cm², and 150 kW/cm² for the single AlGaN layer, the DH structure, and the MQW structure, respectively. At the given pumping powers, the gain threshold (transparency condition) is reached and the net modal gain becomes positive.

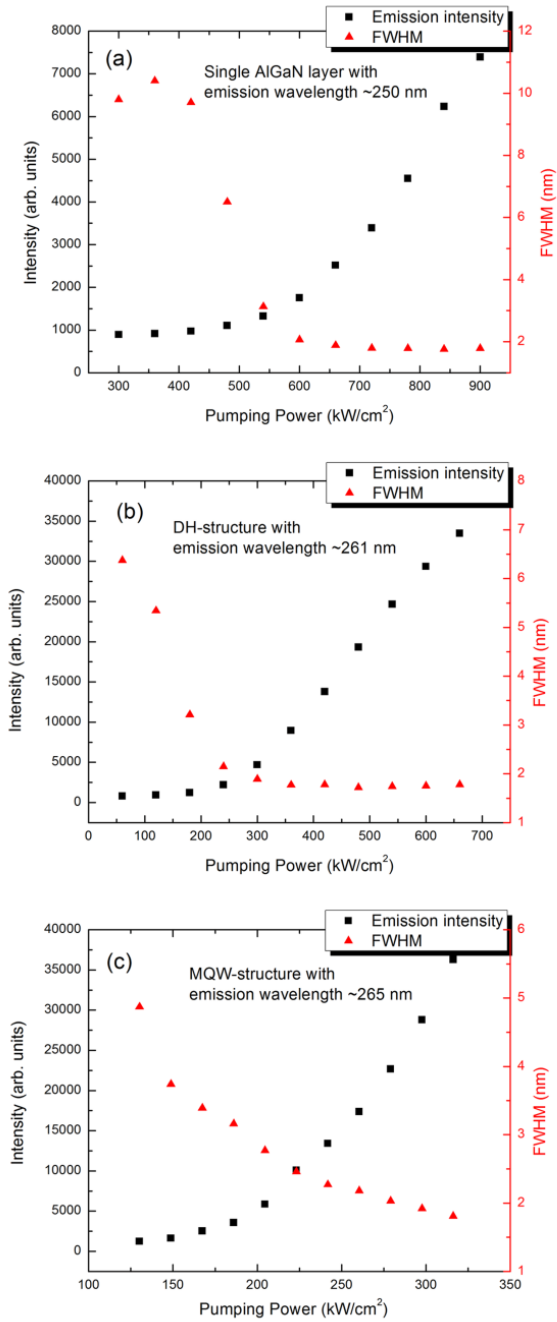


Figure 4.6. Peak emission intensity (black squares) and resulting FWHM (red triangles) with increasing pumping powers for (a) a single AlGaN layer, (b) a DH structure, and (c) a MQW structure measured at room temperature.

A further proof of the onset of stimulated emission is enabled by polarization dependent measurements. Above threshold, an emission characterized by a well-defined polarization state is expected.[160, 161] Figure 4.7 shows the polarization dependency of the edge emission of the single AlGaN film for pumping powers above (Figure 4.7 (a)) and below (Figure 4.7 (b)) the stimulated emission threshold. It is clearly observed that the edge emission above the threshold is strongly TE polarized with a degree of polarization of around 90%. However, at lower pumping powers below the threshold, where the spontaneous emission dominates, the degree of polarization is significantly reduced. A similar pronounced onset of a strong TE polarization of the edge emission above the stimulated emission threshold is observed for both the DH as well as the MQW sample.

By increasing the Al content, the band ordering changes due to a transition between a positive to a negative crystal field splitting.[162, 163] Therefore, a crossover of the crystal-field split-off hole (CH) and heavy hole (HH)/light-hole (LH) bands accompanied with a change of the polarization from TE to TM is expected. Considering that the AlGaN epitaxial layers were grown pseudomorphically on the AlN template layer with in-plane biaxial strain, the Al composition from the AlGaN active region probably had not reached the critical point where the stimulated emission changes from TE polarization dominated to TM polarization dominated.[164-166]

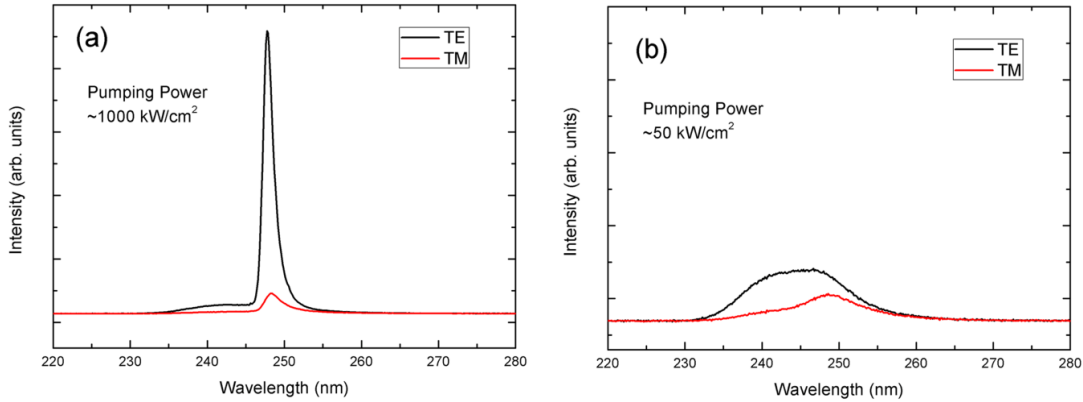


Figure 4.7. TE and TM emission spectra collected from the edge of the single AlGaN layer sample at a pumping power of 1000 kW/cm^2 (a) and 50 kW/cm^2 (b). All spectra were normalized with respect to the emission maximum of the TM polarized light for easier comparison.

4.4 Gain spectra and threshold values of AlGaN heterostructures

The calculation of the gain spectra is based on the relationship between the stimulated emission and the stripe length. In Figure 4.8, the dependency of the emission peak intensity on the stripe length is shown for all three samples at different excitation power densities. The single AlGaN layer shows a linear response to the increase of the stripe length for an excitation density of 300 kW/cm^2 . For the higher pumping powers of 700 kW/cm^2 and 1000 kW/cm^2 , a super-linear dependency is observed. It indicates a positive gain value for the emitting medium. In the case of the single AlGaN epitaxial layer, no optical confinement was assumed. Therefore, the found positive gain value demonstrated the good optical quality of our AlGaN epitaxial layer. For the DH and the MQW structure, a super-linear enhancement of the emission intensity with increasing stripe length is observed for all excitation power densities and the super-linearity of the emission intensity increased as a function of pumping

power. This behavior is expected as the population of the excited states is enhanced with increasing pumping power. Consequently, higher optical gain values could be achieved.

Following equation (4.2.1), the optical gain values could be calculated by linear regression. Assuming that $e^{G(\lambda)*l}$ is much larger than 1, equation (4.2.1) could be rearranged to:

$$\ln I_{ASE} = \ln\left(\frac{A}{G(\lambda)}\right) + G(\lambda) \times l \quad (4.4.1)$$

Finally, the optical gain is given by the slope of the semi-logarithmic plot of the amplified spontaneous emission intensity, I_{ASE} and stripe width l .[157] However, for small gain values, which is especially the case for the investigated AlGaN materials, the above used approximation does not hold. Now the exponential term in equation (4.2.1) is of the order of 1 and so the “-1” term within the brackets in (4.2.1) cannot be neglected. Instead, a direct fitting of equation (4.2.1) to the measured peak intensity graph yields a higher precision. Comparing both methods, the estimation of the gain value using the slope of the $\ln(I_{ASE}) - l$ plot results in a 20% overestimation of the gain values. The direct fitting of the experimental data at an excitation power density of 1000 kW/cm² in Figure 4.8 exhibits the maximum gain values of 17 ± 1 cm⁻¹, 58 ± 3 cm⁻¹, and 48 ± 2 cm⁻¹ for the single AlGaN layer, the DH structure, and the MQW samples, respectively.

In order to achieve an accurate estimation of the gain values, the stripe length was adjusted. If the stripe length exceeds a critical value, the slope of the intensity-stripe length graph decreases. A fitting of the data would result in an under-estimation of the optical gain

value. According to Dal Negro et al.,[151] this behavior could be attributed to a gain saturation effect. The stimulated emission may deplete the excited states population, causing a reduction or even complete cancelation of the population inversion. A further increase of the excitation stripe length or the pumping power would not increase the light amplification by stimulated emission. To avoid this saturation effect, all presented experimental results were carried out at stripe lengths below 600 μm .

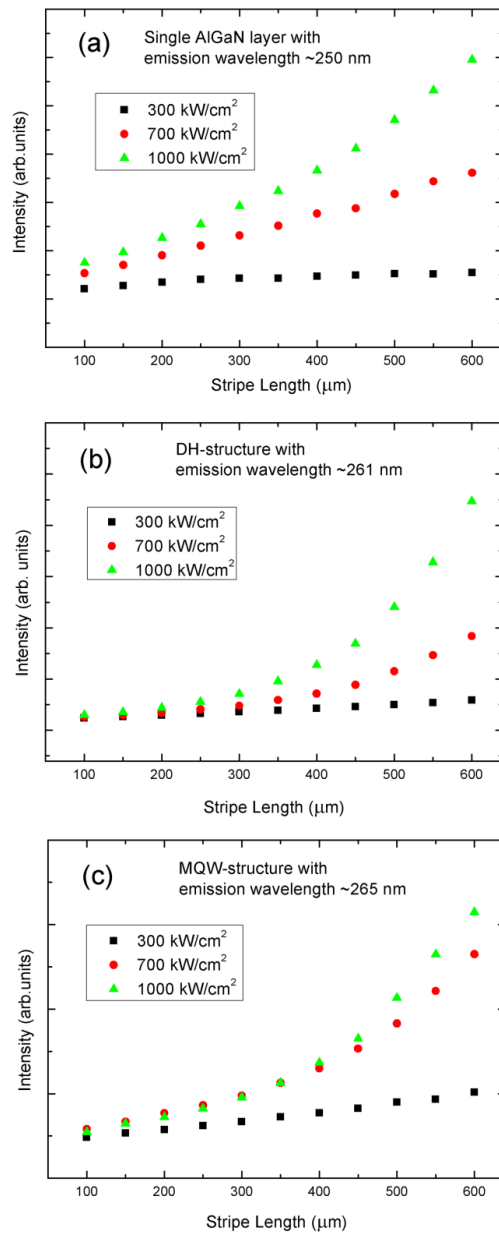


Figure 4.8. Stimulated emission peak intensity as a function of stripe length for (a) the single AlGaN layer, (b) the DH structure, and (c) the MQW samples under different pumping powers of $300 \text{ kW}/\text{cm}^2$, $700 \text{ kW}/\text{cm}^2$, and $1000 \text{ kW}/\text{cm}^2$.

Table 4.1 summarizes the calculated maximum gain values at different pumping powers and the threshold densities for all three AlGaN based structures. Higher gain values and a delayed onset of saturation is expected at higher excitation power densities due to an increased number of excited states.[151] As expected, the gain values of the DH and MQW structure are higher than those achieved on the single AlGaN layer, where the carrier confinement is absent.

A comparison of the modal gain values at different pumping powers for all three different structures is given in Figure 4.9. The dashed lines show a linear extrapolation of the measured data to a modal gain value of zero. The intercept corresponds to the gain threshold. The estimated values are 700 kW/cm² for the single AlGaN layer, 250 kW/cm² for the DH structure, and 150 kW/cm² for the MQW sample. As expected, all threshold values are larger than the critical values of the onset of stimulated emission (less than 400 kW/cm², 200 kW/cm², and 150 kW/cm² for the single AlGaN layer, the DH, and the MQW structure). The light amplification by stimulated emission needs to be larger than the losses in order to obtain a positive net modal gain.

Table 4.1. Maximum net optical gain values at different pumping powers and the estimated gain threshold values for the three investigated AlGaN-based samples.

| | Gain value (cm ⁻¹) | | | Gain threshold value (kW/cm ²) |
|---------------|--------------------------------|------------------------|-------------------------|--|
| | 300 kW/cm ² | 700 kW/cm ² | 1000 kW/cm ² | |
| Single AlGaN | - | 2 | 17 | 700 |
| DH structure | 6 | 49 | 58 | 250 |
| MQW structure | 11 | 36 | 48 | 150 |

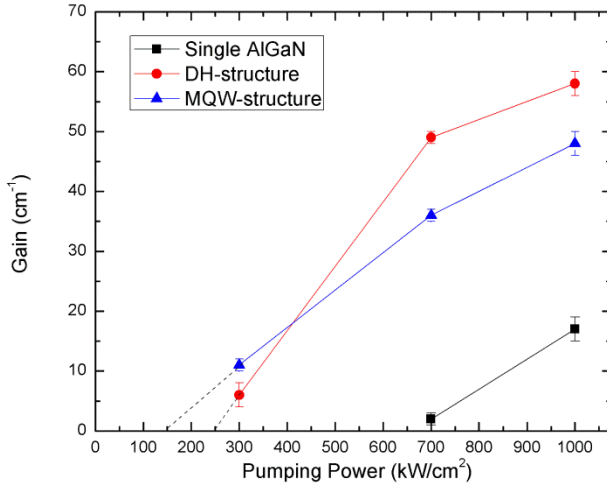


Figure 4.9. Maximum optical gain values as a function of the pumping power for three different samples.
The gain threshold values were estimated by the intercept of the linear extrapolation of the data with a gain value equals to zero.

Using the software package *Matlab* (see Appendix A for details), the spectral dependence of the gain values could be deduced by fitting the experimental data of the intensity I_{ASE} as a function of the stripe length for various wavelengths around the emission peak maximum. The resulting modal gain spectra at different pumping powers for all three samples are plotted in Figure 4.10. The modal gain increases to its maximum value at a critical point $E_c > E_g$ with decreasing wavelength. At this energy, the stimulated emission peak occurs. A further decrease of the wavelength results in a drop of the gain curve to negative values. Now, absorption within the gain medium is enhanced which limits the amplification ($\Gamma g \leq \alpha$, following equation (4.2)).[33] The found peak modal gain values correspond well to the data shown in Table 4.1. For the single AlGaN structure, a positive gain is observed at

pumping power above 700 kW/cm² even though no confining structure is present. Consequently, a good optical quality of the AlGaN epitaxial layer grown on an AlN bulk crystal is assumed. In contrast, the electrical confinement in the DH and MQW structure facilitates the achievement of the population inversion condition, resulting in higher gain values compared to the single AlGaN film. In addition, a similar small blue shift (< 1 nm) of the gain maximum was observed for all three structures with increasing pumping power. The decrease of the peak maximum could be attributed to a band filling effect.[153]

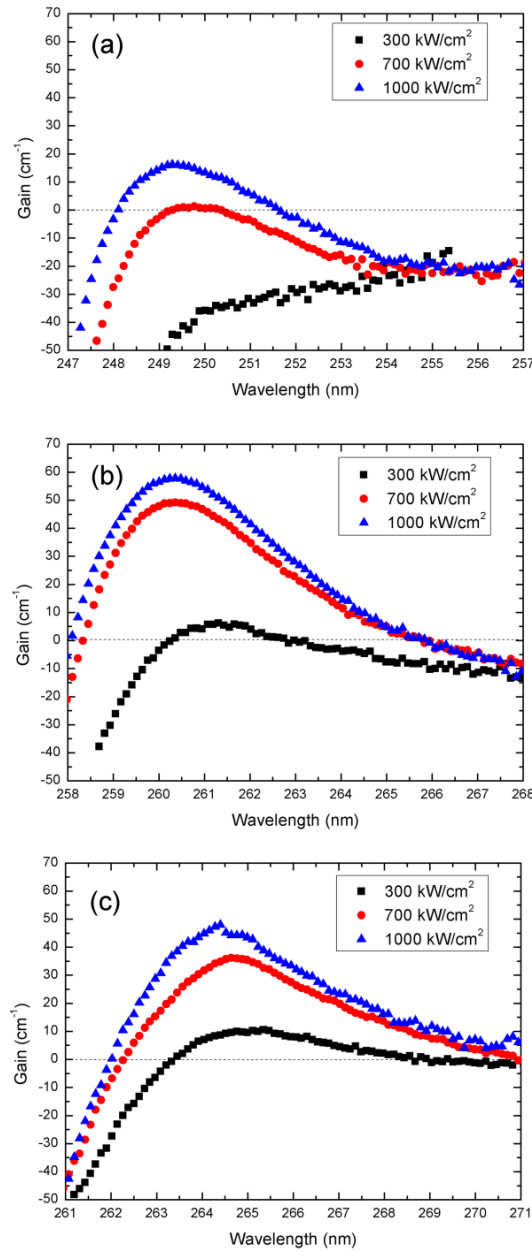


Figure 4.10. Spectral dependency of the net modal gain value for three different pumping power for the (a) single AlGaN layer, (b) DH structure, and (c) MQW sample.

So far, our discussion of the gain measurements by using the variable-stripe-length method was limited to three different pumping powers: 300 kW/cm^2 , 700 kW/cm^2 , and 1000 kW/cm^2 . An enhancement of the gain value is expected with an additional increase of the pumping power due to a larger contribution of excited states. In order to demonstrate this trend, higher pumping powers of 2000 kW/cm^2 and 3000 kW/cm^2 were applied to the single AlGaN layer sample. As shown in Figure 4.11 (a), an increased maximum gain value of 38 cm^{-1} could be achieved at a pumping power of 2000 kW/cm^2 . A further enhancement of the pumping power leads to a decrease of the modal gain. For very high excitation densities gain saturation effects and surface overheating or even surface damage limit the gain performance. A quantitative analysis of the gain spectra for low and high pumping powers is shown in Figure 4.11 (b).

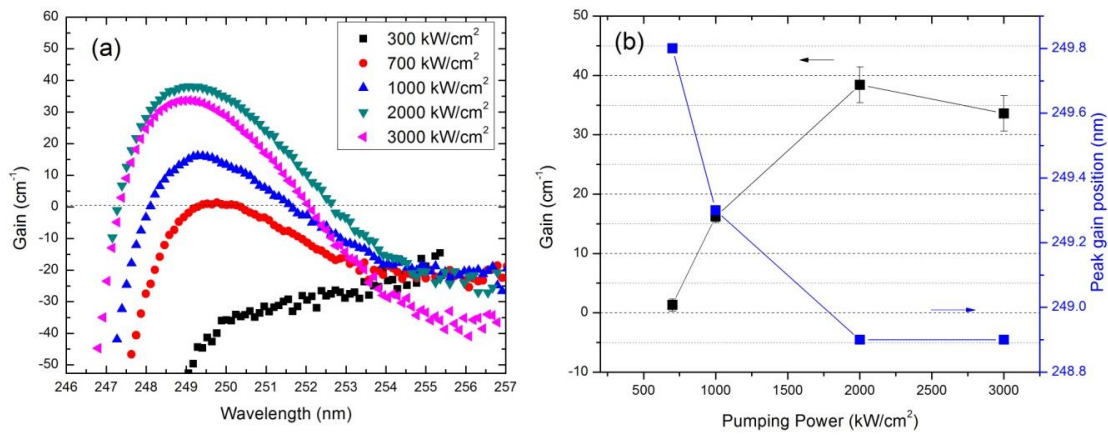


Figure 4.11. Modal gain spectra under low and high pumping powers densities measured at the single AlGaN structure (a); Maximum gain values and the corresponding spectral peak positions as a function of the pumping power for the single AlGaN layer (b).

4.5 Simulation of the gain characteristic and the LD structural design

Gain characteristics of the AlGaN layers and AlGaN based heterostructures were investigated theoretically using the commercial simulation package *Silvaco*. The electronic properties like the band structure and the density of states are calculated based on 6-band $k \cdot p$ theory while optical confinement is taken into account by solving the Maxwell equations. As input parameters, the measured layer thicknesses, refractive indexes and other optical properties were used. Finally the gain spectra of our three investigated AlGaN-based structures were calculated for electrical pumping. As direct optical pumping is not considered in the software package, electrical injection is assumed and all simulated excitation powers were converted to an excitation power density for a direct comparison to our measured results. The simulated material gain spectra for the three different structures are depicted in Figure 4.12. As expected, a higher equilibrium carrier concentration within the active layers leads to higher material gain values due to an increased number of excited states involved in the recombination process. The calculated spectral positions of the gain maxima for the single AlGaN layer, the DH and MQW-structure are at 245.5 nm, 255 nm, and 262 nm, respectively. The increase of the peak wavelength of the three different structures is in accordance with the decreasing Al composition in the active media from the single AlGaN layer to the DH structure and MQW sample. However, all values are lower than the measured experimental results. Possible explanations could be light re-absorption of defects in the structures or a difference in Al composition between the actual structures and targeted structures.

The equilibrium carrier concentration inside the active region increases as a function of the applied bias until it is finally saturated. Comparing all three structures, the highest achievable total carrier concentration accumulated within the active medium is the lowest for the single AlGaN layer ($1 \times 10^{19} \text{ cm}^{-3}$). A slightly higher carrier concentrations of $4 \times 10^{19} \text{ cm}^{-3}$ and $5 \times 10^{19} \text{ cm}^{-3}$ are found for the DH structure and the MQW sample, respectively, due to a specific carrier confinement in the active region. As a consequence, the calculated maximum material gain value is also the lowest (2.5 cm^{-1}) in the case of the single AlGaN layer compared to the DH and MQW structure (330 cm^{-1} and 5600 cm^{-1} , respectively). The highest achieved material gain value is found for the MQW sample. Due to a 2 dimensional quantum confinement, the charge carriers are strongly localized within the quantum well layers. For this, the density of states changes to a step-like distribution rather than the expected parabolic function in the three dimensional case. The larger confinement results in an enhanced spatial overlap between the electron and hole wave functions within the quantum wells and therefore an increased carrier recombination rate at a well-defined transition energy.[33]

A direct comparison of the gain spectra under electrical and optical pumping is feasible by correlating the carrier concentration to the optical pumping power. By taking into account specific material parameters like the radiative recombination coefficient (B), absorption coefficient (α), and internal quantum efficiency (IQE) for our AlGaN structures, the used carrier concentration of $5 \times 10^{19} \text{ cm}^{-3}$ would correspond to an optical pumping power of approximately 600 kW/cm^2 .[167]

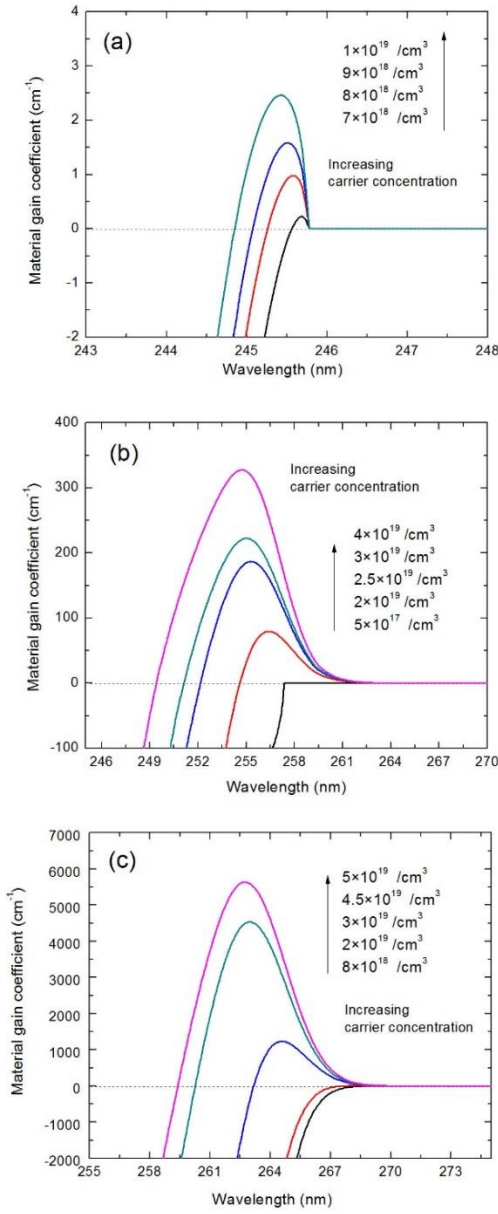


Figure 4.12. Simulated material gain spectra for different carrier concentrations within the (a) single AlGaN layer, (b) the AlGaN based DH structure, and (c) the MQW sample.

As mentioned in the first section and expressed by equation (4.1.2) the modal gain (G) depends on the material gain (g) and the optical confinement factor (Γ). In order to

further understand the influence of the optical confinement factor on the modal gain value, mode profiles were simulated and an estimation of the optical confinement factor is enabled by the calculation of the optical mode distribution within our AlGaN based structures. Figure 4.13 shows the spatial distribution of the simulated fundamental waveguide mode and the refractive index within the single AlGaN epitaxial layer. The mode is mainly confined in the AlGaN film. The optical confinement factor reaches ~91%. However, in the case of the confined heterostructures (DH, and MQW sample), the optical mode cannot be effectively confined inside the active region. As an example, the Figure 4.14 shows the spatial mode distribution of the fundamental TE (a), the second harmonic TE (b), and the third harmonic TE (c) mode inside the MQW structure. The maxima of the different optical modes are mainly located within the lower AlGaN waveguide layer, rather than in the MQW region (Figure 4.14 (a)-(c)). The confinement factors are estimated to 0.9%, 1.5%, and 3.2% for the three different harmonic modes. The low values arise from the reduced total thickness of the MQW region of about 16 nm ($\sim 1.6 \times 10 = 16$ nm), the small refractive index contrast between the MQW region and the underlying AlGaN cladding layer, and the highly asymmetric waveguide design using a 500 nm thick lower AlGaN waveguide layer and a only 4 nm thick upper AlN cladding layer.

To determine the net modal gain by the use of equation (4.2), besides the confinement factor, the internal losses within the active medium had to be estimated. They could be extracted from the asymptotic behavior of the gain spectra at the low-energy side when the gain coefficient vanishes.[168] According to Figure 4.10, the net modal gain is estimated to be around -25 cm^{-1} , -15 cm^{-1} , and -3 cm^{-1} , for the single AlGaN layer, DH structure, and

MQW sample, respectively. Therefore, internal losses are 25cm^{-1} , 15cm^{-1} and 3 cm^{-1} , respectively. Combining all parameters in equation (4.2), the highest modal gain value of: $5600 \times 3.2\% - 3\text{ cm}^{-1} = 178\text{ cm}^{-1}$ is achieved for the MQW structure. This value is higher compared to our measured experimental result at a pumping power of $\sim 600\text{ kW/cm}^2$. This discrepancy could be explained by non-optimized material parameters of our ternary AlGaN material, affecting the recalculation of the carrier concentration at electrical injection to an optical pumping power. In regards to the design of the laser diode, increasing the MQW thickness, e.g. by increasing the number of quantum wells, and the fabrication of symmetric structures with matched upper and lower cladding layers could lead to a higher optical confinement factor and thus higher modal gain value.

For an AlGaN-based injection laser, a trade-off between the optical and electrical properties needs to be achieved. An increase of the Al content in the AlGaN waveguide layers would yield a larger refractive index contrast between the active region and the cladding layers. Consequently, the confinement factor and thus the modal gain is enhanced. However, the free carrier concentration decreases due to the effects related to the widening of the bandgap.[169, 170] In addition, AlGaN based deep UV laser diodes suffer from high acceptor activation energy of the p-AlGaN cladding layer. It needs to be sufficiently thin in order to decrease resistive losses.[103] This limitation has two crucial negative impacts: first, it shifts the maximum intensity of the optical mode away from the gain medium (MQW) due to the asymmetry of the waveguide design, and second, the mode penetrates into the p-GaN region, which increases the losses.[171]

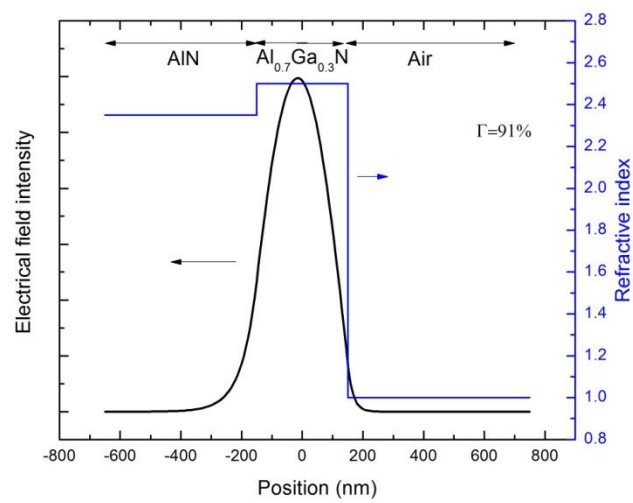


Figure 4.13. Spatial distribution of the simulated fundamental mode and the refractive index profile of the single AlGaN epitaxial layer.

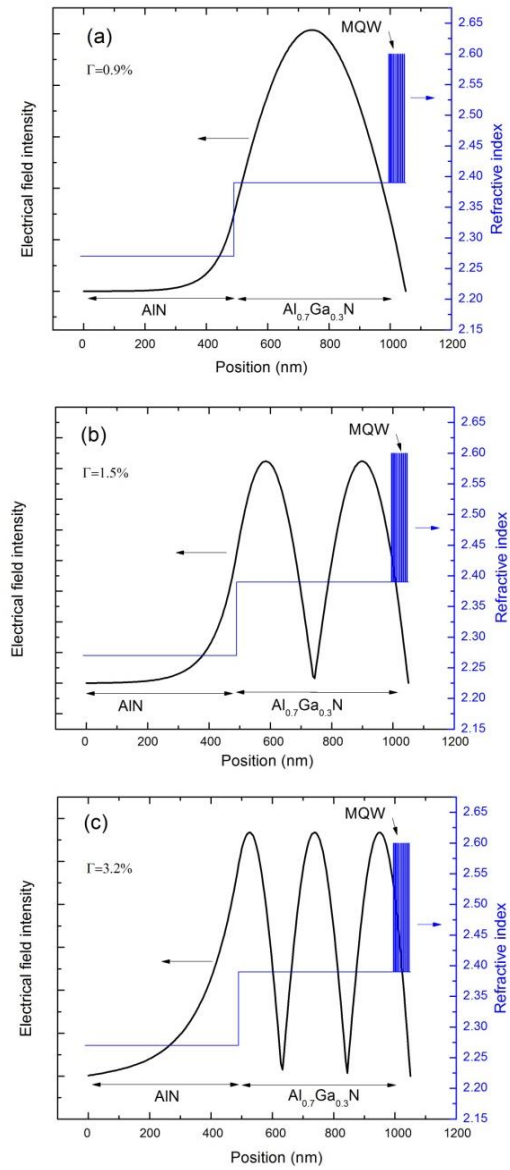


Figure 4.14. Spatial distribution of the simulated fundamental TE (a), second harmonic TE (b), and third harmonic TE mode within the MQW sample. The refractive index profile is given by the blue curve (right ordinate axis).

4.6 Conclusion

In summary, we have investigated the stimulated emission and gain properties of an AlGaN single epitaxial film, a double heterostructure, and a MQW structure grown on single crystalline AlN substrates emitting at a wavelength of 250 nm. Stimulated emission was achieved in all three samples as verified by the onset of a sharp emissions line located on the low energy side on top of a broad spontaneous emission peak. The observed stimulated emission was strongly TE-polarized. Threshold values of less than 700 kW/cm² for the single AlGaN layer, 250 kW/cm² for the DH structure, and 150 kW/cm² for the MQW structure were observed. The onset of stimulated emission was accompanied by a strong intensity enhancement of almost one order of magnitude and a more than ten-fold decrease of the FWHM of the emission peak (to less than 2 nm). The variable stripe length technique was applied to determine the net optical gain values of all three structures. The net optical gain increases as a function of the optical pumping power. The maximum gain values at a pumping power of 1 MW/cm² reaches 16 cm⁻¹, 58 cm⁻¹, and 48 cm⁻¹ in case of the single AlGaN epitaxial layer, the DH, and the MQW structure, respectively. A further increase of the pumping power causes higher modal gain values due to an increased population of excited states. A comparison of the measured results with numerical simulations demonstrated that the MQW structure and the DH structure provide higher material gain values compared to the single AlGaN epitaxial layer. They benefit from a strong charge carrier confinement due to larger overlap of electron and hole wave functions and an easier population inversion condition due to the abrupt increase of density of states at sub-band energy for quantum-confined structures. However, due to a small overlap of the optical mode

and the active region in the DH and MQW structure, the achieved modal gain values are reduced. In contrast, a high mode confinement characterized by a confinement factor of 91% is observed for the single AlGaN film due to an increased layer thickness. For the design of a laser diode structure, an optimization with regards to the optical confinement factor and the modal gain values is needed.

In all, the achieved stimulated emission and gain measurement results suggest an excellent optical quality and gain characteristics of the AlGaN-based structures grown on single crystalline AlN substrates. This proves the suitability for the demonstration of the first sub-280 nm injection lasers.

CHAPTER 5 Conclusions and future work

5.1 Conclusions

In this dissertation, optimization of light emission and propagation for AlGaN-based DUV emitters was investigated. Various techniques were demonstrated to be feasible for the realization of high efficiency, low threshold optoelectronic devices including LEDs and LDs.

High absorption coefficients in the DUV range of bulk AlN crystals and a small light extraction cone were identified to be responsible for the low external quantum efficiency of high Al content AlGaN-based LEDs grown on AlN substrates prepared by physical vapor transport. A KOH based wet etching technique was developed. High selectivity between the AlN and $\text{Al}_x\text{Ga}_{1-x}\text{N}$ (up to 13 times) as well as N-polar and III-polar (up to 300 times) was found to be critical for achieving effective substrate thinning or removal for AlGaN-based DUV LEDs. This KOH etching was further optimized and a smooth etching mechanism with reduced etching hillock size down to the wavelength scale was achieved by adding H_2O_2 into the KOH etchant. The effect of adding H_2O_2 was explained by the formation and dissolution of oxide/hydroxide on the III-nitride crystallographic planes, resulting in isotropic etching perpendicular to the sample surface.

The fabrication of nano-porous and nano-pillar structures on III-nitride substrates and $\text{Al}_{0.5}\text{Ga}_{0.5}\text{N}/\text{AlN}$ MQW structures with feature size as small as 100 nm via natural lithography was demonstrated for the first time. Nano-patterned structures revealed much lower integral reflectivity and enhanced photoluminescence intensity compared to as-grown

structures, demonstrating a large-scale and mass-producible pathway to higher light extraction efficiency in surface-patterned DUV LEDs. In addition, periodic III-nitride arrays with pitch size of 200 nm were fabricated. This is the smallest periodicity achieved on GaN and AlN thin films so far using interference lithography. Angle-resolved transmission measurement demonstrated diagonal intensity streaks on the pseudo-3D transmission graph as a function of both wavelength and collection angle. This was interpreted as a direct evidence of the existence of a photonic crystal.

Using single crystalline AlN substrates, sub-300 nm state-of-the-art AlGaN-based optically pumped DUV-LDs were achieved. A threshold of 84 kW/cm² and FWHM of less than 0.3 nm was demonstrated for the laser emission. The optical gain and polarization properties of AlGaN-based lasers were discussed. An exponential increase of the edge emission with dominant TE polarization demonstrated the onset of stimulated emission. In addition, the gain spectra and gain thresholds of a single AlGaN layer, an AlGaN double-heterostructure, and an AlGaN/AlGaN Multiple-Quantum-Well structure were investigated and compared. In the case of the single AlGaN epitaxial layer, no optical confinement was provided. Therefore, the found positive gain values demonstrated the excellent optical quality of our AlGaN epitaxial layers. Net modal gain values of 16 cm⁻¹, 58 cm⁻¹, and 48 cm⁻¹ were observed for a single AlGaN epitaxial layer, DH, and MQW structure, respectively, at a pumping power density of 1MW/cm². Furthermore, *Silvaco* simulation was applied in theoretical calculation of gain spectra and mode distribution, 5000 cm⁻¹ material gain coefficient can be achieved for MQW structure accompanied with a low (0.9%) optical

confinement factor due to a strongly asymmetric design of the cladding layers. These results provide guidance for further optimization of LD structures.

5.2 Future work

The understanding of light emission and propagation in AlGaN-based DUV LEDs and LDs allowed us to optimize the external quantum efficiency of LEDs and achieve lasing at 260 nm for LDs. However, further research targeting reasonably high EQE in DUV LEDs and electrically pumped DUV LDs is still necessary. The following tasks, which continue the research of this dissertation, are suggested:

- Strong evidence suggests that KOH/H₂O₂-based wet etching is a controllable and mild etching technique that provides large selectivity between AlN and AlGaN. As a continuation and ultimate proof of the positive effect of thinning via wet etching, the light extraction efficiency between an as-grown DUV-LED and a DUV-LED with substrate substantially thinned or removed must be compared.
- The effect of surface patterning needs to be compared. This includes a comprehensive comparison of random surface roughening, local periodic nanostructures and long range periodic nanostructures with various shapes, pitch size and feature height. Ongoing research is exploring the mechanism of light dispersion effect at rough surfaces and the limit of achievable light extraction enhancement. This should provide more information in finding a balance point of reaching satisfactory improvement of light extraction efficiency at a feasible fabrication cost.

- In regards to the AlGaN-based LD development, preliminary simulation results suggested a compromise between the optical and electrical properties needs to be made, which is essential in achieving a large modal gain and efficient carrier injection at the same time. Following the simulation results, various LD structures need to be fabricated with different cladding layer thickness and Al composition (especially p-AlGaN and p-GaN) to investigate the optimized laser structures and efficient carrier injection. In addition, due to the biaxial compressive strain of AlGaN epitaxial layers grown on AlN single crystalline substrates, the transition point of TE polarization to TM polarization is shifted to higher Al content (shorter wavelength) as collected from photoluminescence spectra (spontaneous emission). Further research on the polarization behavior of stimulated emission is underway and it should follow a similar trend as the spontaneous emission. This is very important in understanding the stimulated emission behavior of DUV-LD structures and realizing electrically pumped sub-280 nm laser diodes.

REFERENCES

- [1] R. Collazo, S. Mita, J. Xie, A. Rice, J. Tweedie, R. Dalmau, B. Moody, R. Schlesser, R. Kirste, A. Hoffmann, Z. Sitar, Ieee, 265 nm Light Emitting Diodes on AlN Single Crystal Substrates: Growth and Characterization, 2011.
- [2] C. Pernot, S. Fukahori, T. Inazu, T. Fujita, M. Kim, Y. Nagasawa, A. Hirano, M. Ippommatsu, M. Iwaya, S. Kamiyama, I. Akasaki, H. Amano, Development of high efficiency 255-355nm AlGaN-based light-emitting diodes, Phys. Status Solidi A-Appl. Mat., 208 (2011) 1594-1596.
- [3] M.M. Satter, H.-J. Kim, Z. Lochner, J.-H. Ryou, S.-C. Shen, R.D. Dupuis, P.D. Yoder, Design and Analysis of 250-nm AlInN Laser Diodes on AlN Substrates Using Tapered Electron Blocking Layers, Ieee Journal of Quantum Electronics, 48 (2012) 703-711.
- [4] M. Kneissl, Z.H. Yang, M. Teepe, C. Knollenberg, O. Schmidt, P. Kiesel, N.M. Johnson, S. Schujman, L.J. Schowalter, Ultraviolet semiconductor laser diodes on bulk AlN, Journal of Applied Physics, 101 (2007).
- [5] J.J. Freedman, T. Kubo, T. Egawa, Effect of AlN growth temperature on trap densities of in-situ metal-organic chemical vapor deposition grown AlN/AlGaN/GaN metal-insulator-semiconductor heterostructure field-effect transistors, Aip Advances, 2 (2012).
- [6] M.A. Khan, X. Hu, A. Tarakji, G. Simin, J. Yang, R. Gaska, M.S. Shur, AlGaN/GaN metal–oxide–semiconductor heterostructure field-effect transistors on SiC substrates, Applied Physics Letters, 77 (2000) 1339.
- [7] H. Miyake, T. Kimoto, J. Suda, Demonstration of Common-Emitter Operation in AlGaN/SiC Heterojunction Bipolar Transistors, Ieee Electron Device Letters, 31 (2010) 942-944.
- [8] S. Nakamura, M. Senoh, T. Mukai, HIGH-POWER INGAN/GAN DOUBLE-HETEROSTRUCTURE VIOLET LIGHT-EMITTING-DIODES, Applied Physics Letters, 62 (1993) 2390-2392.
- [9] S. Nakamura, M. Senoh, N. Iwasa, S. Nagahama, HIGH-POWER INGAN SINGLE-QUANTUM-WELL-STRUCTURE BLUE AND VIOLET LIGHT-EMITTING-DIODES, Applied Physics Letters, 67 (1995) 1868-1870.
- [10] S. Nakamura, M. Senoh, S. Nagahama, N. Iwasa, T. Yamada, T. Matsushita, H. Kiyoku, Y. Sugimoto, InGaN-based multi-quantum-well-structure laser diodes, Jpn J Appl Phys 2, 35 (1996) L74-L76.

- [11] C.P. Kuo, R.M. Fletcher, T.D. Osentowski, M.C. Lardizabal, M.G. Craford, V.M. Robbins, HIGH-PERFORMANCE ALGAINP VISIBLE LIGHT-EMITTING-DIODES, Applied Physics Letters, 57 (1990) 2937-2939.
- [12] M.R. Krames, O.B. Shchekin, R. Mueller-Mach, G.O. Mueller, L. Zhou, G. Harbers, M.G. Craford, Status and future of high-power light-emitting diodes for solid-state lighting, Journal of Display Technology, 3 (2007) 160-175.
- [13] M.R. Krames, M. Ochiai-Holcomb, G.E. Hofler, C. Carter-Coman, E.I. Chen, I.H. Tan, P. Grillot, N.F. Gardner, H.C. Chui, J.W. Huang, S.A. Stockman, F.A. Kish, M.G. Craford, T.S. Tan, C.P. Kocot, M. Hueschen, J. Posselt, B. Loh, G. Sasser, D. Collins, High-power truncated-inverted-pyramid $(Al_xGa_{1-x})(0.5)In_0.5P/GaP$ light-emitting diodes exhibiting > 50% external quantum efficiency, Applied Physics Letters, 75 (1999) 2365-2367.
- [14] I. Vurgaftman, J.R. Meyer, Band parameters for nitrogen-containing semiconductors, Journal of Applied Physics, 94 (2003) 3675-3696.
- [15] S.C. Jain, M. Willander, J. Narayan, R. Van Overstraeten, III-nitrides: Growth, characterization, and properties, Journal of Applied Physics, 87 (2000) 965-1006.
- [16] H. Morkoç, Handbook of Nitride Semiconductors and Devices, Materials Properties, Physics and Growth, John Wiley & Sons, 2009.
- [17] S. Nakamura, The roles of structural imperfections in InGaN-Based blue light-emitting diodes and laser diodes, Science, 281 (1998) 956-961.
- [18] J.R. Grandusky, S.R. Gibb, M.C. Mendrick, C. Moe, M. Wraback, L.J. Schowalter, High Output Power from 260nm Pseudomorphic Ultraviolet Light-Emitting Diodes with Improved Thermal Performance, Applied Physics Express, 4 (2011).
- [19] A. Rice, R. Collazo, J. Tweedie, R. Dalmau, S. Mita, J. Xie, Z. Sitar, Surface preparation and homoepitaxial deposition of AlN on (0001)-oriented AlN substrates by metalorganic chemical vapor deposition, Journal of Applied Physics, 108 (2010) 043510.
- [20] J.C. Rojo, L.J. Schowalter, R. Gaska, M. Shur, M.A. Khan, J. Yang, D.D. Koleske, Growth and characterization of epitaxial layers on aluminum nitride substrates prepared from bulk, single crystals, Journal of Crystal Growth, 240 (2002) 508-512.
- [21] J.R. Grandusky, J.A. Smart, M.C. Mendrick, L.J. Schowalter, K.X. Chen, E.F. Schubert, Pseudomorphic growth of thick n-type $Al_xGa_{1-x}N$ layers on low-defect-density bulk AlN substrates for UV LED applications, Journal of Crystal Growth, 311 (2009) 2864-2866.

- [22] R. Dalmau, B. Moody, R. Schlessler, S. Mita, J. Xie, M. Feneberg, B. Neuschl, K. Thonke, R. Collazo, A. Rice, J. Tweedie, Z. Sitar, Growth and Characterization of AlN and AlGaN Epitaxial Films on AlN Single Crystal Substrates, *Journal of The Electrochemical Society*, 158 (2011) H530-H535.
- [23] Z.G. Herro, D. Zhuang, R. Schlessler, Z. Sitar, Growth of AlN single crystalline boules, *Journal of Crystal Growth*, 312 (2010) 2519-2521.
- [24] P. Lu, R. Collazo, R.F. Dalmau, G. Durkaya, N. Dietz, B. Raghothamachar, M. Dudley, Z. Sitar, Seeded growth of AlN bulk crystals in m- and c-orientation, *Journal of Crystal Growth*, 312 (2009) 58-63.
- [25] T. Paskova, K.R. Evans, GaN Substrates-Progress, Status, and Prospects, *Ieee Journal of Selected Topics in Quantum Electronics*, 15 (2009) 1041-1052.
- [26] A. Koukitu, T. Taki, N. Takahashi, H. Seki, Thermodynamic study on the role of hydrogen during the MOVPE growth of group III nitrides, *Journal of Crystal Growth*, 197 (1999) 99-105.
- [27] A. Koukitu, Y. Kumagai, Thermodynamic analysis of group III nitrides grown by metal-organic vapour-phase epitaxy (MOVPE), hydride (or halide) vapour-phase epitaxy (HVPE) and molecular beam epitaxy (MBE), *Journal of Physics: Condensed Matter*, 13 (2001) 6907.
- [28] H. Amano, N. Sawaki, I. Akasaki, Y. Toyoda, Metalorganic vapor phase epitaxial growth of a high quality GaN film using an AlN buffer layer, *Applied Physics Letters*, 48 (1986) 353-355.
- [29] R.n. Collazo, S. Mita, J. Xie, A. Rice, J. Tweedie, R. Dalmau, Z. Sitar, Implementation of the GaN lateral polarity junction in a MESFET utilizing polar doping selectivity, *physica status solidi (a)*, 207 (2010) 45-48.
- [30] S. Mita, Polarity Control in GaN Epilayers Grown by Metalorganic Chemical Vapor Deposition, (2008).
- [31] A. Rice, R. Collazo, J. Tweedie, J. Xie, S. Mita, Z. Sitar, Linear dependency of Al-mole fraction with group-III precursor flows in $\text{Al}_x\text{Ga}_{1-x}\text{N}$ ($0 \leq x \leq 1$) deposition by LPOMVPE, *Journal of Crystal Growth*, 312 (2010) 1321-1324.
- [32] H. Morkoc, Progress and prospects of group-III nitride semiconductors, 1996.
- [33] P. Bhattacharya, Semiconductor optoelectronic devices, Prentice-Hall, Inc., 1994.

- [34] S. Nakamura, T. Mukai, M. Senoh, HIGH-POWER GAN P-N-JUNCTION BLUE-LIGHT-EMITTING DIODES, *Jpn J Appl Phys* 2, 30 (1991) L1998-L2001.
- [35] J.P. Zhang, A. Chitnis, V. Adivarahan, S. Wu, V. Mandavilli, R. Pachipulusu, M. Shatalov, G. Simin, J.W. Yang, M.A. Khan, Milliwatt power deep ultraviolet light-emitting diodes over sapphire with emission at 278 nm, *Applied Physics Letters*, 81 (2002) 4910-4912.
- [36] Y. Taniyasu, M. Kasu, T. Makimoto, An aluminium nitride light-emitting diode with a wavelength of 210 nanometres, *Nature*, 441 (2006) 325-328.
- [37] J. Edmond, A. Abare, M. Bergman, J. Bharathan, K.L. Bunker, D. Emerson, K. Haberern, J. Ibbetson, M. Leung, P. Russel, D. Slater, High efficiency GaN-based LEDs and lasers on SiC, *Journal of Crystal Growth*, 272 (2004) 242-250.
- [38] M. Shatalov, W.H. Sun, A. Lunev, X.H. Hu, A. Dobrinsky, Y. Bilenko, J.W. Yang, M. Shur, R. Gaska, C. Moe, G. Garrett, M. Wraback, AlGaN Deep-Ultraviolet Light-Emitting Diodes with External Quantum Efficiency above 10%, *Applied Physics Express*, 5 (2012).
- [39] H. Hirayama, Quaternary InAlGaN-based high-efficiency ultraviolet light-emitting diodes, *Journal of Applied Physics*, 97 (2005).
- [40] Y.P. Gong, K. Xing, T. Wang, Influence of high temperature AlN buffer on optical gain in AlGaN/AlGaN multiple quantum well structures, *Applied Physics Letters*, 99 (2011).
- [41] Z. Ren, Q. Sun, S.Y. Kwon, J. Han, K. Davitt, Y.K. Song, A.V. Nurmikko, H.K. Cho, W. Liu, J.A. Smart, L.J. Schowalter, Heteroepitaxy of AlGaN on bulk AlN substrates for deep ultraviolet light emitting diodes, *Applied Physics Letters*, 91 (2007) 051116.
- [42] T. Kinoshita, K. Hironaka, T. Obata, T. Nagashima, R. Dalmau, R. Schlessner, B. Moody, J.Q. Xie, S. Inoue, Y. Kumagai, A. Koukitu, Z. Sitar, Deep-Ultraviolet Light-Emitting Diodes Fabricated on AlN Substrates Prepared by Hydride Vapor Phase Epitaxy, *Applied Physics Express*, 5 (2012).
- [43] M. Kneissl, T. Kolbe, C. Chua, V. Kueller, N. Lobo, J. Stellmach, A. Knauer, H. Rodriguez, S. Einfeldt, Z. Yang, N.M. Johnson, M. Weyers, Advances in group III-nitride-based deep UV light-emitting diode technology, *Semiconductor Science and Technology*, 26 (2011).
- [44] U. Ozgur, G. Webb-Wood, H.O. Everitt, F. Yun, H. Morkoc, Systematic measurement of Al_xGa_{1-x}N refractive indices, *Applied Physics Letters*, 79 (2001) 4103-4105.

- [45] C. Huh, K.-S. Lee, E.-J. Kang, S.-J. Park, Improved light-output and electrical performance of InGaN-based light-emitting diode by microroughening of the p-GaN surface, Journal of Applied Physics, 93 (2003) 9383.
- [46] W.N. Carr, G.E. Pittman, ONE-WATT GaAs p-n JUNCTION INFRARED SOURCE, Applied Physics Letters, 3 (1963) 173.
- [47] A.I. Zhmakin, Enhancement of light extraction from light emitting diodes, Physics Reports, 498 (2011) 189-241.
- [48] Y. Li, C.P. Wong, Recent advances of conductive adhesives as a lead-free alternative in electronic packaging: Materials, processing, reliability and applications, Materials Science & Engineering R-Reports, 51 (2006) 1-35.
- [49] H. Sugawara, K. Itaya, H. Nozaki, G. Hatakoshi, HIGH-BRIGHTNESS INGAALP GREEN LIGHT-EMITTING-DIODES, Applied Physics Letters, 61 (1992) 1775-1777.
- [50] O. Shmatov, Z.S. Li, Truncated-inverted-pyramid light emitting diode geometry optimisation using ray tracing technique, Iee Proceedings-Optoelectronics, 150 (2003) 273-277.
- [51] C.C. Kao, H.C. Kuo, H.W. Huang, J.T. Chu, Y.C. Peng, Y.L. Hsieh, C.Y. Luo, S.C. Wang, C.C. Yu, C.F. Lin, Light-output enhancement in a nitride-based light-emitting diode with 22 degrees undercut sidewalls, Ieee Photonics Technology Letters, 17 (2005) 19-21.
- [52] T.X. Lee, K.F. Gao, W.T. Chien, C.C. Sun, Light extraction analysis of GaN-based light-emitting diodes with surface texture and/or patterned substrate, Optics Express, 15 (2007) 6670-6676.
- [53] B. Humphreys, M. Govett, ECR RIE-enhanced low pressure plasma etching of GaN/InGaN/AlGaN heterostructures, Mrs Internet Journal of Nitride Semiconductor Research, 1 (1996) U224-U232.
- [54] T. Fujii, Y. Gao, R. Sharma, E.L. Hu, S.P. DenBaars, S. Nakamura, Increase in the extraction efficiency of GaN-based light-emitting diodes via surface roughening, Applied Physics Letters, 84 (2004) 855.
- [55] T. Wang, X. Guo, Y. Fang, G.D. Shen, Roughening surface morphology on free-standing GaN membrane with laser lift-off technique, Chinese Science Bulletin, 52 (2007) 1001-1005.
- [56] E. Matioli, B. Fleury, E. Rangel, T. Melo, E. Hu, J. Speck, C. Weisbuch, High Extraction Efficiency GaN-Based Photonic-Crystal Light-Emitting Diodes: Comparison of

Extraction Lengths between Surface and Embedded Photonic Crystals, Applied Physics Express, 3 (2010) 032103.

- [57] J.J. Wierer, M.R. Krames, J.E. Epler, N.F. Gardner, M.G. Crawford, J.R. Wendt, J.A. Simmons, M.M. Sigalas, InGaN/GaN quantum-well heterostructure light-emitting diodes employing photonic crystal structures, Applied Physics Letters, 84 (2004) 3885.
- [58] A.A. Erchak, D.J. Ripin, S. Fan, P. Rakich, J.D. Joannopoulos, E.P. Ippen, G.S. Petrich, L.A. Kolodziejski, Enhanced coupling to vertical radiation using a two-dimensional photonic crystal in a semiconductor light-emitting diode, Applied Physics Letters, 78 (2001) 563.
- [59] K.-J. Byeon, S.-Y. Hwang, H. Lee, Fabrication of two-dimensional photonic crystal patterns on GaN-based light-emitting diodes using thermally curable monomer-based nanoimprint lithography, Applied Physics Letters, 91 (2007) 091106.
- [60] T. Nishida, H. Saito, N. Kobayashi, Efficient and high-power AlGaN-based ultraviolet light-emitting diode grown on bulk GaN, Applied Physics Letters, 79 (2001) 711.
- [61] C. Pernot, M. Kim, S. Fukahori, T. Inazu, T. Fujita, Y. Nagasawa, A. Hirano, M. Ippommatsu, M. Iwaya, S. Kamiyama, I. Akasaki, H. Amano, Improved Efficiency of 255-280 nm AlGaN-Based Light-Emitting Diodes, Applied Physics Express, 3 (2010).
- [62] M. Khizar, Z.Y. Fan, K.H. Kim, J.Y. Lin, H.X. Jiang, Nitride deep-ultraviolet light-emitting diodes with microlens array, Applied Physics Letters, 86 (2005).
- [63] T. Kinoshita, T. Obata, T. Nagashima, H. Yanagi, B. Moody, S. Mita, S. Inoue, Y. Kumagai, A. Koukitu, Z. Sitar, Performance and Reliability of Deep-Ultraviolet Light-Emitting Diodes Fabricated on AlN Substrates Prepared by Hydride Vapor Phase Epitaxy, Applied Physics Express, 6 (2013).
- [64] E. Francesco Pecora, W. Zhang, A. Yu. Nikiforov, L. Zhou, D.J. Smith, J. Yin, R. Paiella, L. Dal Negro, T.D. Moustakas, Sub-250 nm room-temperature optical gain from AlGaN/AlN multiple quantum wells with strong band-structure potential fluctuations, Applied Physics Letters, 100 (2012) 061111.
- [65] H. Yoshida, Y. Yamashita, M. Kuwabara, H. Kan, Demonstration of an ultraviolet 336 nm AlGaN multiple-quantum-well laser diode, Applied Physics Letters, 93 (2008).
- [66] R. Dingle, K.L. Shaklee, R.F. Leheny, Zetterst.Rb, STIMULATED EMISSION AND LASER ACTION IN GALLIUM NITRIDE, Applied Physics Letters, 19 (1971) 5-&.

- [67] S. Masui, Y. Matsuyama, T. Yanamoto, T. Kozaki, S. Nagahama, T. Mukai, 365 nm ultraviolet laser diodes composed of quaternary AlInGaN alloy, *Jpn J Appl Phys* 2, 42 (2003) L1318-L1320.
- [68] H. Tsuzuki, F. Mori, K. Takeda, T. Ichikawa, M. Iwaya, S. Kamiyama, H. Amano, I. Akasaki, H. Yoshida, M. Kuwabara, Y. Yamashita, H. Kan, High-performance UV emitter grown on high-crystalline-quality AlGaN underlying layer, *Phys. Status Solidi A-Appl. Mat.*, 206 (2009) 1199-1204.
- [69] S. Nakamura, UV/blue/green InGaN-based LEDs and laser diodes grown on epitaxially laterally overgrown GaN, *Ieice Transactions on Electronics*, E83C (2000) 529-535.
- [70] G.A. Garrett, P. Rotella, H. Shen, M. Wraback, T. Wunderer, C.L. Chua, Z. Yang, J.E. Northrup, N.M. Johnson, Sub-Threshold Time-Resolved Spectroscopy of Mid-UV AlGaN Laser Diode Structures Pseudomorphically Grown on Bulk AlN, in: *CLEO: Applications and Technology*, Optical Society of America, 2012, pp. JTh1L. 5.
- [71] T. Wunderer, C.L. Chua, Z. Yang, J.E. Northrup, N.M. Johnson, G.A. Garrett, H. Shen, M. Wraback, Pseudomorphically Grown Ultraviolet C Photopumped Lasers on Bulk AlN Substrates, *Applied Physics Express*, 4 (2011) 092101.
- [72] J. Xie, S. Mita, Z. Bryan, W. Guo, L. Hussey, B. Moody, R. Schlessner, R. Kirste, M. Gerhold, R.n. Collazo, Z. Sitar, Lasing and longitudinal cavity modes in photo-pumped deep ultraviolet AlGaN heterostructures, *Applied Physics Letters*, 102 (2013) 171102.
- [73] M. Feneberg, B. Neuschl, K. Thonke, R. Collazo, A. Rice, Z. Sitar, R. Dalmau, J.Q. Xie, S. Mita, R. Goldhahn, Sharp bound and free exciton lines from homoepitaxial AlN, *Phys. Status Solidi A-Appl. Mat.*, 208 (2011) 1520-1522.
- [74] T. Wunderer, C.L. Chua, J.E. Northrup, Z. Yang, N.M. Johnson, M. Kneissl, G.A. Garrett, H. Shen, M. Wraback, B. Moody, H.S. Craft, R. Schlessner, R.F. Dalmau, Z. Sitar, Optically pumped UV lasers grown on bulk AlN substrates, in: P.J. Parbrook, R.W. Martin, M.P. Halsall (Eds.) *Physica Status Solidi C: Current Topics in Solid State Physics*, Vol 9, No 3-4, Wiley-VCH Verlag GmbH, Weinheim, 2012, pp. 822-825.
- [75] B. Coppa, Bigger Sapphire Wafers to Make LED Lighting More Affordable, in, Examiner.com, 2012.
- [76] R. Collazo, J. Xie, B.E. Gaddy, Z. Bryan, R. Kirste, M. Hoffmann, R. Dalmau, B. Moody, Y. Kumagai, T. Nagashima, Y. Kubota, T. Kinoshita, A. Koukitu, D.L. Irving, Z. Sitar, On the origin of the 265 nm absorption band in AlN bulk crystals, *Applied Physics Letters*, 100 (2012).

- [77] W.S. Wong, T. Sands, N.W. Cheung, M. Kneissl, D.P. Bour, P. Mei, L.T. Romano, N.M. Johnson, Fabrication of thin-film InGaN light-emitting diode membranes by laser lift-off, *Applied Physics Letters*, 75 (1999) 1360.
- [78] A. Szczeńny, P. Śniecikowski, J. Szmidt, A. Werbowy, Reactive ion etching of novel materials—GaN and SiC, *Vacuum*, 70 (2003) 249-254.
- [79] I. Adesida, C. Youtsey, A.T. Ping, F. Khan, L.T. Romano, G. Bulman, Dry and wet etching for group III-nitrides, *Mrs Internet Journal of Nitride Semiconductor Research*, 4 (1999).
- [80] D. Zhuang, J.H. Edgar, Wet etching of GaN, AlN, and SiC: a review, *Materials Science and Engineering: R: Reports*, 48 (2005) 1-46.
- [81] D. Zhuang, J.H. Edgar, L.H. Liu, B. Liu, L. Walker, Wet chemical etching of AlN single crystals, *Mrs Internet Journal of Nitride Semiconductor Research*, 7 (2002).
- [82] J.A. Grenko, C.L. Reynolds, R. Schlesser, K. Bachmann, Z. Rietmeier, R.F. Davis, Z. Sitar, Selective etching of GaN from AlGaN/GaN and AlN/GaN structures, *Mrs Internet Journal of Nitride Semiconductor Research*, 9 (2004).
- [83] J.L. Weyher, P.D. Brown, J.L. Rouviere, T. Wosinski, A.R.A. Zauner, I. Grzegory, Recent advances in defect-selective etching of GaN, *Journal of Crystal Growth*, 210 (2000) 151-156.
- [84] P. Visconti, D. Huang, F. Yun, M.A. Reschchikov, T. King, R. Cingolani, J. Jasinski, Z. Liliental-Weber, H. Morkoc, Rapid delineation of extended defects in GaN and a novel method for their reduction, *Physica Status Solidi a-Applied Research*, 190 (2002) 5-14.
- [85] J.L. Weyher, L. Macht, G. Kamler, J. Borysiuk, I. Grzegory, Characterization of GaN single crystals by defect-selective etching, *physica status solidi (c)*, 0 (2003) 821-826.
- [86] T. Palacios, F. Calle, M. Varela, C. Ballesteros, E. Monroy, F.B. Naranjo, M.A. Sanchez-Garcia, E. Calleja, E. Munoz, Wet etching of GaN grown by molecular beam epitaxy on Si(111), *Semiconductor Science and Technology*, 15 (2000) 996-1000.
- [87] D. Kapolnek, X.H. Wu, B. Heying, S. Keller, B.P. Keller, U.K. Mishra, S.P. DenBaars, J.S. Speck, Structural evolution in epitaxial metalorganic chemical vapor deposition grown GaN films on sapphire, *Applied Physics Letters*, 67 (1995) 1541.
- [88] D. Zhuang, J.H. Edgar, B. Strojek, J. Chaudhuri, Z. Rek, Defect-selective etching of bulk AlN single crystals in molten KOH/NaOH eutectic alloy, *Journal of Crystal Growth*, 262 (2004) 89-94.

- [89] Y. Morimoto, FEW CHARACTERISTICS OF EPITAXIAL GAN - ETCHING AND THERMAL-DECOMPOSITION, Journal of The Electrochemical Society, 121 (1974) 1383-1384.
- [90] K.R. Bray, W. Zhao, L. Kordas, R. Wise, M. Robinson, G. Rozgonyi, Electrical, structural, and chemical analysis of defects in epitaxial SiGe-based heterostructures, Journal of The Electrochemical Society, 152 (2005) C310-C315.
- [91] T. Paskova, E.A. Preble, A.D. Hanser, K.R. Evans, R. Kroeger, P.P. Paskov, A.J. Cheng, M. Park, J.A. Grenko, M.A.L. Johnson, Polar and nonpolar HVPE GaN substrates: impact of doping on the structural, electrical and optical characteristics, in: R. Butte (Ed.) Physica Status Solidi C: Current Topics in Solid State Physics, Vol 6, Suppl 2, 2009, pp. S344-S347.
- [92] R. Kirste, S. Mita, L. Hussey, M.P. Hoffmann, W. Guo, I. Bryan, Z. Bryan, J. Tweedie, J. Xie, M. Gerhold, R.n. Collazo, Z. Sitar, Polarity control and growth of lateral polarity structures in AlN, Applied Physics Letters, 102 (2013) 181913.
- [93] R. Kirste, S. Mita, M.P. Hoffmann, L. Hussey, W. Guo, I. Bryan, Z. Bryan, J. Tweedie, M. Gerhold, A. Hoffmann, Properties of AlN based lateral polarity structures, physica status solidi (c), (2014).
- [94] D.S. Li, M. Sumiya, S. Fuke, D.R. Yang, D.L. Que, Y. Suzuki, Y. Fukuda, Selective etching of GaN polar surface in potassium hydroxide solution studied by x-ray photoelectron spectroscopy, Journal of Applied Physics, 90 (2001) 4219-4223.
- [95] H.M. Ng, N.G. Weimann, A. Chowdhury, GaN nanotip pyramids formed by anisotropic etching, Journal of Applied Physics, 94 (2003) 650-653.
- [96] E.A. Moon, J.L. Lee, H.M. Yoo, Selective wet etching of GaAs on Al_xGa_{1-x}As for AlGaAs/InGaAs/AlGaAs pseudomorphic high electron mobility transistor, Journal of Applied Physics, 84 (1998) 3933-3938.
- [97] R.A. Logan, F.K. Reinhart, OPTICAL WAVEGUIDES IN GAAS-AIGAAS EPITAXIAL LAYERS, Journal of Applied Physics, 44 (1973) 4172-4176.
- [98] B. Wu, M. Zinkevich, F. Aldinger, W. Zhang, Ab initio structural and energetic study of (, Ga) perovskites, Journal of Physics and Chemistry of Solids, 68 (2007) 570-575.
- [99] R. Dalmau, R. Collazo, S. Mita, Z. Sitar, X-Ray Photoelectron Spectroscopy Characterization of Aluminum Nitride Surface Oxides: Thermal and Hydrothermal Evolution, Journal of Electronic Materials, 36 (2007) 414-419.

- [100] D.A. Stocker, E.F. Schubert, J.M. Redwing, Crystallographic wet chemical etching of GaN, *Applied Physics Letters*, 73 (1998) 2654.
- [101] M. Bickermann, S. Schmidt, B.M. Epelbaum, P. Heimann, S. Nagata, A. Winnacker, Wet KOH etching of freestanding AlN single crystals, *Journal of Crystal Growth*, 300 (2007) 299-307.
- [102] T. Tsuchida, H. Takahashi, X-RAY PHOTOELECTRON SPECTROSCOPIC STUDY OF HYDRATED ALUMINAS AND ALUMINAS, *Journal of Materials Research*, 9 (1994) 2919-2924.
- [103] H. Hirayama, S. Fujikawa, N. Noguchi, J. Norimatsu, T. Takano, K. Tsubaki, N. Kamata, 222-282 nm AlGaN and InAlGaN-based deep-UV LEDs fabricated on high-quality AlN on sapphire, *Phys. Status Solidi A-Appl. Mat.*, 206 (2009) 1176-1182.
- [104] H. Hirayama, Advances of AlGaN-based High-Efficiency Deep-UV LEDs, *Optoelectronic Materials and Devices V*, 7987 (2011).
- [105] T.N. Oder, J. Shakya, J.Y. Lin, H.X. Jiang, III-nitride photonic crystals, *Applied Physics Letters*, 83 (2003) 1231.
- [106] Y.D. Wang, S.J. Chua, M.S. Sander, P. Chen, S. Tripathy, C.G. Fonstad, Fabrication and properties of nanoporous GaN films, *Applied Physics Letters*, 85 (2004) 816.
- [107] C.-H. Hou, S.-Z. Tseng, C.-H. Chan, T.-J. Chen, H.-T. Chien, F.-L. Hsiao, H.-K. Chiu, C.-C. Lee, Y.-L. Tsai, C.-C. Chen, Output power enhancement of light-emitting diodes via two-dimensional hole arrays generated by a monolayer of microspheres, *Applied Physics Letters*, 95 (2009) 133105.
- [108] C.-F. Lai, C.-H. Chao, H.-C. Kuo, H.-H. Yen, C.-E. Lee, W.-Y. Yeh, Directional light extraction enhancement from GaN-based film-transferred photonic crystal light-emitting diodes, *Applied Physics Letters*, 94 (2009).
- [109] U.C. Fischer, H.P. Zingsheim, SUB-MICROSCOPIC PATTERN REPLICATION WITH VISIBLE-LIGHT, *Journal of Vacuum Science & Technology*, 19 (1981) 881-885.
- [110] B.J. Kim, H. Jung, S.H. Kim, J. Bang, J. Kim, GaN-Based Light-Emitting Diode With Three-Dimensional Silver Reflectors, *Ieee Photonics Technology Letters*, 21 (2009) 700-702.
- [111] S. Wong, V. Kitaev, G.A. Ozin, Colloidal crystal films: Advances in universality and perfection, *Journal of the American Chemical Society*, 125 (2003) 15589-15598.

- [112] W.Y. Ji, I.S. Jae, M.A. Ho, G.K. Tae, Fabrication of Nanometer-scale Pillar Structures by Using Nanosphere Lithography, *Journal of the Korean Physical Society*, 58 (2011) 994.
- [113] H. Masuda, K. Fukuda, ORDERED METAL NANOHOLE ARRAYS MADE BY A 2-STEP REPLICATION OF HONEYCOMB STRUCTURES OF ANODIC ALUMINA, *Science*, 268 (1995) 1466-1468.
- [114] H. Masuda, F. Hasegwa, S. Ono, Self-ordering of cell arrangement of anodic porous alumina formed in sulfuric acid solution, *Journal of The Electrochemical Society*, 144 (1997) L127-L130.
- [115] T. Dai, B. Zhang, X.N. Kang, K. Bao, W.Z. Zhao, D.S. Xu, G.Y. Zhang, Z.Z. Gan, Light Extraction Improvement From GaN-Based Light-Emitting Diodes With Nano-Patterned Surface Using Anodic Aluminum Oxide Template, *Ieee Photonics Technology Letters*, 20 (2008) 1974-1976.
- [116] W.Y. Fu, K.K.-Y. Wong, H.W. Choi, Room temperature photonic crystal band-edge lasing from nanopillar array on GaN patterned by nanosphere lithography, *Journal of Applied Physics*, 107 (2010) 063104.
- [117] M.A. Tsai, P.C. Yu, C.H. Chiu, H.C. Kuo, T.C. Lu, S.H. Lin, Self-Assembled Two-Dimensional Surface Structures for Beam Shaping of GaN-Based Vertical-Injection Light-Emitting Diodes, *Ieee Photonics Technology Letters*, 22 (2010) 12-14.
- [118] K.H. Li, H.W. Choi, InGaN light-emitting diodes with indium-tin-oxide photonic crystal current-spreading layer, *Journal of Applied Physics*, 110 (2011) 053104.
- [119] J. Liang, H. Chik, A. Yin, J. Xu, Two-dimensional lateral superlattices of nanostructures: Nonlithographic formation by anodic membrane template, *Journal of Applied Physics*, 91 (2002) 2544.
- [120] X.X. Fu, B. Zhang, X.N. Kang, J.J. Deng, C. Xiong, T. Dai, X.Z. Jiang, T.J. Yu, Z.Z. Chen, G.Y. Zhang, GaN-based light-emitting diodes with photonic crystals structures fabricated by porous anodic alumina template, *Optics Express*, 19 (2011) A1104-A1108.
- [121] D. Pudiš, L. Šušlik, J. Škriniarová, J. Kováč, I. Martinček, Š. Haščík, I. Kubicová, J. Novák, M. Veselý, Light extraction from a light emitting diode with photonic structure in the surface layer investigated by NSOM, *Optics & Laser Technology*, 43 (2011) 917-921.
- [122] L. Wu, W.Y.Y. Tong, K.S. Wong, J. Hua, M. HaeuBler, B.Z. Tang, Holographic nano-patterning based on photo-cross-linkable light emitting polyacetylenes, in: W. Jantsch, F. Schaffler (Eds.) *Physics of Semiconductors*, Pts A and B, 2007, pp. 367-368.

- [123] T.H. Seo, T.S. Oh, Y.S. Lee, H. Jeong, J.D. Kim, H. Kim, A.H. Park, K.J. Lee, C.-H. Hong, E.-K. Suh, Enhanced Light Extraction in GaN-Based Light-Emitting Diodes with Holographically Fabricated Concave Hemisphere-Shaped Patterning on Indium–Tin–Oxide Layer, *Japanese Journal of Applied Physics*, 49 (2010) 092101.
- [124] M.D.B. Charlton, M.E. Zoorob, T. Lee, Photonic quasi-crystal LEDs: design, modelling, and optimisation, 6486 (2007) 64860R-64860R-64810.
- [125] T.N. Oder, K.H. Kim, J.Y. Lin, H.X. Jiang, III-nitride blue and ultraviolet photonic crystal light emitting diodes, *Applied Physics Letters*, 84 (2004) 466.
- [126] H.Y. Ryu, J.I. Shim, Structural Parameter Dependence of Light Extraction Efficiency in Photonic Crystal InGaN Vertical Light-Emitting Diode Structures, *Ieee Journal of Quantum Electronics*, 46 (2010) 714-720.
- [127] Y.-J. Lee, S.-H. Kim, J. Huh, G.-H. Kim, Y.-H. Lee, S.-H. Cho, Y.-C. Kim, Y.R. Do, A high-extraction-efficiency nanopatterned organic light-emitting diode, *Applied Physics Letters*, 82 (2003) 3779.
- [128] M. Rattier, H. Benisty, R.P. Stanley, J.F. Carlin, R. Houdre, U. Oesterle, C.J.M. Smith, C. Weisbuch, T.F. Krauss, Toward Ultrahigh-Efficiency aluminum oxide microcavity light-emitting diodes: Guided mode extraction by photonic crystals, *Ieee Journal of Selected Topics in Quantum Electronics*, 8 (2002) 238-247.
- [129] D. Gao, Z. Zhou, Nonlinear equation method for band structure calculations of photonic crystal slabs, *Applied Physics Letters*, 88 (2006) 163105.
- [130] C. Wiesmann, K. Bergeneck, N. Linder, U.T. Schwarz, Analysis of the emission characteristics of photonic crystal LEDs, 6989 (2008) 69890L-69890L-69899.
- [131] R. Collazo, S. Mita, A. Aleksov, R. Schlessner, Z. Sitar, Growth of Ga- and N- polar gallium nitride layers by metalorganic vapor phase epitaxy on sapphire wafers, *Journal of Crystal Growth*, 287 (2006) 586-590.
- [132] L.-C. Chen, C.-K. Wang, J.-B. Huang, L.-S. Hong, A nanoporous AlN layer patterned by anodic aluminum oxide and its application as a buffer layer in a GaN-based light-emitting diode, *Nanotechnology*, 20 (2009) 085303.
- [133] C.B. Soh, W. Liu, A.M. Yong, S.J. Chua, S.Y. Chow, S. Tripathy, R.J.N. Tan, Phosphor-Free Apple-White LEDs with Embedded Indium-Rich Nanostructures Grown on Strain Relaxed Nano-epitaxy GaN, *Nanoscale Research Letters*, 5 (2010) 1788-1794.

- [134] M.E. Walsh, Nanostructuring magnetic thin films using interference lithography, in, Massachusetts Institute of Technology, 2000.
- [135] K. Leinartas, P. Miecienskas, A. Selskis, E. Juzeliunas, Nanoporous alumina formation in a thin magnetron-sputtered Al layer, *Chemija*, 21 (2010) 1-6.
- [136] S. Ono, M. Saito, M. Ishiguro, H. Asoh, Controlling Factor of Self-Ordering of Anodic Porous Alumina, *Journal of The Electrochemical Society*, 151 (2004) B473.
- [137] K.C. Park, H.J. Choi, C.H. Chang, R.E. Cohen, G.H. McKinley, G. Barbastathis, Nanotextured Silica Surfaces with Robust Superhydrophobicity and Omnidirectional Broadband Supertransmissivity, *Acs Nano*, 6 (2012) 3789-3799.
- [138] S. Chattopadhyay, Y.F. Huang, Y.J. Jen, A. Ganguly, K.H. Chen, L.C. Chen, Anti-reflecting and photonic nanostructures, *Materials Science & Engineering R-Reports*, 69 (2010) 1-35.
- [139] J.M. Park, Z.Q. Gan, W.Y. Leung, R. Liu, Z. Ye, K. Constant, J. Shinar, R. Shinar, K.M. Ho, Soft holographic interference lithography microlens for enhanced organic light emitting diode light extraction, *Optics Express*, 19 (2011) A786-A792.
- [140] J.S. Yu, Y.M. Song, J.W. Leem, Y.T. Lee, Subwavelength antireflection structures and their device applications, (2010) 760812-760812-760818.
- [141] C. Wiesmann, K. Bergeneck, N. Linder, U.T. Schwarz, Photonic crystal LEDs - designing light extraction, *Laser & Photonics Review*, 3 (2009) 262-286.
- [142] S. Keller, C. Schaake, N.A. Fichtenbaum, C.J. Neufeld, Y. Wu, K. McGroddy, A. David, S.P. DenBaars, C. Weisbuch, J.S. Speck, U.K. Mishra, Optical and structural properties of GaN nanopillar and nanostripe arrays with embedded InGaN/GaN multi-quantum wells, *Journal of Applied Physics*, 100 (2006).
- [143] L. Ondic, K. Kusova, O. Cibulka, I. Pelant, K. Dohnalova, B. Rezek, O. Babchenko, A. Kromka, N. Ganesh, Enhanced photoluminescence extraction efficiency from a diamond photonic crystal via leaky modes, *New Journal of Physics*, 13 (2011).
- [144] D.H. Long, H.-A. Do, J. Park, I.-K. Hwang, S.-W. Ryu, J.-K. Lee, Enhancement of light extraction efficiency of light-emitting diode with hexagonal photonic crystal layer, 6645 (2007) 66450G-66450G-66458.
- [145] Z. Yang, T. Yu, S. Mu, Z. Chen, G. Zhang, A precise ray tracing simulation model for GaN based light emitting diodes, *physica status solidi (c)*, 7 (2010) 2193-2195.

- [146] S.J. Lee, Study of photon extraction efficiency in InGaN light-emitting diodes depending on chip structures and chip-mount schemes, *Optical Engineering*, 45 (2006).
- [147] I. Buss, M. Cryan, G. Nash, M. Haigh, I. Craddock, C. Railton, J. Rarity, 3D modelling of enhanced surface emission using surface roughening, 2006.
- [148] W. Choi, Q. Park, D. Kim, H. Jeon, C. Sone, Y. Park, FDTD simulation for light extraction in a GaN-based LED, *Journal of the Korean Physical Society*, 49 (2006) 877-880.
- [149] J.Q. Xie, S. Mita, Z. Bryan, W. Guo, L. Hussey, B. Moody, R. Schlessler, R. Kirste, M. Gerhold, R. Collazo, Z. Sitar, Lasing and longitudinal cavity modes in photo-pumped deep ultraviolet AlGaN heterostructures, *Applied Physics Letters*, 102 (2013).
- [150] A.A. Belyanin, J. Zhang, H. Zhao, N. Tansu, P.M. Smowton, Gain characteristics of deep UV AlGaN quantum wells lasers, 7953 (2011) 79530H-79530H-79539.
- [151] L.D. Negro, P. Bettotti, M. Cazzanelli, D. Pacifici, L. Pavesi, Applicability conditions and experimental analysis of the variable stripe length method for gain measurements, *Optics Communications*, 229 (2004) 337-348.
- [152] S.L. Chuang, Optical gain of strained wurtzite GaN quantum-well lasers, *Ieee Journal of Quantum Electronics*, 32 (1996) 1791-1800.
- [153] W.W. Chow, A. Knorr, S.W. Koch, THEORY OF LASER GAIN IN GROUP-III NITRIDES, *Applied Physics Letters*, 67 (1995) 754-756.
- [154] J. Mickevicius, J. Jurkevicius, K. Kazlauskas, A. Zukauskas, G. Tamulaitis, M.S. Shur, M. Shatalov, J. Yang, R. Gaska, Stimulated emission in AlGaN/AlGaN quantum wells with different Al content, *Applied Physics Letters*, 100 (2012).
- [155] T.J. Schmidt, Y.-H. Cho, J.J. Song, W. Yang, Room-temperature deep-ultraviolet-stimulated emission from Al_xGa_{1-x}N thin films grown on sapphire, *Applied Physics Letters*, 74 (1999) 245.
- [156] D. Wiesmann, I. Brener, L. Pfeiffer, M.A. Khan, C. Sun, Gain spectra and stimulated emission in epitaxial (In, Al) GaN thin films, *Applied Physics Letters*, 69 (1996) 3384-3386.
- [157] K.L. Shaklee, Direct Determination of Optical Gain in Semiconductor Crystals, *Applied Physics Letters*, 18 (1971) 475.
- [158] L. Dal Negro, M. Cazzanelli, N. Daldosso, Z. Gaburro, L. Pavesi, F. Priolo, D. Pacifici, G. Franzò, F. Iacona, Stimulated emission in plasma-enhanced chemical vapour deposited

silicon nanocrystals, *Physica E: Low-dimensional Systems and Nanostructures*, 16 (2003) 297-308.

[159] C.C. Liao, S.W. Feng, C.C. Yang, Y.S. Lin, K.J. Ma, C.C. Chuo, C.M. Lee, J.I. Chyi, Stimulated emission study of InGaN/GaN multiple quantum well structures, *Applied Physics Letters*, 76 (2000) 318-320.

[160] K.B. Nam, J. Li, M.L. Nakarmi, J.Y. Lin, H.X. Jiang, Unique optical properties of AlGaN alloys and related ultraviolet emitters, *Applied Physics Letters*, 84 (2004) 5264.

[161] A.A. Yamaguchi, Theoretical investigation of optical polarization properties in Al-rich AlGaN quantum wells with various substrate orientations, *Applied Physics Letters*, 96 (2010).

[162] L. Cláudio de Carvalho, A. Schleife, F. Fuchs, F. Bechstedt, Valence-band splittings in cubic and hexagonal AlN, GaN, and InN, *Applied Physics Letters*, 97 (2010) 232101.

[163] I. Vurgaftman, J.R. Meyer, L.R. Ram-Mohan, Band parameters for III-V compound semiconductors and their alloys, *Journal of Applied Physics*, 89 (2001) 5815.

[164] J. Zhang, H.P. Zhao, N. Tansu, Effect of crystal-field split-off hole and heavy-hole bands crossover on gain characteristics of high Al-content AlGaN quantum well lasers, *Applied Physics Letters*, 97 (2010).

[165] A.A. Yamaguchi, Valence band engineering for remarkable enhancement of surface emission in AlGaN deep-ultraviolet light emitting diodes, in: T. Palacios, D. Jena (Eds.) *Physica Status Solidi C - Current Topics in Solid State Physics*, Vol 5, No 6, 2008, pp. 2364-2366.

[166] S.-H. Park, J.-I. Shim, Carrier density dependence of polarization switching characteristics of light emission in deep-ultraviolet AlGaN/AlN quantum well structures, *Applied Physics Letters*, 102 (2013) 221109.

[167] Q. Dai, M.F. Schubert, M.-H. Kim, J.K. Kim, E. Schubert, D.D. Koleske, M.H. Crawford, S.R. Lee, A.J. Fischer, G. Thaler, Internal quantum efficiency and nonradiative recombination coefficient of GaInN/GaN multiple quantum wells with different dislocation densities, *Applied Physics Letters*, 94 (2009) 111109.

[168] G. Fuchs, J. Horer, A. Hangleiter, V. Harle, F. Scholz, R.W. Glew, L. Goldstein, INTERVALENCE BAND ABSORPTION IN STRAINED AND UNSTRAINED INGAAS MULTIPLE QUANTUM-WELL STRUCTURES, *Applied Physics Letters*, 60 (1992) 231-233.

- [169] Y.C. Yeo, T.C. Chong, M.F. Li, W.J. Fan, Analysis of optical gain and threshold current density of wurtzite InGaN/GaN/AlGaN quantum well lasers, *Journal of Applied Physics*, 84 (1998) 1813-1819.
- [170] L.Q. Zhang, D.S. Jiang, J.J. Zhu, D.G. Zhao, Z.S. Liu, S.M. Zhang, H. Yang, Confinement factor and absorption loss of AlInGaN based laser diodes emitting from ultraviolet to green, *Journal of Applied Physics*, 105 (2009).
- [171] G. Muziol, H. Turski, M. Siekacz, M. Sawicka, P. Wolny, P. Perlin, C. Skierbiszewski, Determination of gain in AlGaN cladding free nitride laser diodes, *Applied Physics Letters*, 103 (2013).

APPENDIX

Appendix A: Matlab script for optical gain analysis

```
%Gain Analysis

clc;
clear all;
close all;

%input folder location
%file=input('Enter input folder name:','s');
file=uigetdir('', 'Find a folder with stuff in it!');
if isempty(file)
    error('No folder specified');
end
bg=input(sprintf('Enter background intensity level.\n(default=750)\n'));
if isempty(bg)
    bg=750;
end
feedback=input(sprintf('Feedback Type:\n1: See all plots and fits
individually\n2: See all plots and fits in sets of 10\n3: Only see final
gain curve and r^2 histogram.\n(default=2)\n'));
if isempty(feedback)
    feedback=2;
end
rsqCut=input(sprintf('Enter minimum r^2 value. (poorly fitting plots get
thrown out)\n(default=0.95)\n'));
if isempty(rsqCut)
    rsqCut=.95;
end
ngain=input(sprintf('Remove datapoints with negative gain?\n1: Remove
negative gain\n2: Keep negative gain\n(default=2)\n'));
if isempty(ngain)
    ngain=2;
end

%getting the data for the current directory
dirData = dir(file);
%finding the index for directories
dirIndex = [dirData.isdir];
%getting a list of the files
fileList = {dirData(~dirIndex).name}';

fname=char(fileList(1));
lengthname=fname(1:length(fname)-4);
infile=strcat(file,'/',fname);
w=csvread(infile);
wavelength=w(:,1);

%generating outfile matrix
outfile1=zeros(length(wavelength),length(fileList)+1);
outfile1(:,1)=wavelength;
```

```

%writing to outfile matrix
for i=1:length(fileList)
    fname=char(fileList(i));
    lengthname=fname(1:length(fname)-4);
    infile=strcmp(infile,'/',fname);
    lgth(i)=str2num(lengthname);
    w=csvread(infile);
    for k=1:length(wavelength)
        outfile1(k,i+1)=w(k,2);
    end
end

K=1;
for j=1:length(wavelength)
    if min(outfile1(j,2:end)>bg)==0
    else
        newoutfile1(K,:)=outfile1(j,1:end);
        newwavelength(K)=wavelength(j);
        K=K+1;
    end
end

%This loop finds the row of the maximum index so it can be retrieved and
shown
maxIndex=1;
for j=1:length(newwavelength)
    if max(newoutfile1(j,2:end))>max(newoutfile1(maxIndex,2:end))
        maxIndex=j;
    end
end
figure(1);
fig=figure(1);
set (fig, 'Units', 'normalized', 'Position', [0.1,0.1,.8,.8]);
plot(lgth,newoutfile1(maxIndex,2:end),'o');
title(sprintf('This plot is of the curve with the maximum intensity for
the dataset.\nChoose bounds to avoid saturated regions.'));
xlabel('Stripe Length (um)');
ylabel('Intensity (arb)');
xlim([min(lgth)-50 max(lgth)+50]);

lower=input(sprintf('Enter lower bound (Stripe length
(um)).\n(default=min(length))\n'));
if isempty(lower)
    lower=min(lgth);
end
upper=input(sprintf('Enter upper bound (Stripe Length
(um)).\n(default=max(length))\n'));
if isempty(upper)
    upper=max(lgth);
end

```

```

%these two lines take out the values beyond the lower and upper limits
newlgth=lgth(find(lgth>=lower&lgth<=upper));
newnewoutfile1=newoutfile1(:,[1,find(lgth>=lower&lgth<=upper)+1]);

%fitting to gain function
for j=1:length(newwavelength)
    gainfunction=@(p,x) (p(1)./p(2).*exp(p(2)*x)-1));
    guess=[0.45 0.0025];
    coefEsts=nlinfit(newlgth,newnewoutfile1(j,2:end)-
bg,gainfunction,guess);
    G(j)=coefEsts(2);
    rsqs(j)=1-(sum((newnewoutfile1(j,2:end)-
(gainfunction(coefEsts,newlgth)+bg)).^2))/((length(newnewoutfile1(j,2:end)-
1)*var(newoutfile1(j,2:end))));

    if feedback~=3
        if feedback==1
            figure(j+2);
            fig=figure(j);
            set (fig, 'Units', 'normalized', 'Position', [0.1,0.1,.8,.8]);
        end
        if feedback==2
            figure(ceil(j/10+2));
            subplot(2,5,mod(j+9,10)+1);
            fig=figure(ceil(j/10+2));
            set (fig, 'Units', 'normalized', 'Position', [0.1,0.1,.8,.8]);
        end
        plot(newlgth,newnewoutfile1(j,2:end), 'o');
        xlim([lower-50 upper+50]);
        coefEstsxgrid=linspace(min(newlgth),max(newlgth),100);
        xgrid=linspace(min(newlgth),max(newlgth),100);
        line(xgrid,gainfunction(coefEsts,xgrid)+bg);
        title(sprintf('r^2= %0.3f G= %i',rsqs(j),int32(10000*G(j))));
        xlabel('Stripe Length (um)');
        ylabel('Intensity (arb)');
    end
end

%%%%%
%these four lines take out the rows that did not fit well (rsq<rsqCut)
newnewwavelength=newwavelength(find(rsqs>=rsqCut));
newnewnewoutfile1=newoutfile1(find(rsqs>=rsqCut),:);
trimmedG=G(find(rsqs>=rsqCut));
newrsqs=rsqs(find(rsqs>=rsqCut));

if ngain==1
    newnewnewwavelength=newnewwavelength(find(trimmedG>=0));
    newnewnewoutfile1=newnewnewoutfile1(find(trimmedG>=0),:);
    newtrimmedG=trimmedG(find(trimmedG>=0));
    newnewrsqs=newrsqs(find(trimmedG>=0));
else

```

```

newnewnewwavelength=newnewwavelength;
newnewnewoutfile1=newnewwavelength;
newtrimmedG=trimmedG;
newnewsqs=newrsqs;
end

a=0;
b=0;
for k=1:length(newnewnewwavelength)
    if 10000*newtrimmedG(k)<=500 && 10000*newtrimmedG(k)>=-500
        a=a+1;
        newwave(a)=newnewnewwavelength(k);
        newG(a)=10000*newtrimmedG(k);
        outfile(a,1)=newwave(a);
        outfile(a,2)=newG(a);
    else
        b=b+1;
    end
end

figure(1);
fig = figure(1);
set (fig, 'Units', 'normalized', 'Position', [0.1,0.1,.8,.8]); %maximize
subplot(1,1,1);
plot(newwave,newG,'o');
title(['Gain curve']);
xlabel('Wavelength (nm)');
ylabel('Gain (cm^-1)');

figure(2);
subplot(1,1,1);
hist(newnewsqs);
title(['Distribution of r^2 values.']);
disp('');

%creating new excel sheet
write=input(sprintf('Write output data to file?\n1: Write output file\n2:
Close program\n(default=2, close without saving)\n'));
if isempty(write)
    write=2;
end

%output file location
if write==1
    [outName outPath]=uiputfile({'* .csv'}, 'Save Output File', 'GainCurve');
    csvwrite([outPath '\\" outName],outfile);
end

```